ARO 24788.7-EG

②

PREDICTION OF UNSTEADY TRANSONIC SEPARATED FLOW FOR MISSILE APPLICATIONS

Final Report

P. Reisenthel and D. Nixon

November 20, 1990

U.S. Army Research Office
Contract No. DAAL03-87-C-0008

Nielsen Engineering & Research, Inc.
510 Clyde Avenue
Mountain View, California

NEAR TR 418

APPROVED FOR PUBLIC RELEASE
DISTRIBUTION UNLIMITED

UNCLASSIFIED
SECURITY CLASSIFICATION OF THIS PAGE

REPORT DOCUMENTATION PAGE

1a. REPORT SECURITY CLASSIFICATION
Unclassified

1b. RESTRICTIVE MARKINGS

2a. SECURITY CLASSIFICATION AUTHORITY

2b. DECLASSIFICATION / DOWNGRADING SCHEDULE

3. DISTRIBUTION / AVAILABILITY OF REPORT
Approved for public release;
distribution unlimited.

4. PERFORMING ORGANIZATION REPORT NUMBER(S)

5. MONITORING ORGANIZATION REPORT NUMBER(S)
ARO 24788.7-EG

6a. NAME OF PERFORMING ORGANIZATION
Nielsen Engineering &
Research, Inc.

6b. OFFICE SYMBOL *(If applicable)*

7a. NAME OF MONITORING ORGANIZATION
U. S. Army Research Office

6c. ADDRESS *(City, State, and ZIP Code)*
510 Clyde Avenue
Mountain View, CA 94043-2287

7b. ADDRESS *(City, State, and ZIP Code)*
P. O. Box 12211
Research Triangle Park, NC 27709-2211

8a. NAME OF FUNDING / SPONSORING ORGANIZATION
U. S. Army Research Office

8b. OFFICE SYMBOL *(If applicable)*

9. PROCUREMENT INSTRUMENT IDENTIFICATION NUMBER
DAAL03-87-C-0008

8c. ADDRESS *(City, State, and ZIP Code)*
P. O. Box 12211
Research Triangle Park, NC 27709-2211

10. SOURCE OF FUNDING NUMBERS

PROGRAM ELEMENT NO.	PROJECT NO.	TASK NO.	WORK UNIT ACCESSION NC

11. TITLE *(Include Security Classification)*
Prediction of Unsteady Transonic Separated Flow for Missile Applications.

12. PERSONAL AUTHOR(S)
P. Reisenthel, D. Nixon

13a. TYPE OF REPORT
Final

13b. TIME COVERED
FROM 7/1/87 TO 10/15/90

14. DATE OF REPORT *(Year, Month, Day)*
90 November 20

15. PAGE COUNT
6

16. SUPPLEMENTARY NOTATION The view, opinions and/or findings contained in this report are thos of the author(s) and should not be construed as an official Department of the Army positio policy, or decision, unless so designated by other documentation.

17. COSATI CODES

FIELD	GROUP	SUB-GROUP
20	04	
16	02	01

18. SUBJECT TERMS *(Continue on reverse if necessary and identify by block number)*
unsteady flow, transonic flow, flow separation, missile configurations, indicial theory, numerical modeling, aeroelasticity

19. ABSTRACT *(Continue on reverse if necessary and identify by block number)*

A theory was developed to treat flow separation and related vortex effects in unsteady transonic flow around slender bodies. This theory involves the simultaneous solution of a modified Transonic Small Disturbance Equation, a kinematic vector potential equation, and a three-dimensional transport equation for the streamwise vorticity. In this theory, flow separation is modeled using normal vorticity jets placed along the separation line. The location and strength of the separating vorticity was determined from empirical criteria. A steady version of the theory was implemented using a considerably developed form of the TWING potential code, while the unsteady implementation was performed using an enhanced version of the computational aeroelasticity program (CAP-TSD). A critical result was that a second order correction to the pressure, namely, the inclusion of the rotational streamwise velocity component, is necessary ~~in order~~ to account for the tilting of vortices away from the body axis. Time-accurate computations of subsonic, transonic, and supersonic flow show that it is possible to compute the flow around realistic angle of attack missile configurations, thus showing considerable potential for aeroelastic computations and unsteady aerodynamics. ~~The~~ results of two-dimensional Navier-Stokes calculations indicate that several key aspects characterizing the time-dependent behavior of boundary layer separation may be accurately predicted using indicial theory. These results demonstrate the possibility of significant phase lags and fluctuation overshoots of the normal vorticity flux at separation.

20. DISTRIBUTION / AVAILABILITY OF ABSTRACT
☒ UNCLASSIFIED/UNLIMITED ☐ SAME AS RPT. ☐ DTIC USERS

21. ABSTRACT SECURITY CLASSIFICATION
Unclassified

22a. NAME OF RESPONSIBLE INDIVIDUAL
Dr. Thomas L. Doligalski

22b. TELEPHONE *(Include Area Code)*
(919)549-0641

22c. OFFICE SYMBOL

DD FORM 1473, 84 MAR

83 APR edition may be used until exhausted.
All other editions are obsolete.

SECURITY CLASSIFICATION OF THIS PAGE
UNCLASSIFIED

TABLE OF CONTENTS

STATEMENT OF PROBLEM STUDIED

The problem studied was motivated by the technological need to efficiently predict unsteady transonic flow with vortex effects. Although much progress has been made in the last decade[1] in the numerical simulation of transonic flow typical of that occurring over wings of commercial aircraft, these flows usually have negligible vortical effects. In contrast, missiles flying at transonic speeds experience important effects due to separation and, thus, vortical effects. Consequently, the purpose of the present research was to derive a reduced set of governing equations which properly account for vortical effects in unsteady transonic flow, and to explore various implementations of this theory using well-tested potential flow solvers as a basis. The result will be efficient and cost effective computations for maneuvering missiles and aeroelastic effects.

SUMMARY OF MOST IMPORTANT RESULTS

A theory was developed to treat flow separation and related vortex effects in unsteady transonic flow around slender bodies.[2,3] This theory involves the simultaneous solution of a potential equation (or modified Transonic Small Disturbance Equation), a kinematic vector potential equation, and a three-dimensional unsteady vorticity transport equation for the streamwise (dominant) component of vorticity. The theory constitutes a subset of the Euler equations, where flow separation is modeled by introducing vorticity in the flow field by means of normal vorticity jets placed along the separation line. In this model, the location and strength of the separating vorticity are determined from empirical criteria.[4] It was shown that the theory can be regarded as a unifying theory for all speed ranges since it provides a framework for incorporating vorticity into the classic potential equation for incompressible as well as compressible flow. As a further refinement, it was also shown that a second order correction to the pressure, namely the inclusion of the rotational streamwise velocity component, was critical in order to properly account for the tilting of lee-side vortices away from the body axis.

An extension of the analysis[5] that included two components of vorticity showed that in the presence of constant shed vorticity the vortex must expand in size as it progresses down the body. This extended analysis also explained the creation of entropy when vorticity is introduced at a non-normal angle to the body, thus resulting in a loss of total pressure within the rolled-up vortex. An important result is that, for slender bodies, the three components of vorticity are separable in magnitude.

The numerical implementation of the steady version of the theory was performed using a considerably developed form of the TWING potential code.[6] Results for bodies at high angles of attack and at subsonic and transonic Mach numbers were obtained and compared to experiment and, for subsonic flow, to a discrete vortex method. These demonstrated the need for the aforementioned second order correction on the pressure. It was also found that numerical errors can dissipate an isolated vortex by a considerable amount, suggesting the need for further refinement of the vorticity transport algorithm.

Similar problems were observed with the approximate factorization algorithm used in the unsteady implementation of the theory.[3] The unsteady code was based on the well-tested unsteady transonic potential flow solver CAP-TSD. This code is capable of predicting the unsteady transonic and supersonic flow over a complete aircraft configuration including fins, stores, and pylons.[7] Improvements in the representation of the fuselage on the one hand, and the development of an appropriate transfer of boundary conditions between the true and computational surfaces on the other, were found to be key considerations in being able to resolve vorticity transport close to the body.[8] Time-accurate calculations using this substantially enhanced version of the CAP-TSD code were performed for complete missile configurations in the subsonic, transonic, and supersonic flow regimes. The results demonstrated that the flow around realistic angle of attack configurations could be calculated for unsteady transonic flow with separation, thus showing considerable potential for aeroelastic computations and unsteady aerodynamics.

Due to the unavailability of experimental data for unsteady separated transonic flow over three-dimensional slender bodies, comparisons of time-accurate solutions with experiment could only be performed for steady angle of attack. In the unsteady cases, a quasi-steady implementation of the modified Stratford[9] criterion was used to predict the instantaneous separation line. The question as to whether additional time lags may originate from the separation process itself was addressed by means of two-dimensional unsteady Navier-Stokes calculations of flow around a circular cylinder. The results of this effort indicated that the time dependent behavior of integral quantities (such as vorticity flux and drag coefficient) and to a lesser extent of the separation angle could be predicted with great accuracy using indicial theory.[10] The location of the separation point was found to be satisfactorily predicted within the range of frequencies corresponding to missile flutter. In particular, it was shown that substantial phase delays and overshoots of fluctuations in the vorticity flux could be attained within the range of frequencies of interest. Although these results were obtained for low Reynolds number laminar flow, they establish for the first time that several key aspects characterizing the time-dependent behavior of two-dimensional boundary layer separation may be predicted using indicial theory. Whether such ideas are applicable to high Reynolds number turbulent flow for the development of fully unsteady separation criteria remains to be established.

The unsteady computer code that was developed under the present contract is currently being used for sea-skimming missile applications (NSWC Contract No. N60921-90-C-0134), in which missiles flying close to the sea surface experience periodic gusts due to the waves. These gusts can excite structural (aeroelastic) modes which result in a deterioration of the control systems' performance.[11] The unsteady aeroelastic effects make the code ideally suited for this application. The code is currently being enhanced to calculate the transonic and supersonic flow over a swept-finned missile of arbitrary roll angle configuration. This additional enhancement will be supplemented with a more complete version of the Transonic Small Disturbance Equation which includes the necessary nonlinearities for swept horizontal as well as vertical shocks.

LIST OF PUBLICATIONS

1. Nixon, D.: The Occurrence of Multiple Solutions for the "TSD-Euler" Equation, NEAR Paper No. 239, Nielsen Engineering & Research, Inc., March 1988 (to be published in Acta Mechanica).

2. Nixon, D., Caruso, S. C., and Klopfer, G. H.: Prediction of Transonic Flow with Vortex Effects, AIAA Paper 90-0389.

3. Nixon, D.: The Effect of Vortex Rotation on the Flow Around a Missile, NEAR Paper No. 266, Nielsen Engineering & Research, January 1990, (Submitted to AIAA Journal).

4. Nixon, D., Reisenthel, P., Torres, T. O., and Klopfer, G. H.: Prediction of Unsteady Transonic Flow Around Missile Configurations, AIAA Paper 90-0934.

5. Reisenthel P. and Nixon, D.: Application of Indicial Theory to the Prediction of Unsteady Separation, NEAR Paper No. 288, Nielsen Engineering & Research, September 1990 (Submitted for presentation at the AIAA 22nd Fluid and Plasmadynamics Conference, Honolulu, HI, June 24-26, 1991).

6. Reisenthel, P. and Nixon, D.: Prediction of Unsteady Separated Transonic Flow Around Missile Configurations, AIAA Paper 91-0601, to be presented at the AIAA 29th Aerospace Sciences Meeting, Reno, NV, January 7-10, 1991.

LIST OF PARTICIPATING PERSONNEL

Dr. D. Nixon, President and Principal Investigator
Dr. G. H. Klopfer, Research Scientist
Dr. S. C. Caruso, Research Scientist
Ms. T. O. Torres, Research Engineer
Dr. P. Reisenthel, Research Scientist

LIST OF PRESENTATIONS

Formal Presentations:

- Naval Postgraduate School, Monterey CA, October 1989
- AIAA 28th Aerospace Sciences Meeting, Reno, NV, January 1990
- AIAA 31st Structures, Structural Dynamics, and Materials Conference, Long Beach, CA, April 1990
- Wright Research & Development Center, Wright-Patterson AFB, OH, September 1990

- NASA Langley Research Center, Langley, VA, September 1990

Informal Talks:

- Gil Graff, NSWC - White Oak, Silver Spring, MD, October 1989
- Andrew Wardlaw, NSWC - White Oak, Silver Spring, MD, October 1989
- Walter Sturek, BRL, Aberdeen, MD, May 1990
- Billy Walker, MICOM, Huntsville, AL, June 1990
- Dean Christiansen, MICOM, Huntsville, AL, October 1990.

BIBLIOGRAPHY

1. Edwards, J. T. and Thomas, J. L.: Computational Methods for Unsteady Transonic Flows, Unsteady Transonic Aerodynamics, Vol. 120 of Progress in Astronautics and Aeronautics, ed. by D. Nixon, AIAA 1989.

2. Klopfer, G. H. and Nixon, D.: Transonic Flows with Vorticity Transport Around Slender Bodies, AIAA Journal, Vol. 27, No. 10, 1989, pp. 1461-1464.

3. Nixon, D., Reisenthel, P. H., Torres, T. O., and Klopfer, G. H.: Prediction of Unsteady Transonic Flow Around Missile Configurations, AIAA Paper 90-0934.

4. Mendenhall, M. R. and Perkins, S. C., Jr.: Vortex Cloud Model for Body Vortex Shedding and Tracking, Tactical Missile Aerodynamics, Vol. 104, Progress in Astronautics and Aeronautics, ed. by M. J. Hemsch and J. N. Nielsen, AIAA 1986.

5. Nixon, D.: The Effect of Vortex Rotation on the Flow Around a Missile. NEAR Paper No. 266, Nielsen Engineering & Research, January 1990, (Submitted to AIAA Journal).

6. Nixon, D., Caruso, S. C., and Klopfer, G. H.: Prediction of Transonic Flow with Vortex Effects, AIAA Paper 90-0389.

7. Batina, J. T.: An Efficient Algorithm for Solution of the Unsteady Transonic Small Disturbance Equation, AIAA Paper 87-0109.

8. Reisenthel, P. and Nixon, D.: Prediction of Unsteady Separated Transonic Flow Around Missile Configurations. AIAA Paper 91-0601, to be presented at the AIAA 29th Aerospace Sciences Meeting, Reno, NV, January 7-10, 1991.

9. Stratford, B. S.: The Prediction of Separation of the Turbulent Boundary Layer, Journal of Fluid Mechanics, Vol. 5, 1959, pp. 1-16.

10. Reisenthel, P. and Nixon, D.: Application of Indicial Theory to the Prediction of Unsteady Separation, NEAR Paper No. 288, Nielsen Engineering & Research, September 1990 (Submitted for presentation at the AIAA 22nd Fluid and Plasmadynamics Conference, Honolulu, HI, June 24-26, 1991).

11. Lesieutre, D. J., Nixon, D., Dillenius, M. F. E., and Torres, T. O.: Analysis of Missiles Flying Low Over Various Sea States, NEAR TR 408, November 1989, also AIAA Paper 90-2855, August 1990.

APPENDIX

COPIES OF PUBLICATIONS AND CONFERENCE PAPERS RESULTING FROM THIS CONTRACT

The Occurrence of Multiple Solutions for the "TSD-Euler" Equation

by

David Nixon

Nielsen Engineering & Research, Inc.
Mountain View, California
94043-2287 USA

Summary

In a recent paper the TSD- Euler equation for transonic flow has been derived. This equation is similar in some respects to the TSD equation but has both entropy and vorticity terms retained. In this paper the existence of multiple solutions for the TSD-Euler equation is examined and it is found that such solutions excist for a small range of Mach numbers and airfoil thickness. It is found also that the addition of a vorticity flux on the airfoil surface can enhance the appearance of multiple solutions.

Introduction

The existence of multiple or "phantom" solutions in potential simulations of transonic flow was first described by Steinhoff & Jameson [1]. These solutions give lift for a symmetric airfoil at zero degrees angle of attack and appeared for a small range of Mach number. These phantom solutions appear when some degree of asymmetry, either in the algorithm or in the initial conditions, is introduced into the solution process for a certain range of Mach numbers. The asymmetry may also be introduced by a physical angle of attack. It appears that there is a certain range of Mach number in which the phantom solution is preferred to the conventional solution. Most of the early work on the occurrence of phantom solutions concerned steady flow, although Williams et al [2] solved the unsteady TSD equation to give phantom solutions for unsteady flows. Williams et al [2] also modeled viscous effects by a boundary layer displacement thickness and found phantom solutions for a slightly different Mach number range than for inviscid flow models. Nixon [3] attempted to explain mathematically the occurrence of phantom solutions and concluded that the flow must be transonic. Phantom solutions have also been found for three-dimensional flows [4]. These phantom solutions have, until recently, not been observed in equation sets other than the potential equation; although, it has been speculated by Williams et al [2] and Nixon [5] that they would exist for the Euler equations. All of these studies are concerned with potential flow, although Salas et al [6] did try to find phantom solutions for the Euler equations with no success. This paper is concerned with the possible occurrence of phantom solutions in the Euler equations although the analysis uses a subset of the Euler equations, called the TSD-Euler equation derived by Nixon [5]. It is concluded that for very thin airfoils at a freestream Mach number close to unity phantom solutions to the TSD-Euler equation exist. It is found also that the addition of vorticity at the airfoil boundary enhances the probability of obtaining a phantom solution.

Examples of Multiple Solutions

An example of the pressure distribution around a symmetric Joukowski airfoil at zero degrees angle of attack and $M_\infty = 0.85$ is shown in Figure 1. This solution was produced by solving the transonic small disturbance (TSD) equation using the conservative Murman-Cole algorithm. The asymmetry was introduced as an initial condition. The phenomena appears for conventional lifting airfoils. An example [6] of the variation of lift coefficient, C_L, with angle of attack α, for a RAE2822 airfoil is shown in Figure 2. It may be observed that at $\alpha = 0.6$ degrees, C_L can have a value of about 0.5 or about 1.4. It is interesting to note that if the phantom solution is realizable the value of C_L would be three times the "conventional" value.

TSD-Euler Equation

One possible reason for the inability to find phantom solutions for the Euler equations is that the algorithms for solving the Euler equations do not satisfy these equations on the airfoil surface since the tangential velocity on the surface are found by extrapolation from the interior. It is noted by Nixon [3] that it is the behavior of the potential equation on the surface that gives rise to the eigensolution necessary to obtain phantom solutions. To examine this aspect further, Nixon [5] derived a "small disturbance" version of the Euler equations, the "TSD-Euler" equation, which includes the first order effects of entropy and vorticity. This equation reduces to the classic transonic small disturbance (TSD) equation (for which phantom solutions can be computed) in the absence of vorticity and has the advantage that the basic equation is satisfied everywhere, thus allowing the emergence of the necessary eigensolution.

The TSD-Euler equation [5] is given by

$$\left[\beta^2 u - k \frac{u^2}{2} \right]_x + v_y = \left(\frac{S}{R} \right)_x \tag{1}$$

where u and v are perturbation velocities in the x and y directions, respectively, nondimensionalized with respect to freestream values. S is the entropy change, R is the gas constant and

$$\beta^2 = 1 - M_\infty^2; \quad k = (\gamma + 1)\, M_\infty^2 \tag{2}$$

where M_∞ is the freestream Mach number. If ϕ is a perturbation velocity potential, and ψ is a vector potential, then

$$\left.\begin{aligned} u &= \phi_x + \psi_y \\ v &= \phi_y - \psi_x \end{aligned}\right\} \tag{3}$$

and

$$\psi_{xx} + \psi_{yy} = -\omega \tag{4}$$

where the vorticity ω is related to the entropy S by Crocco's theorem. The entropy generated at a shock is given by

$$\frac{S}{R} \simeq \frac{2\gamma}{(\gamma + 1)^2} \left(M^{+2} - 1 \right)^3 \tag{5}$$

where M^+ is the Mach number just ahead of the shock and is related to u. The entropy generated by the shock is constant with respect to x aft of the shock. The tangency boundary condition is represented by the thin airfoil approximation so that the equation and its boundary conditions reduce to the classic TSD formulation in the absence of vorticity. The tangency boundary condition is given by

$$(\phi_y - \psi_x)_{y = \pm 0} = y_s'(x) \tag{6}$$

where $y = y_s(x)$ denotes the airfoil.

Equation (1) with its boundary condition, Equation (6), and the vorticity equation, can be written in similarity form to give

$$\left[\bar{u} - \frac{\bar{u}^2}{2}\right]_x + \bar{v}_{\bar{y}} = \frac{-2\gamma}{(\gamma + 1)^2} k \beta^2 \frac{\partial}{\partial x} [(1 - \bar{u}^+)^3] \tag{7}$$

$$\bar{v}(x, \pm o) = K \bar{y}_s'(x) \tag{8}$$

$$\bar{u} = \bar{\phi}_x + \beta^2 \bar{\psi}_{\bar{y}} \; ; \quad \bar{v} = \bar{\phi}_{\bar{y}} - \bar{\psi}_x \tag{9}$$

$$\beta^2 \bar{\psi}_{\bar{y}\bar{y}} + \bar{\psi}_{xx} = - \bar{\omega} = \frac{2\gamma}{(\gamma+1)} \beta^3 \frac{\partial}{\partial \bar{y}} [(1-\bar{u}^+)^3] \tag{10}$$

where $\bar{\phi} = {}^k/_{\beta^2} \phi$; $\bar{\psi} = {}^k/_{\beta^3} \psi$; $\bar{\omega} = {}^k/_{\beta^3} \omega$, $\bar{y} = \beta y$ and $\bar{u}^+$ is the value of $\bar{u}$ just ahead of the shock. In the derivation of Equation (10) the first order approximation to Crocco's Equation has been used; thus

$$\omega = \frac{1}{R\gamma M_\infty^2} \frac{\partial}{\partial y} (S/R) \tag{11}$$

If $\tau\bar{y}_s = y_s$ where τ is the thickness of the airfoil then a transonic similarity parameter, K, can be defined as

$$K = {}^{k\tau}/_{\beta^3} \tag{12}$$

The transonic similarity parameter, K, is constant for combinations of Mach number and thickness; if the airfoil is very thin the Mach number approaches unity and the entropy production vanishes as $\tau \to o$ and $\beta 2 \to o$. Thus for a given K it is possible to approach the TSD equation arbitrarily closely by varying the thickness and the Mach number.

The set of equations, Equations (7-10), can be solved using the same algorithm and treatment of the boundary conditions used in the TSD example, thus ensuring that a phantom solution can be obtained as $\beta \to 0$.

Addition of Vorticity

If any vorticity is introduced into the two dimensional flow the vorticity vector will be aligned with the spanwise direction and the magnitude of the vorticity will not change in this direction. According to the equations of Klopfer and Nixon (7) this vorticity is convected like

$$(\omega u)_x + (\omega v)_y = 0 \qquad (13)$$

to a first approximation. The velocity induced by the vorticity is given by Equation (4) or Equation (10). In these models vorticity is defined as

$$v_x - u_y = \omega \qquad (14)$$

Using Equation (14) and Equation (13) gives an alternative representation of the vorticity transport, namely,

$$A_{xx} + A_{yy} = \omega^2 + \omega_x^{\nu} - \omega_y u \qquad (15)$$

where

$$A_x = \omega\, v;\ A_y = -\, \omega\, u \qquad (16)$$

A suitable boundary condition for Equation (15) is that normal derivatives of A are specified on the boundaries, that is Neumann boundary conditions are used.

Equation (15) can be solved using a simple central differencing scheme with the vorticity terms on the right hand side set retarded by one iteration. Equation (15) can be solved iteratively with Equations (1), (3), (4), and (5).

In one of the examples discussed in the next section a small amount of vorticity, comparable in magnitude to the shock generated vorticity, is introduced over a small part of the chord (usually over three grid points). The amount of vorticity, ω, is symmetric on both surfaces of the airfoil; the symmetry or asymmetry of u depends on whether a phantom solution is present.

Results from the TSD-Euler Equation

It has been found that phantom solutions for the TSD-Euler equation, Equation (1), for the NACA00XX series airfoil, can only be obtained for a very thin airfoil at a freestream Mach number close to unity. This is in keeping with a suggestion of Williams et al [2]. An example for a 0.00076% thick airfoil at $M_\infty = 0.9945$ is shown in Figure 3. The lowest Mach number for which a phantom solution could be obtained is 0.986 for an airfoil of thickness 0.003%. These results indicate that the occurrence of the phantom solutions in the Euler equations is not likely to be of practical interest.

As an experiment a vorticity source, equivalent to a heat sink, was placed upstream of the shock waves on the airfoil surface. The entropy induced by this source is approximately the same magnitude of that produced by the shock but with the opposite sign; (S/R) is of the order of 10^{-4}. Using this device it proved possible to generate a lifting solution for a Mach number of 0.945 for a 2 1/2% thick airfoil; the solution is shown in Figure 4. This is a much more interesting proposition than the previous cases. It can be inferred from this result that a small amount of vorticity can greatly increase the chance of getting the phantom solution.

If the phantom solutions found for the TSD-Euler equations could be made physically realizable they are only practical if a vorticity source is inserted into the airfoil boundary, indicating that a control device is necessary to obtain these solutions. The fact that phantom solutions have been found for flows with shock-induced and distributed vorticity suggests that the solutions can be obtained for the Navier-Stokes equations. The calculations reported by Williams et al [2] for boundary layer flows reinforce this point. It is suggested that the phantom solution are realizable and that these could provide radically increased aerodynamic efficiency of conventional flows as may be observed from the result shown in Figure 2.

Concluding Remarks

An equation with many similarities to the Euler equations has been examined for the occurrency of multiple or phantom solutions. It is concluded that although these solutions do exist it is for a much more restrictive range of Mach numbers than the potential equation. If a small amount of vorticity is introduced into the flow through the airfoil surface, upstream of the shock, then phantom solutions can be found for a much larger range of Mach number. Since this model has vorticity, entropy and shock waves represented it is speculated that phantom solutions could be found for the Navier-Stokes equations. The fact that such solutions of the potential equation coupled with a boundary layer model serves to reinforce this point.

If the Navier-Stokes equations have phantom solutions similar to those found for the potential or TSD-Euler equations then it may be possible to exploit this "new" aerodynamic phenomena to radically improve aerodynamic efficiency. In fact there may be many instances of phantom solutions involving more than one location of concentrated vortices, shock waves, or shear surfaces that could be used to revolutionize aircraft flight if these phenomena can be made to occur and stabilized in a real flight.

Acknowledgement

Part of this work was supported by the U.S. Army under Contract No. DAAL03-87-C-0008.

REFERENCES

[1] Steinhoff, J. S. and Jameson, A.: Multiple Solutions of the Transonic Potential Flow Equation. <u>AIAA J.</u>, Vol. 20, (11), pp. 1521-1525 (1982).

[2] Williams, M. H., Bland, S. R., and Edwards, J. W.: Flow Instability in Transonic Small Disturbance Theory. AIAA J., Vol. 23, (10), pp. 1491-1496 (1985).

[3] Nixon, D.: Observations on the Occurrence of Multiple Solutions in Transonic Potential Theory. Acta Mechanica 68, pp. 43-56 (1987).

[4] Hicks, R. M.: Private Communication (1983).

[5] Nixon, D.: The Effect of Entropy Production on the Occurrence of Multiple Solutions in Transonic Flow (to be published in Acta Mechanica).

[6] Salas, M. D., Jameson, A., and Melnik, R. E.: A Comparative Study of the Non-Uniqueness Problem of the Potential Equation. Proc. AIAA Comp. Fluid Dynamics Conf., pp. 48-60 (1983).

[7] Klopfer, G. H. and Nixon, D.: Transonic Flow with Vorticity Transport around Slender Bodies. Nielsen Engineering & Research Paper No. 222, June 1987. (Also submitted to AIAA Journal)

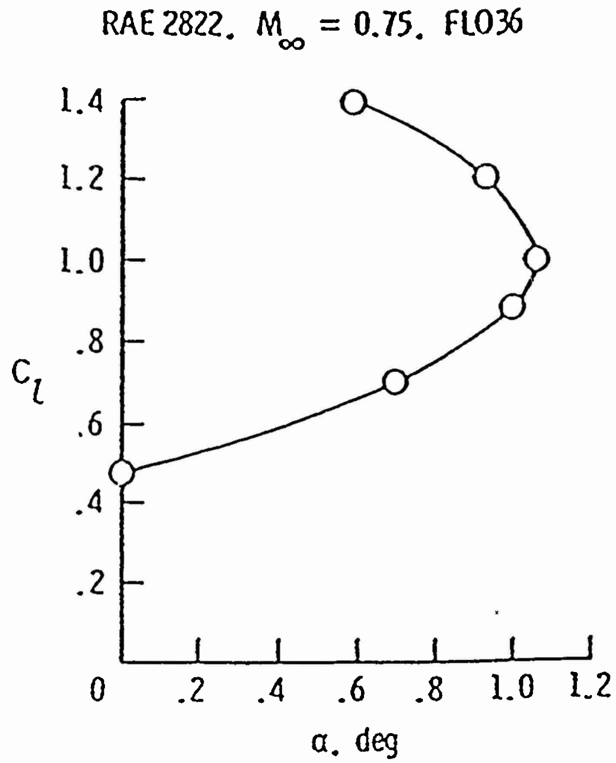

Figure 1.- Lift-α curve obtained with FLO 36 for an RAE 2822 airfoil.

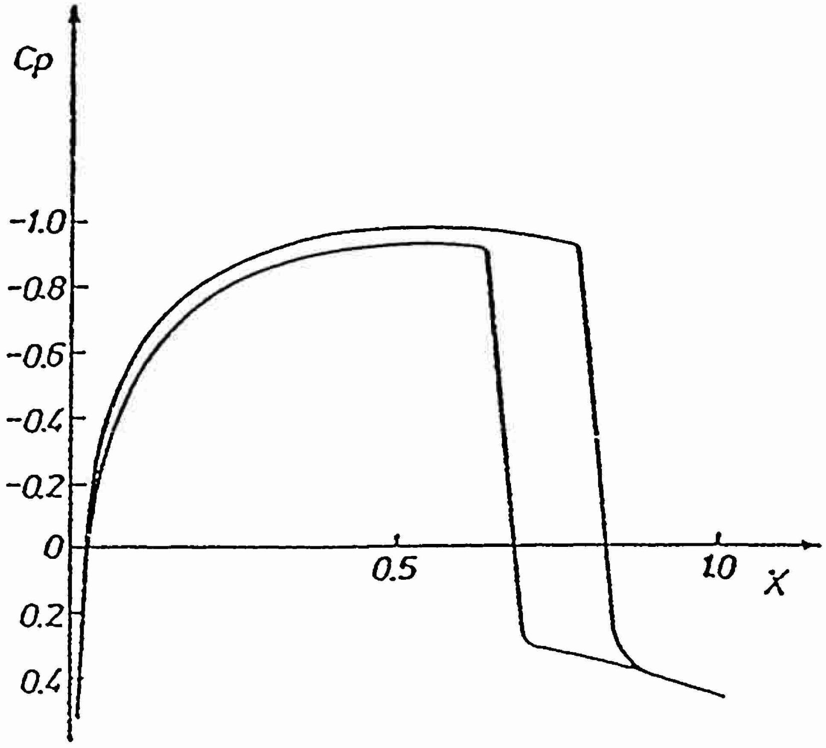

Figure 2.- Pressure distribution around a 11.8% Joukowski airfoil; $M_\infty = 0.85$, $\alpha = 0.0°$.

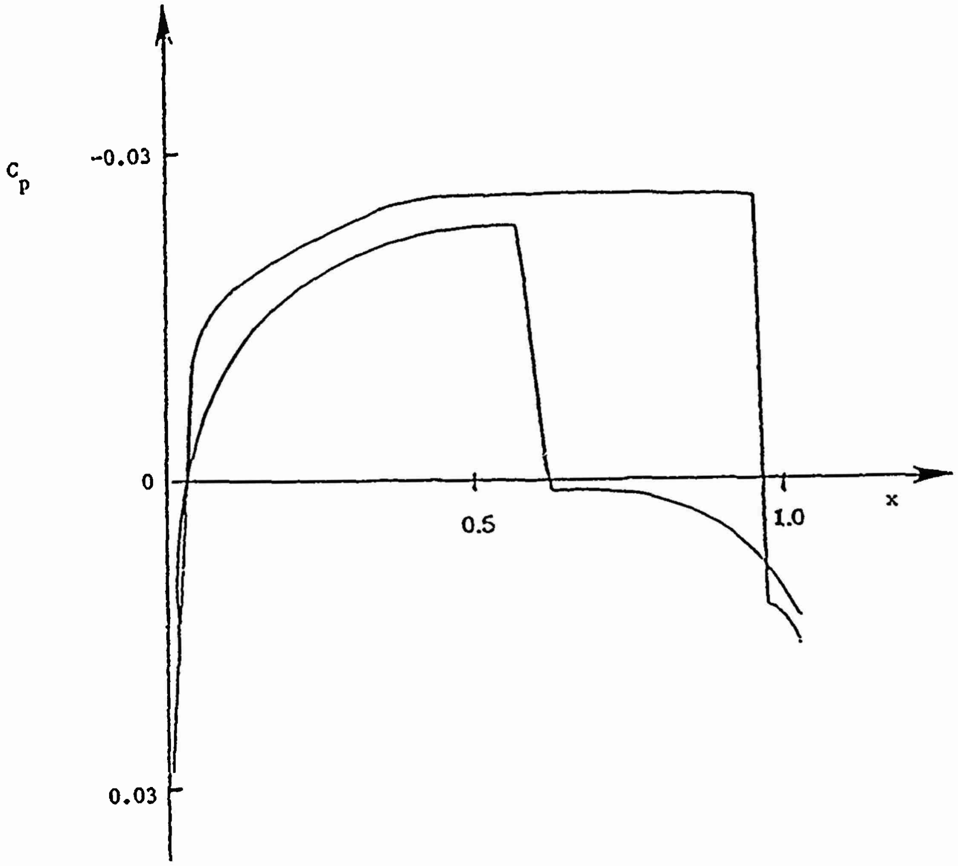

Figure 3.- Pressure distribution around a NACA00XX airfoil, $M_\infty = 0.9945$, $\tau = 0.00076\%$ (TSD-Euler).

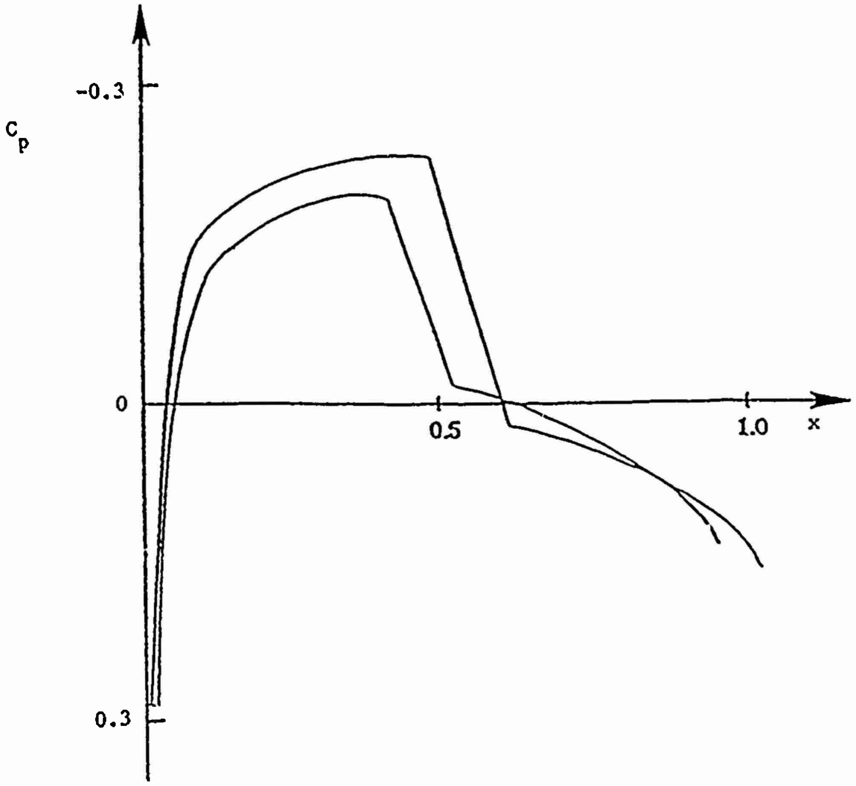

Figure 4.- Pressure distribution around a NACA00XX airfoil, $M_\infty = 0.945$, $\tau = 0.025\%$ (TSD-Euler and vorticity source).

AIAA-90-0389

Prediction of Transonic Flow with Vortex Effects

D. Nixon, S. C. Caruso, and G. H. Klopfer
Nielsen Engineering & Research, Inc.
Mountain View, CA

28th Aerospace Sciences Meeting

January 8-11, 1990/Reno, Nevada

For permission to copy or republish, contact the American Institute of Aeronautics and Astronautics
370 L'Enfant Promenade, S.W., Washington, D.C. 20024

PREDICTION OF TRANSONIC FLOW WITH VORTEX EFFECTS

D. Nixon,* S. C. Caruso,** and G. H. Klopfer***
Nielsen Engineering & Research, Inc.
510 Clyde Avenue
Mountain View, CA 94043-2287

Introduction

In recent years it has been possible to predict the unsteady transonic flow around a wing, especially those typical of commercial aircraft, in a fairly efficient manner. Frequently, the computer codes that are used are based on potential theory and are considerably faster than a corresponding calculation using the Euler equations. However, these methods have been developed for aircraft and are not really applicable to missile flows where vorticity effects are important; the potential approximation cannot predict the effects of vorticity other than by representing a vortex wake by an infinitely thin sheet which is excluded from the computational domain. This model is complicated and may not be a viable option for routine calculations around real aircraft or missile configurations because the geometry of the vortex sheet can get quite complex.

Missiles generally have low aspect ratio fins and slender bodies, neither of which are features of commercial aircraft; this may cause problems in grid generation. The airflow over missiles is dominated by vortex effects; this is in contrast to the attached flow over a commercial aircraft. For steady missile flow a variety of prediction methods are available, ranging from panel methods, with the addition of nonlinear vortex dynamics, to the Euler equations or Navier-Stokes equations. The Navier-Stokes equations will model flow separation and track the resulting vorticity but are only as accurate as the turbulence model used in the calculation. This is critical in defining the separation line. The prediction methods based on the Euler equations need some empirical criteria to predict the location and strength of the separating vortex sheet; the Euler equations will then model the transport of this vorticity reasonably accurately. A detailed discussion of the methods used to predict steady flows over missiles is given in Reference (1). In order to predict unsteady flow over a missile to adequate accuracy, the method must be able therefore, to treat unsteady separated flow. Furthermore, if it is necessary to predict the steady flow at transonic, rather than supersonic, speeds the method must be computationally efficient since, unlike supersonic flow which can use a marching procedure, transonic flow methods require numerous sweeps of the computational domain leading to large computational times.

It would be ideal to use the Navier-Stokes equations to model unsteady transonic flow around missiles, but there are several difficulties with this approach. The most obvious difficulty is the computer time required, which is several orders of magnitude greater than that required for a potential calculation. Even if a dedicated supercomputer were available for such calculations, the computation of the necessary flow separation might be inaccurate because of the inherent inaccuracy of many present turbulence models. The next best approach is to use the time dependent Euler equations which require some empirical factor to initiate separation and compute the shed vorticity. This empiricism would be a development of the steady flow criteria described in Reference (1). If the separation line and shed vorticity can be predicted, then the Euler equations would be a viable model. However, since missiles are slender some further approximations can be made. This paper is concerned with developing a method of predicting the pressure distribution on missiles at transonic and supersonic speeds. The concepts developed in this work will be transferred to an unsteady analysis. The approach is to make as much use of the existing technology as possible. The final goal is to develop a computer code capable of predicting the unsteady transonic flow about missiles for use in aeroelastic calculations or during maneuver. The present paper is an account of the first phase of the work, namely the development of a steady flow variant of the method.

The approach is based on experience gained in steady subsonic and supersonic flow predictions for missiles, in particular, the fact that if a separation line and the strength of the vorticity introduced at that line can be estimated empirically, the governing equations (such as the Euler equations) will represent the transport of this vorticity accurately. Because the computational time for the Euler equations for an unsteady calculation is considerably greater than that for a potential calculation, a simplified model is used.

The basic equations are those derived by Klopfer and Nixon[2] and are a subset of the Euler equations. For slender bodies, the five Euler equations are reduced to an equation similar to the three-dimensional unsteady potential equation, a vorticity transport equation and a two-dimensional Poisson equation. Apart from the reduced set of equations, a second advantage is that one of the equations is almost identical to the potential equation for which there are well tested computer codes. This allows the development of a prediction method

---

*President
**Research Scientist, Member AIAA
***Research Scientist

based considerably on proved technology. A derivation of the equations is given in Reference 2.

Basic Equations

From Reference 2, the basic equations are as follows:

Vorticity Transport

$$u_\infty \Omega_x + (v\Omega)_y + (w\Omega)_z = 0 \tag{1}$$

Rotational Crossflow

$$A_{yy} + A_{zz} = -\Omega \tag{2}$$

Mass Conservation

$$(\rho u)_x + (\rho u)_y + (\rho w)_z = 0 \tag{3}$$

where

$$u = \phi_x ; v = \phi_y + A_z ; w = \phi_z - A_y \tag{4}$$

and

$$\rho = \rho_\infty \left\{ 1 + \frac{(\gamma-1) M_\infty^2}{2} (1-u^2-v^2-w^2) \right\}^{\frac{1}{\gamma-1}} \tag{5}$$

ϕ is the velocity potential, A is the vector potential, ρ is the density, M_∞ is the freestream Mach number, Ω is the vorticity in the streamwise direction, and u, v, and w are velocities in the coordinate directions x, y, z respectively.

Governing Equations in Transformed Curvilinear Coordinates

In order to treat complex geometries, the governing equations are transformed to a curvilinear body conforming coordinate system which is orthogonal in the crossflow plane:

$$x = \xi$$

$$y = y(\xi, \eta, \zeta) \tag{6}$$

$$z = z(\xi, \eta, \zeta)$$

Note that in the transformed coordinates, ξ is the streamwise direction, the η and ζ directions are a basis for the crossflow plane, and $\vec{\nabla}\eta \cdot \vec{\nabla}\zeta = 0$. The η and ζ directions are parallel and normal, respectively, to the body surface.

Before presenting the transformed equations, an alternate formulation of the continuity equation will be derived. The total velocity, $\vec{V}$, is defined as the sum of potential and rotational velocity components, $\vec{V}^P$ and $\vec{V}^R$, respectively:

$$\vec{V} = \vec{V}^P + \vec{V}^R \tag{7}$$

where

$$\vec{V}^P = \vec{\nabla}\phi \tag{8}$$

and

$$\vec{V}^R = \vec{\nabla} x \vec{A} \tag{9}$$

with

$$\vec{A} = (A, O, O)^T \tag{10}$$

In Cartesian coordinates:

$$\vec{V}^P = (\phi_x, \phi_y, \phi_z)^T \tag{11a}$$

and

$$\vec{V}^R = (0, A_z, -A_y)^T \tag{11b}$$

Note that

$$\vec{\nabla} x \vec{V}^P = 0 \tag{12a}$$

and

$$\vec{\nabla} \cdot \vec{V}^R = 0 \tag{12b}$$

In other words, the potential velocity field is irrotational and the rotational velocity field is divergence free.

The continuity equation, (3), in vector form is

$$\vec{\nabla} \cdot (\rho \vec{V}) = 0 \tag{13}$$

Combining Equations (7) - (13) gives

$$\vec{\nabla} \cdot (\rho \vec{\nabla} \phi) = S \tag{14}$$

where

$$S = -\vec{V}^R \cdot \vec{\nabla}\rho \tag{15}$$

Equation (14) is the full potential equation with a source term. It can be transformed from Cartesian coordinates to strong conservation law (SCL) form. An existing code is used to solve Equation (14) in SCL form, and will be described below.

The vorticity transport equation transforms to the following SCL form:

$$\hat{\Omega}_\xi + (V\hat{\Omega})_\eta + (W\hat{\Omega})_\zeta = 0 \tag{16}$$

where

$$\hat{\Omega} = \frac{\Omega}{J} \tag{17}$$

and the contravariant velocities are defined

$$V = \eta_x + \eta_y\ v/u_\infty + \eta_z\ w/u_\infty \tag{18a}$$

$$W = \zeta_x + \zeta_y\ w/u_\infty + \zeta_z\ w/u_\infty \tag{18b}$$

Formulas for the Jacobian, J, and the metric terms η_x, η_y, ζ_x, etc. can be found in Reference 3 for a generalized curvilinear transformation. The transformation, Equation (6), permits simplification of some of these terms.

The vector potential equation, (2), transforms to:

$$\alpha A_{\eta\eta} + BA_{\zeta\zeta} + \gamma A_\eta + \delta A_\zeta = -\Omega \tag{19}$$

where

$$\alpha = \eta_y^2 + \eta_z^2$$

$$\beta = \zeta_y^2 + \zeta_z^2$$

$$\gamma = \eta_{yy} + \eta_{zz}$$

$$\delta = \zeta_{yy} + \zeta_{zz}$$

Since the transformation is orthogonal in the η-ζ plane, the cross-derivative term, $A_{\eta\zeta}$ does not appear.

To summarize, the governing equations, continuity, vorticity transport, and the vector potential equations have been transformed to a curvilinear coordinate system and are given by Equations (14), (16), and (19), respectively. The following section discusses boundary conditions used for these equations.

Boundary Conditions

Boundary conditions for the velocity potential, ϕ, the vorticity, Ω, and the vector potential, A, are required on the body surface and at the far field boundary. All boundary conditions will be described next.

Body Surface

Away from the separation locations, flow tangency is applied on the body surface:

$$\vec{V} \cdot \vec{n}\ \Big|_{\text{body}} = 0 \tag{20}$$

where $\vec{n}$ is the outward unit normal to the surface. This requires that

$$V_n^P + V_n^R = 0 \tag{21a}$$

where $V_n^{(\cdot)}$ is a normal velocity component. Equation (21a) indicates that either V_n^P or V_n^R can be arbitrarily specified. We choose

$$V_n^P = 0 \tag{21b}$$

since this condition is built into the existing full potential code. With V_n^P chosen, Equation (21a) requires that

$$V_n^R = 0 \tag{22}$$

In a locally orthonormal coordinate system in the crossflow plane with $\vec{n}$ and $\vec{t}$ (the unit tangential to the surface) as the basis vectors, the normal component of the rotational velocity becomes

$$V_n^R = -\frac{\partial A}{\partial t} \tag{23}$$

and the tangential component is:

$$V_t^R = \frac{\partial A}{\partial n} \tag{24}$$

Equations (22) and (23) provide the body boundary condition for the vector potential:

$$\frac{\partial A}{\partial t} = 0 \tag{25}$$

or

$$A = A_o = \text{const.} \tag{26}$$

along the body (away from the separation point).

Vorticity is introduced into the flowfield only in the vicinity of the separation locations (see discussion below). Consequently, away from the separation points

$$\Omega\Big|_{\text{body}} = 0 \tag{27}$$

is applied.

Far-Field

In the farfield, freestream conditions prevail,

$$\vec{V} = \vec{V}_\infty \tag{28}$$

or in component form:

$$\phi_x\ \Big|_\infty = u_\infty \tag{29a}$$

$$\left[\frac{\partial\phi}{\partial n} - \frac{\partial A}{\partial t}\right]_\infty = v_{n,\infty} \tag{29b}$$

$$\left[\frac{\partial\phi}{\partial t} + \frac{\partial A}{\partial n}\right]_\infty = v_{t,\infty} \tag{29c}$$

Where $\frac{\partial}{\partial n}$ and $\frac{\partial}{\partial t}$ are local normal and tangential derivatives with respect to the freestream boundary surface.

Note that either a Neuman condition on A, which specifies $\frac{\partial A}{\partial n}$, or a Dirichlet condition, which indirectly specifies $\frac{\partial A}{\partial t}$ can be applied at the far field boundary, but not both. Having chosen either of these conditions, the velocity potential boundary condition must then be modified to ensure satisfaction of Equation (29). A third alternative is chosen. The far field boundary is placed far enough away from the body such that

$$V_t^R = \frac{\partial A}{\partial n} \approx 0 \qquad (30)$$

Then by specifying a Dirichlet condition

$$A \Big|_{\infty} = A_{\infty} = \text{constant} \qquad (31)$$

which implies

$$V_n^R = \frac{\partial A}{\partial t} = 0 \qquad (32)$$

The boundary condition for the velocity potential thus becomes

$$\vec{V}_{p,\infty} = \vec{V}_{\infty} \qquad (33)$$

and this is already implemented in the existing full potential code. Equations (31) - (33) indicate that the far field flow is irrotational, consequently:

$$\Omega \Big|_{\infty} = 0 \qquad (34)$$

is also specified at the far field boundary.

Separation condition

The vorticity flux passing through a plane normal to a two-dimensional boundary layer is given to the order of approximation of boundary layer theory by

$$\int_0^{\delta} V\,\Omega\,dy = \int_0^{\delta} V\,\frac{\partial V}{\partial y}\,dy = \frac{V_e^2}{2} \qquad (35)$$

where V_e is the velocity at the edge of the boundary layer, δ.

At the separation point, it is assumed that this vorticity is "injected" into the inviscid flow field. Consequently, a vorticity flux boundary condition is applied to the vorticity transport equation at the separation location. The flux ($V_n\ \Omega$) is applied at the body surface such that

$$\int_a^b V_n \Omega\, dl = \frac{V_e^2}{2}\lambda \qquad (36)$$

is satisfied, where the integration is taken along the surface coordinate, l, in the vicinity of the separation location, $a < l < b$. Note that an empirical factor, λ, has been included to reduce the boundary layer vorticity flux. This "vortex reduction factor" is widely used in discrete vortex methods to provide better agreement between predicted and measured values. The recommended value[4] lies in the range $0.6 \leq \lambda < 1.0$.

The separation line is determined[4] by the Stratford criterion which for turbulent boundary layers states that separation occurs when

$$C_p\left(\xi\frac{dc_p}{d_{\xi}}\right)^{1/2}\left(R_{e\xi} \times 10^{-6}\right)^{-0.1} = 0.35 \sin\alpha \qquad (37)$$

where C_p is the pressure coefficient, ξ is the length of the boundary layer in the streamwise direction, and $R_{e\,\xi}$ is the Reynolds number based on this length. The separation criteria and the strength of the shed vorticity have been used successfully in many subsonic examples.[4] As a first step the same criteria are used here.

It is shown in Reference 2 that the present formulation is equivalent at subsonic speeds to the "vortex cloud" method used by Mendenhall and Perkins.[4] The main difference is that the vorticity transport equation, Equation (1), is solved by representing the vorticity flux by discrete vortices which are transported with the flow. The velocity induced by the vortices is computed from the Biot-Savart law. The strength of the vortices introduced at the separation line is determined by the same criteria as the present work, that is Equation (36). However, the location of a vortex that has just been introduced must be determined, which is achieved by ensuring that the separation line is a crossflow stagnation point. Since the discrete vortex is the integral of the vorticity over an element, the location may be regarded as the centroid of the vorticity in the element. If the vorticity flux in a time interval is uniform, then the centroid is at the center of the element; there is no flexibility in changing the centroid other than by changing the rate of change of vorticity flux in each time interval which seems to be a nonphysical artifice. Another difference between the present method and vortex cloud is that discrete vortex methods do not automatically converge as the number of vortices is increased; this introduces an element of art into the procedure which cannot be duplicated in the present method.

A Second Order Correction

In the work of Mendenhall and Perkins,[4] it is necessary to introduce the rotational increment in u due to the rotation of the vortex away from the axial direction. This additional term is necessary to obtain any kind of adequate results and is presented as an empirical correction. It is necessary to include this correction in the present theory but it is instructive to examine the idea further.

From the definition of the various vorticity components

$$w^R_y - v^R_z = \Omega_1 \qquad (38a)$$

$$u^R_z - w^R_x = \Omega_2 \qquad (38b)$$

$$v^R_x - u^R_y = \Omega_3 \qquad (38c)$$

where the superscript "R" denotes a rotational component, Ω_1 is the vorticity component in the axial direction, Ω_2 is the component in the y direction, and Ω_3 is the component in the z direction. In the computations, Ω_1 is computed. From Equation (38b)

$$u^R = \int^z (w^R_x + \Omega_2)\,dz + f(x,y) \qquad (39)$$

where f(x,y) is a function due to the integration and on differentiation

$$u^R_y = \int^z (w^R_{xy} + \Omega_{2y})\,dz + f_y \qquad (40)$$

From Equation (38a) and (38c)

$$w^R_y = \Omega_1 + v^R_z \qquad (41)$$

$$u^R_y = v^R_x - \Omega_3 = \int^z (v^R_{xz} - \Omega_{3z})\,dz \qquad (42)$$

and on substitution of Equations (41) and (42) into Equation (40)

$$f_y = \int^z \left[v^R_{xz} - \Omega_{3z} - \Omega_{1x} - v^R_{xz} - \Omega_{2y}\right] d\eta \qquad (43)$$

Since

$$\Omega_{1x} + \Omega_{2y} + \Omega_{3z} = 0$$

by definition it follows that

$$u^R = \int^z (w^R_x + \Omega_2)\,dz \qquad (44)$$

From the analysis of Klopfer and Nixon[2] it may be shown that

$$w^R_x \sim \underline{0}(\epsilon u_\infty)$$

$$(45)$$

$$\Omega_2 \sim \underline{0}(\epsilon\Omega_1) \sim \underline{0}(\epsilon^3)$$

Hence a first approximation is

$$u^R = \int^z w^R_x dz \qquad (46)$$

The point of this analysis is that the "empirical correction" of Mendenhall and Perkins[4] is actually a consistent second order extension of the theory. This extra component of velocity is incorporated into the pressure relation

$$C_p = \frac{2}{\gamma M^2_\infty} \left\{ \left[1 + \frac{(\gamma-1)}{2} M^2_\infty (1 - q^2) \right]^{\gamma/\gamma-1} - 1 \right\} \qquad (47)$$

where

$$q^2 = (u^P + u^R)^2 + (v^P + v^R)^2 + (w^P + w^R)^2 \qquad (48)$$

Numerical Methods

The governing equations, continuity, vorticity transport, vector potential Equations (14) - (19), and the Bernoulli equation are a coupled, non-linear system and are solved in an iterative manner. The numerical method used for each equation and the overall solution algorithm for the system are described in this section.

Continuity Equation

Equation (14) with S = 0 is the transonic full potential equation. An existing code, TWING[3], which solves the full potential equation in SCL form for a wing was modified to treat a general body and to include the source term, S, and the terms A_y and A_z in the Bernoulli equation.

TWING uses an implicit, approximate factorization (AF) shock-capturing scheme. Central differencing is used at subsonic points and an equivalent upwind density biasing is applied at supersonic points. For a full description of the numerical method used in TWING, see Reference 3.

The AF scheme for the full potential equation can be written

$$NC^n + \omega L\phi^n = 0 \qquad (49)$$

where $L\phi = 0$ represents the full potential equation in operator form. The ω is a relaxation parameter, C^n is the correction term $(\phi^{n+1} - \phi^n)$, $L\phi^n$ is the residual, and N is an operator representing the AF splitting. The source term was incorporated into the AF scheme by replacing the residual $L\phi^n$ with $(L\phi^n - S^n)$ giving

$$NC^n - \omega(L\phi^n - S^n) = 0 \qquad (50)$$

and S^n is evaluated according to Equation (15). The velocity terms appearing in the Bernoulli Equation (5) were modified to include A_y and A_z as indicated in Equation (4). No further modifications were required.

Vorticity Transport Equation

The vorticity transport equation is hyperbolic with ξ as the time-like variable. Consequently, a marching-type procedure is used to solve this equation. Central differencing is used with a Beam and Warming-type [5] solution algorithm that is derived next.

The vorticity transport equation (16) is first rewritten as

$$\hat{\Omega}_\xi = -\left[(V\hat{\Omega})_\eta + (W\hat{\Omega})_\zeta\right] \qquad (51)$$

Trapezoidal differencing is used in the ξ-direction, and second-order central differencing in the η and ξ directions, resulting in:

$$\frac{\hat{\Omega}_{i+1} - \hat{\Omega}_i}{\Delta\xi} = -1/2\left\{\left[\delta_\eta(V\hat{\Omega}) + \delta_\zeta(W\hat{\Omega})\right]_{i+1} + \left[\delta_\eta(V\hat{\Omega}) + \delta_\zeta(W\hat{\Omega})\right]_i\right\} \qquad (52)$$

where "i" is the grid index in the ξ-direction; "j" and "k," the indices in the η and ζ directions, respectively are implied in Equation (52). The central difference operators are

$$\delta_\eta(\ )_{ijk} = 1/2\left\{(\ )_{i,j+1,k} - (\ )_{i,j-1,k}\right\} \qquad (53a)$$

and

$$\delta_\zeta(\ )_{ijk} = 1/2\left\{(\ )_{i,j,k+1} - (\ )_{i,j,k-1}\right\} \qquad (53b)$$

Equation (52) can be rearranged:

$$\left\{I + \frac{\Delta\xi}{2}\left[\delta_\eta V_{i+1} + \delta_\zeta W_{i+1}\right]\right\}\hat{\Omega}_{i+1} = \left\{I - \frac{\Delta\xi}{2}\left[\delta_\eta V_i + \delta_\zeta W_i\right]\right\}\hat{\Omega}_i \qquad (54)$$

Equation (54) is then factorized giving,

$$\left(I + \frac{\Delta\xi}{2}\delta_\eta V_{i+1}\right)\left(I + \frac{\Delta\xi}{2}\delta_\zeta W_{i+1}\right)\hat{\Omega}_{i+i} = \left(I - \frac{\Delta\xi}{2}\delta_\eta V_i\right)\left(I - \frac{\Delta\xi}{2}\delta_\zeta W_i\right)\hat{\Omega}_i + D_i \qquad (55)$$

Note that this equation is linear in $\hat{\Omega}$, since provisional values of V_{i+1} and W_{i+1} are known when Equation (55) is solved (see discussion below concerning the global iteration strategy). The right hand side of Equation (55) has also been factored to minimize the factorization error.

D_i, in Equation (55), represents an added explicit fourth-order dissipation term which is necessary to stabilize the integration in ξ. The dissipation also provides a spatial smoothing of the vorticity which inhibits the odd-even decoupling phenomena, characteristic of central-differenced, convective-transport equations.

The formula used for D_i is taken from Reference 6:

$$D_i = \epsilon J_i^{-1}(\delta^4_\eta + \delta^4_\zeta)(\hat{\Omega}J)_i \qquad (56)$$

where δ^4_η and δ^4_ζ are centered, fourth differences, e.g.:

$$\delta^4_\eta\Omega = \Omega_{j-2} - 4\Omega_{j-1} + 6\Omega_j - 4\Omega_{j+1} + \Omega_{j+2} \qquad (57)$$

and ϵ, the fourth order smoothing coefficient, is a constant.

The fourth order difference terms, Equation (57), are modified near the boundaries and are discussed below in the results section.

To advance Equation (55), the following two step procedure is executed.

$$1: \{I + \frac{\Delta\xi}{2}\delta_\eta V_{i+1}\} \hat{\Omega}^{*}_{i+1} = R_i \tag{58a}$$

$$2: \{I + \frac{\Delta\xi}{2}\delta_\zeta W_{i+1}\} \hat{\Omega}_{i+1} = \hat{\Omega}^{*}_{i+1} \tag{58b}$$

where R_i = right-hand-side of Equation (55). Steps 1 and 2 require the inversion of scalar tridiagonal matrices.

Vector potential equation

The vector potential is a Poisson equation that is solved separately in each crossflow plane. Second order central differencing is used for both first and second order derivatives in Equation (19). Successive over-relaxation is used as the iteration scheme.

The second order metric derivatives appearing in Equation (19) are evaluated by using the chain rule, e.g.:

$$\eta_{yy} = (\eta_y)_\eta \eta_y + (\eta_y)_\zeta \zeta_y \tag{59}$$

(recall that $\xi \neq f(y)$). Central differencing is used to approximate the terms like $(\eta_y)_\eta$.

Treatment at grid singularities

Two different mesh topologies were used in the study, an H-grid and a polar grid. At the grid singularities, the dependent variables were taken as simple averages of neighboring values in the same crossflow plane.

Global iteration strategy

The solution of the coupled system of Equations (14), (16), and (19) is achieved by sequentially iterating each individual equation in turn. A single pass through all the equations is a global or outer iteration; inner iterations are performed on the velocity potential and vector potential equations. Because the inner iteration algorithms were designed to be stable and convergent, the global iteration process is expected to be similarly well behaved.

One global iteration consists of the following steps:

1. Iterate on the velocity potential equation (50). Initially $S = A_z = A_y = 0$.

2. Determine the incipient separation plane $\xi = \xi_{is}$ using the Stratford criterion in Equation (37). This is the first upstream plane where vorticity will be shed.

3. March the vorticity transport and vector potential equations downstream from ξ_{is} to ξ_{max} where ξ_{max} is end value of ξ.

   (a) $\xi_i = \xi_{is}$

   (b) Determine the separation location from the Stratford criterion and evaluate the vorticity flux to be "shed" to ξ_i crossflow plane according to Equation (36).

   (c) Advance vorticity from plane ξ_i to ξ_{i+1}. Since vorticity transport and vector potential equations are coupled through $\vec{V}^R$, this is an iterative procedure. n = 1.

      (i) Step vorticity transport Equation (51) from plane ξ_i to ξ_{i+1}.

      (ii) Iterate vector potential Equation (19) for ξ_{i+1} plane.

      (iii) Calculate total velocity for ξ_{i+1} plane: $\vec{V}^n_{i+1} = (\vec{V}^P + \vec{V}^R)^n_{i+1}$

      (iv) Check for convergence on total velocity in ξ_{i+1} plane: if $|\vec{V}^n_{i+1} - \vec{V}^{n-1}_{i+1}| \sim 0$ iteration converged, otherwise continue iterating (n = n + 1, go to (i) above).

   (d) If at last crossflow plane, $\xi_{i+1} = \xi_{max}$ continue, otherwise continue marching vorticity downstream (go to (c) above).

4. Calculate the source term, S, Equation (15), then continue iterating velocity potential equation (go to 1).

The number of inner iterations performed on the velocity and vector potential equations are arbitrary and are determined by experience. Note that this global iteration strategy has not been optimized in terms of convergence rate or operation count. Its primary purpose is to provide a method for determining the solution to the coupled system of equations.

CONVECTION OF A SINGLE VORTEX

The convection of a single vortex in the potential flowfield about an axisymmetric body was used as a test problem for debugging during the early development of the computer programs. An interesting numerical effect was discovered which raises some questions regarding the accuracy of numerical simulations of vortex flows.

A conservation equation for the circulation will first be derived from the vorticity transport equation. Then, an equivalent numerical conservation equation will be derived from the difference equations used to approximate the vorticity transport equation. Finally, results of the test problem will be given to illustrate the degree to which circulation is conserved in a calculation.

If the vorticity transport equation, Equation (1), is integrated over a crossflow plane, one obtains

$$\int_A \frac{\partial \Omega}{\partial x}\, dA + \int_A \vec{\nabla} \cdot \left[\vec{V}_{xf}\Omega\right] dA = 0 \qquad (60)$$

where

$$dA = dydz$$

$$\vec{V}_{xf} = \frac{v}{u_\infty}\vec{j} + \frac{w}{u_\infty}\vec{k}$$

and $\vec{\nabla}$ is a two-dimensional gradient operating in the y and z directions. Applying the divergence theorem and noting that $A \neq f(x)$, Equation (60) becomes:

$$\frac{\partial}{\partial x}\int_A \Omega dA + \int_l v_n \Omega dl = 0 \qquad (61)$$

where in the second integral, $v_n\,\Omega$ is the vorticity flux normal to l, the boundary of the flowfield in the crossflow plane. Notice that the first integral is the definition of the circulation, Γ, so that Equation (61) can be expressed as:

$$\frac{\partial \Gamma}{\partial x} + \int_l v_n \Omega dl = 0 \qquad (62)$$

Equation (62) indicates that if there is no vorticity flux at the boundaries of the flowfield, then the circulation is conserved. The algorithm used to solve the vorticity transport equation is next analyzed to determine to what extent circulation is numerically conserved.

The finite difference equations which determine the convection of vorticity over one step, $\Delta\xi$, in the streamwise direction are represented by Equation (55). Expanding and rearranging Equation (55) gives:

$$\overset{\#1}{\hat{\Omega}_{i+1}} = \overset{\#2}{\hat{\Omega}_i} + \frac{\Delta\xi}{2}\left\{\overset{\#3}{\delta_\eta\left[\hat{F}_i + \hat{F}_{i+1}\right]} + \overset{\#4}{\delta_\zeta\left[\hat{G}_i + \hat{G}_{i+1}\right]}\right\} + \overset{\#5}{D_i} + \overset{\#6}{\frac{(\Delta\xi)^2}{4}\left\{\delta_\eta V_i \delta_\zeta \hat{G}_i - \delta_\eta V_{i+1}\delta_\zeta \hat{G}_{i+1}\right\}} \qquad (63)$$

where

$$\hat{F} = V\hat{\Omega} \text{ and } \hat{G} = W\hat{\Omega}$$

(The last term on the right hand side of Equation (63) is the approximate factorization error.)

The numerical analog of the circulation conservation statement, Equation (62), is obtained by summing each term in Equation (63) over all interior grid points in the respective crossflow plane. If the result of such a summation involves only boundary terms, the numerical method is said to be conservative. This scheme, Equation (63), will be analyzed below to determine if it is conservative. The summation of each term in Equation (63) will be considered separately, beginning with the left hand side term.

Using j as the grid point index for the circumferential direction, η, and k as the index for the normal direction, ζ, $\hat{\Omega}_{i+1}$ is summed over all interior points in the i+1 plane giving:

$$\sum_{j=1}^{jmax-1}\sum_{k=2}^{kmax-1}\hat{\Omega}_{i+1,j,k} = \sum_{j=1}^{jmax-1}\sum_{k=2}^{kmax-1}\left[\frac{\Omega}{J}\right]_{i+1,j,k} \qquad (64)$$

Limits on the summation over j indicate that the grid is periodic in this direction. The inverse of the Jacobian, J^{-1} represents the elemental area in the crossflow plane associated with a grid point, thus $J^{-1} = \Delta A$ so that Equation (64) can be rewritten:

$$\sum_j \sum_k \hat{\Omega}_{i+1,j,k} = \sum_j \sum_k (\Omega\Delta A)_{i+1,j,k} \qquad (65)$$

(The limits on the summation in Equation (65) and all following equations in this section are implied to be the same as in Equation (64), i.e. to include all interior grid points) The right hand side of Equation (65) is a numerical approximation to $\int \Omega dA$, which as noted above, is equal to the circulation, Γ. Consequently,

$$\sum_j \sum_k \hat{\Omega}_{i+1,j,k} = \Gamma_{i+1} \qquad (66)$$

and therefore the summation of $\hat{\Omega}_{i+1}$ over all interior grid points represents the circulation contained in the i+1-th crossflow plane. Similarly, Γ_i is obtained by summing $\hat{\Omega}_i$ over all points in the i-th plane.

Next consider the summation of either component of term #3 in Equation (63). Making use of the difference formula for δ_η in Equation (53) and periodicity in the j-direction, it can be shown that:

$$\sum_j \sum_k \delta \hat{F}_{i,j,k} = 0 \tag{67}$$

The difference term, $\delta_\eta \hat{F}$ is therefore conservative.

For $\delta_\zeta \hat{G}_i$ in term #4 of Equation (63), it can be shown that:

$$\sum_j \sum_k \delta_\zeta \hat{G}_{i,j,k} = \sum_j \left[- \frac{(\hat{G}_{i,j,1} + \hat{G}_{i,j,2})}{2} + \frac{(\hat{G}_{i,j,kmax-1} + \hat{G}_{i,j,kmax})}{2} \right] \tag{68}$$

Notice that the two terms on the right hand side represent approximations to boundary fluxes, located at (i,j,k+1/2) and (i,j,kmax-1/2), respectively. Thus in the standard nomenclature, the $\delta_\zeta \hat{G}$ term is also conservative.

It can also be shown that the summation of the approximate factorization error, term #6 in Equation (63), is identically zero. Using Eqns. (66) - (68), the result of summing Equation (63) over all interior grid points is

$$\Gamma_{i+1} = \Gamma_i + \frac{\Delta \xi}{2} \sum_j \left[- \frac{(\hat{G}_{i,j,1} + \hat{G}_{i,j,2})}{2} + \frac{(\hat{G}_{i,j,kmax-1} + \hat{G}_{i,j,kmax})}{2} \right]_{i=i,i+1} + \sum_j \sum_k D_i \tag{69}$$

It is thus found that the numerical scheme, Equation (55), should conserve the circulation, provided that the dissipation term, D_i, is also conservative. This term will be considered next.

The dissipation term initially used in the program is given by Equation (56), as recommended by Steger and Pulliam.[6] However, this formulation is not conservative because the inverse Jacobian, J^{-1}, appears outside of the difference operators. This situation is remedied by removing the inverse Jacobian and operating directly on $\hat{\Omega}$. In other words:

$$\delta_\eta^4 \hat{\Omega} = \hat{\Omega}_{j-2} - 4\hat{\Omega}_{j-1} + 6\hat{\Omega}_j - 4\hat{\Omega}_{j+1} + \hat{\Omega}_{j+2} \tag{70a}$$

and

$$\delta_\zeta^4 \hat{\Omega} = \hat{\Omega}_{k-2} - 4\hat{\Omega}_{k-1} + 6\hat{\Omega}_k - 4\hat{\Omega}_{k+1} + \hat{\Omega}_{k+2} \tag{70b}$$

Note that for applying the ζ-direction term, $\delta_\zeta^4 \hat{\Omega}$, at interior grid points immediately adjacent to a boundary, a formula different from the symmetric formula, Equation (70b), must be used. (Since the grid is periodic in the j-direction, the interior point formulation for $\delta_\eta^4 \hat{\Omega}$, Equation (70a), does not need to be modified.) Various boundary point formulas were tried including a second-order difference and also a non-symmetric fourth-order term. However with these formulations, summation of the dissipation term results in a non-zero linear combination of near-boundary $\hat{\Omega}$ values which represents an approximation to a third derivative normal to the boundary. This boundary term can become quite large when there are significant gradients in the vorticity, causing the term $\sum_j \sum_k D_i$ in the numerical conservation equation, Equation (69), to act as a source or sink of circulation, depending on the term's sign.

To remedy this problem, the following boundary point formulas were derived:

$$\delta_\zeta^3 \hat{\Omega} \Big|_{k=2} = -\hat{\Omega}_1 + 3\hat{\Omega}_2 - 3\hat{\Omega}_3 + \hat{\Omega}_4 \tag{71a}$$

$$\delta_\zeta^3 \hat{\Omega} \Big|_{k=kmax-1} = \hat{\Omega}_{kmax-3} - 3\hat{\Omega}_{kmax-2} + 3\hat{\Omega}_{kmax-1} - \hat{\Omega}_{kmax} \tag{71b}$$

Using Equations (71) with Equation (70), results in

$$\sum_j \sum_k D_{ijk} = 0 \tag{72}$$

and makes the dissipation term conservative. By substituting Equation (72) into Equation (69), one obtains:

$$\Gamma_{i+1} = \Gamma_i + \frac{\Delta\xi}{2} \sum_{j}^{jmax-1} \left[\frac{(\hat{G}_{i,j,1} + \hat{G}_{i,j,2})}{2} \right. \tag{73}$$

$$\left. + \frac{(\hat{G}_{i,j,kmax-1} + \hat{G}_{i,j,kmax})}{2} \right]_{i=i,i+1}$$

This final equation demonstrates that the numerical approximation, Equation (55) to the vorticity transport equation conserves circulation to within the error of the boundary flux approximations.

The test problem used to demonstrate the conservation properties of the numerical method will be described next. An axisymmetric body used in the simulation consists of an 8-caliber cylinder having a 3-caliber tangent-ogive cylindrical nose. A base having the same shape as the nose was included to close the body. A grid was constructed about this body having 41 x 21 x 41 points in the streamwise, circumferential, and body-normal directions, respectively. Views of the grid in the symmetry and a crossflow plane are give in Figures 1(a) and 1(b), respectively.

Calculations were made at a free stream Mach number, $M_\infty = 0.3$, and angle of attack, $\alpha = 15°$. The potential flowfield was first calculated by solving the full potential equation. A single vortex was then placed in this flowfield in a crossflow plane located near the beginning of the straight section by specifying a non-zero value of vorticity at a single grid point in the crossflow plane. Zero-normal vorticity flux was specified on all boundaries in all crossflow planes. The vortex was convected in the potential flowfield by solving the vorticity transport equation. The vortex was advanced twenty streamwise steps downstream to a crossflow plane located near the end of the straight section. Several calculations were made to investigate the effect of the dissipation on the conservation of circulation.

In the first set of calculations, the vortex was placed at a location approximately one body diameter away from the body surface in the initial, upstream crossflow plane. This put the vortex twelve grid points, radially, away from the body, indicated by the symbol, ⊗, in Figure 1b. Two calculations were made; the first using the non-conservative dissipation term, Equation (56), the second using the fully conservative dissipation term, Equations (70) and (71). The calculated circulation in each crossflow plane was evaluated by summing $\hat{\Omega}$ over all interior points in the plane, according to Equation (65). The ratio of the circulation in the final and initial crossflow planes was evaluated to measure the degree of conservation of circulation. Due to the specification of zero-normal vorticity flux at the boundaries, the initial circulation should ideally be preserved. The results are presented in Table 1.

With the non-conservative dissipation term, Case No. 1, there is an incremental loss of circulation as the vortex is advanced at each crossflow plane, resulting in a significant net loss (14%) in circulation after the vortex has been advanced to the end of the straight section. Using the conservative dissipation term, the loss in circulation is significantly less, only 2% of the initial value. However, no loss in circulation is expected since the numerical method has been shown above to be "conservative." This apparent anomaly will be discussed below.

Another series of calculations were made with the location of the initial vortex much closer to the body, in this case only four grid points radially away from the body surface, indicated by the symbol, X, in Figure 1b. Both methods show a much larger loss in circulation in this instance, Case No. 2, with a 54% loss with the non-conservative, and a 22% loss with the conservative dissipation term. The latter loss in circulation is unexpectedly large for a numerical scheme which is supposed to conserve circulation.

The source of the loss in circulation was found to be the boundary-normal vorticity flux term, $\hat{G}_{i,j,1/2}$:

$$\hat{G}_{i,j,1/2} = \frac{\hat{G}_{i,j,1} + \hat{G}_{i,j,2}}{2} \tag{74}$$

which appears in Equation (73). Recall that zero-normal vorticity flux is specified on the crossflow plane boundaries, so that $\hat{G}_{i,j,1} = 0$ at the body surface, defined by $k=1$. (Similarly $\hat{G}_{i,j,kmax} = 0$ is specified at the far field boundary, $k = kmax$.) However, since $\hat{G}_{i,j,2}$ is a calculated value, it can attain a non-zero value, particularly when the vorticity is convected close to the body, and serve as a boundary flux of vorticity out of the flowfield. This explains why the loss in vorticity is much less when the vortex is located away from the flowfield boundaries.

Although the numerical method was shown to be conservative in the standard sense, the occurrence of a non-zero boundary flux with zero flux specified is an artifact of the finite difference scheme. The error which is induced, the loss in circulation, can be minimized, although not totally eliminated, by reducing the mesh spacing in the ζ-direction at the boundary surface. Alternatively, the problem can be completely avoided by using a finite volume formulation, where boundary fluxes can be exactly specified. In any case, for flows which critically depend on the vorticity contained within the flowfield, it is of utmost importance that the numerical method most nearly maintain conservation of circulation to ensure a high degree of accuracy.

RESULTS

This section presents computational results made with the computer program, TSBVRT, (transonic, slender-body, vortical flows) which uses the algorithm described above. Comparisons are made with experimental data. Results are first described for subsonic flow over a cylindrical body, followed by results for subsonic and a transonic flow over a body having an elliptical-shaped cross section.

The body for the subsonic case, an ogive-cylinder with a 3-caliber nose and 8-caliber body is the same as described in the previous section. The flow conditions are also the same: free stream Mach number, $M_\infty = 0.3$ and angle of attack, $\alpha = 15^\circ$. This particular model and flow conditions were selected to correspond to a set of available experimental data (Ref. 7).

The grid used for this case is the 41 x 21 x 41 grid that also was described above and is illustrated in Figure 1. Flow calculations were performed in the following manner. First, since TSBVRT did not have the Stratford separation criteria, Equation (37), programmed, the separation line was determined from a calculation made with the VTXCLD program (Ref. 8) for the same body and set of flow conditions. VTXCLD, a discrete vortex method, compares well with this experimental data and also has the Stratford separation criteria built-in.

Using the VTXCLD-determined separation line location, the vortical flow field was calculated with TSBVRT. The vorticity flux at the separation location in each crossflow plane was specified at a single grid point according to Eqn. (36). The boundary layer edge velocity, V_e was taken to be the potential velocity on the body surface at the separation location in each respective crossflow plane. The vortex reduction factor, $\lambda = 0.45$ was found to give the best agreement with the experimental data.

Calculated surface pressures and corresponding velocity fields at two crossflow stations are shown in Figures 2 and 3, respectively. On the abscissa for the pressure plots, $\beta = 0^\circ$ corresponds to the windward meridian and $\beta = 180^\circ$ to the leeward meridian. Also plotted in these figures are the corresponding pressures for both experimental and VTXCLD results. As the pressure curves indicate, the current results are found to agree fairly well with both experimental data and the VTXCLD calculation. Note in the velocity plots the vortical flowfields located on the leeward side of the cylinder. The close proximity of the calculated vortices to the body is responsible for the correct modification of the pressure distribution on the upper surface, $\beta \approx 120^\circ - 180^\circ$.

The agreement between the present results and vortex cloud is sometimes not as good as would be expected from two mathematically similar formulations as can be seen in Figure 2. A test of both methods indicated that the dominant cause of the discrepancy is the computation of the second order term u^R which is due to the tilting of the vortex. A comparison of this term at $x/D = 7.5$ computed by both methods is shown in Table 2. It may be seen that at the location of the greatest error in surface pressures, $\theta \sim 120^\circ$, the present correction is much less than that computed by the vortex cloud method. This error occurs below the vortex feeding sheet. The second order correction is found by an integral of the vortical velocity w^R. If the vortex sheet is diffused by the calculation, the integral from the outer to inner boundary may be expected to be independent of the diffuse nature of the sheet if the total vorticity along the line of integration is conserved since it does not depend on the details of the flow, only the end points. Since the present method is conservative and integrates the vorticity to obtain the correction there should be no significant error due to numerical diffusion of the vortex. Consequently, the cause of the difference is not clear at this stage.

The second body investigated in this study has a 2:1 elliptical cross section with a parabolic planform. This body has been experimentally investigated (Ref. 9) at subsonic, transonic and supersonic free stream speeds. A grid was constructed about the body with 41 x 81 x 23 points in the streamwise, circumferential, and body-normal directions, respectively. Views of the grid in the planform plane and also in a crossflow plane are given in Figures 4(a) and 4(b), respectively. Note in Figure 4(a) that the body is closed with a simple circular arc base. Note also that all dimensions have been normalized to 2A, the maximum major axis of the elliptical body. The total length of the body, not including the base, is $L/2A = 4.3$.

The first calculation made is for a subsonic flow with free stream Mach number, $M_\infty = 0.4$ and angle of attack, $\alpha = 16.3^\circ$. As was done with the circular body, VTXCLD was run first to obtain the location of the separation line. However for the elliptic body, it is relatively easy to infer the separation line from the experimental data. The incipient separation plane can be estimated by assessing where the measured surface pressures begin to vary from the pressures obtained from a potential flow computation. Downstream of this location, the flow separates on the shoulder of the body. The separation point was treated as above, except that in this case, the vortex reduction factor, $\lambda = 0.60$ gave the best agreement with the experimental data.

Surface pressures computed at several axial stations are plotted against the experimental data and also the VTXCLD results in Figure 5. On the abscissa in these curves, $\Phi = 0^\circ$ corresponds to the leeward meridian and $\Phi = 180^\circ$ to the windward meridian. Agreement with the data for both TSBVRT and VTXCLD computations is not as good for this body; however, TSBVRT appears to capture the correct trend of the data. The cause of the discrepancy between predictions and data is not known at this time. Grid refinement, especially in the body-normal direction may improve the accuracy of the calculation. To illustrate the vortical flow field computed with TSBVRT, the velocity field is shown in Figure 6 for the crossflow plane at X/2A = 3.1.

The second calculation made with the elliptic body is a transonic flow with free stream Mach number, $M_\infty = 0.95$ and angle of attack, $\alpha = 16.9°$. The separation line was the same as in the previous calculation, except here, $\lambda = 0.90$. The computed surface pressures at several axial stations are plotted along with experimental values in Figure 7. The predicted results have about the same degree of agreement with the data as in the previous case.

For this flow, the free stream Mach number is not large enough to produce crossflow shocks; however, a shock does occur on the upper surface of the base. Figure 8 plots vorticity contours just upstream and downstream of this shock. This latter result demonstrates the ability of the current method to compute vortical flowfields with shock waves.

Concluding Remarks

The equations of Klopfer and Nixon[2] have been coded. The computer code is a considerably developed version of a potential code, TWING. Results for bodies at high angle of attack and at subsonic and transonic Mach numbers have been obtained and compared to experiment, and, for subsonic flow, to a discrete vortex method. The equations of Klopfer and Nixon assume that only one component of vorticity is important but the present study shows that the vorticity component due to the vortex rotating away from the body must be included. This, in fact, is introduced as an empirical convection in the discrete vortex method. In the present work this is shown to be a second order correction to the basic theory.

There is considerable discrepancy between the results of the present theory and both the discrete vortex method and experimental data. Since both prediction methods solve the same equations but with different algorithms, it suggests that the flow may be very sensitive to errors.

It has also been found that numerical errors can dissipate an isolated vortex by a considerable amount, a fact that suggests further work in algorithm development. It is suggested that the use of a finite volume method would remedy this problem.

References

1. Klopfer, G. H. and Nielsen, J. N.: Computational Fluid Dynamics Application to Missile Aerodynamics. Paper No. 3 in AGARD CP-336, Missile Aerodynamics, September 1982.
2. Klopfer, G. H. and Nixon, D.: Transonic Flows with Vorticity Transport Around Slender Bodies. AIAA Journ., Vol. 27, No. 10, October 1989, pp. 1461-1464.
3. Holst, T. L.: Fast, Conservative Algorithm for Solving the Transonic Full-Potential Equation. AIAA Journ., Vol. 18, No. 12, December 1980, pp. 1431-1439.
4. Mendenhall, M. R. and Perkins, S. C., Jr.: Vortex Cloud Model for Body Vortex Shedding and Tracking. Tactical Missile Aerodynamics, ed. by M. J. Hemsch and J. N. Nielsen, Vol. 104 Progress in Astronautics and Aeronautics, 1986, pp. 519-571.
5. Beam, R. and Warming, R. F.: An Implicit Finite - Difference Algorithm for Hyperbolic Systems in Conservation Law Form. J. Comp. Phys., Vol. 22, 1976, pp. 87-110.
6. Pulliam, T. H. and Steger, J. L.: Implicit Finite Difference Simulations of Three-Dimensional Compressible Flow, AIAA Journ., Vol. 18, No. 2, February 1980, pp. 159-167.
7. Tinling, B. E. and Allen, C. Q.: An Investigation of the Normal-Force and Vortex-Wake Characteristics of an Ogive-Cylinder at Subsonic Speeds. NASA TN D-1297, April 1962.
8. Mendenhall, M. R. and Lesieutre, D. J.: Prediction of Vortex Shedding from Circular and Noncircular Bodies in Subsonic Flow. NASA CR-4037, January 1987.
9. Sellers, Marvin E.: Pressure Test of Three Elliptic Missile Body Configurations. AEDC-TSR-85-P19, October 1985.

Table 1
Convection of a Single Vortex
Check on Conservation of Circulation

		$(1 - \Gamma_{final}/\Gamma_{initial})$	
Case No.	Ω initial location	Non-conservative dissipation	Conservative dissipation
1	1 diameter from body surface	.14	.02
2	close to body surface	.54	.22

Table 2
Second Order Correction Term at x/D = 7.5

θ	VTXCLD	Present Results, Equation (46)
90	-0.0018	0.0
100	0.0031	0.0035
110	0.0484	0.0211
120	0.1095	0.0438
130	0.1042	0.0798
140	0.0931	0.1201
150	0.0864	0.1205
160	0.0677	0.1039
170	0.0938	0.0629
180	0.0999	0.0000

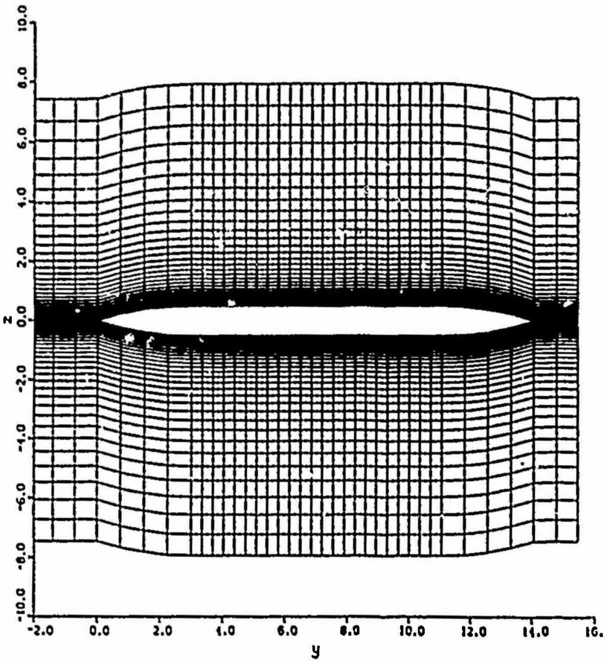

(a) Symmetry plane

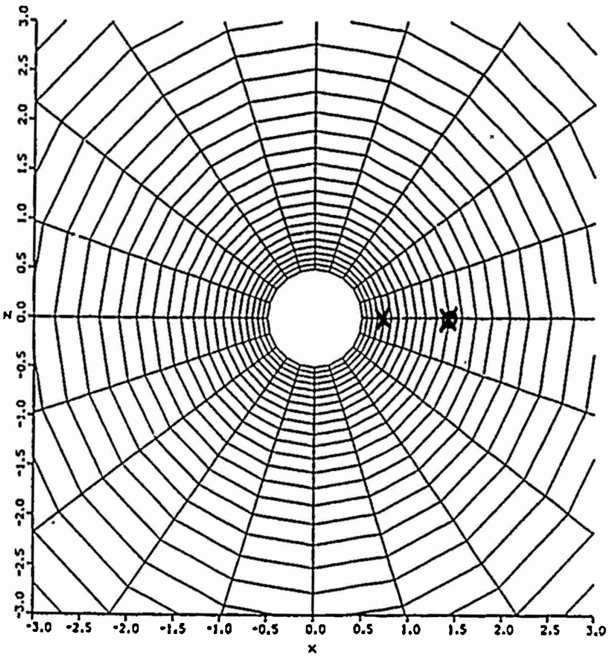

(b) Crossflow Plane

Figure 1. - Grid for Axisymmetric Body.

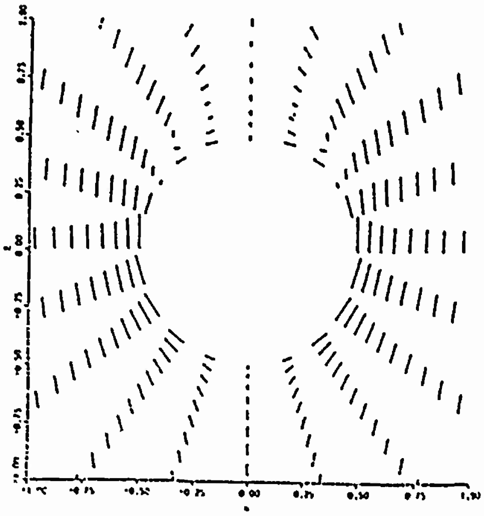

(a) velocity field

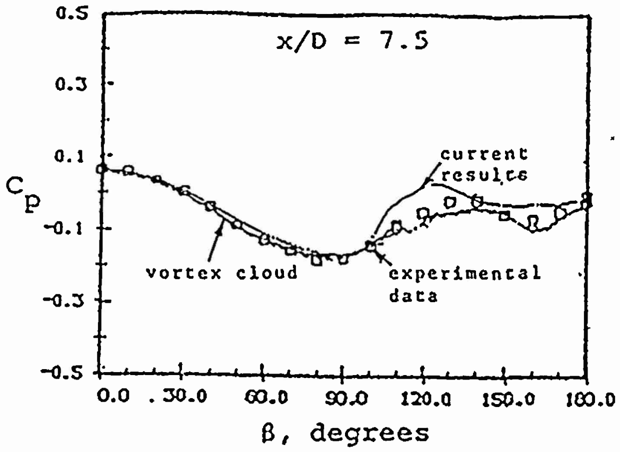

(b) surface pressures

Figure 2. - Results for Axisymmetric Body at x/D = 7.5.

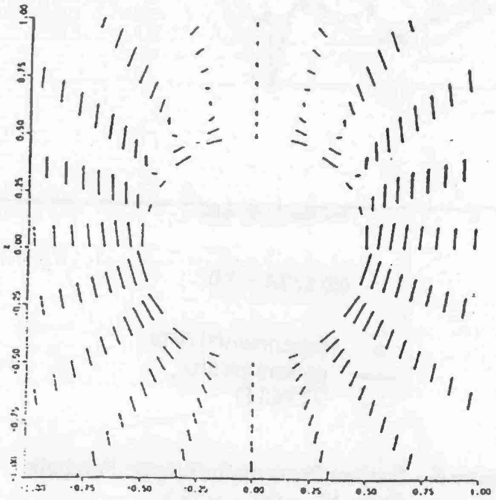

(a) velocity field

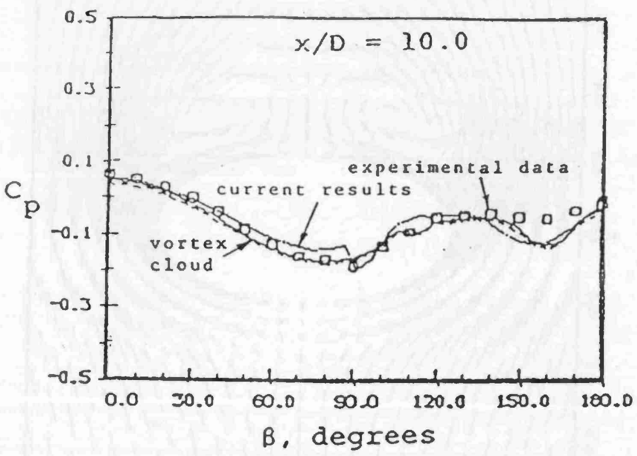

(b) surface pressures

Figure 3. - Results for Axisymmetric Body at x/D = 10.

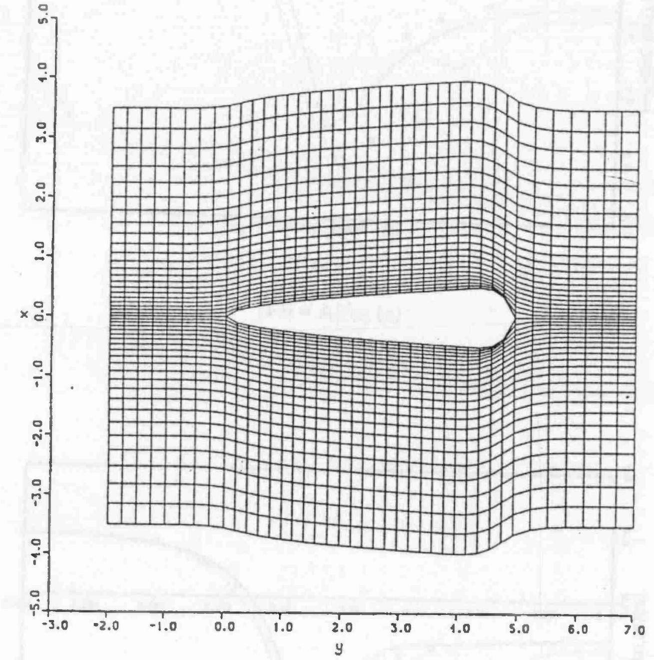

(a) Planform View

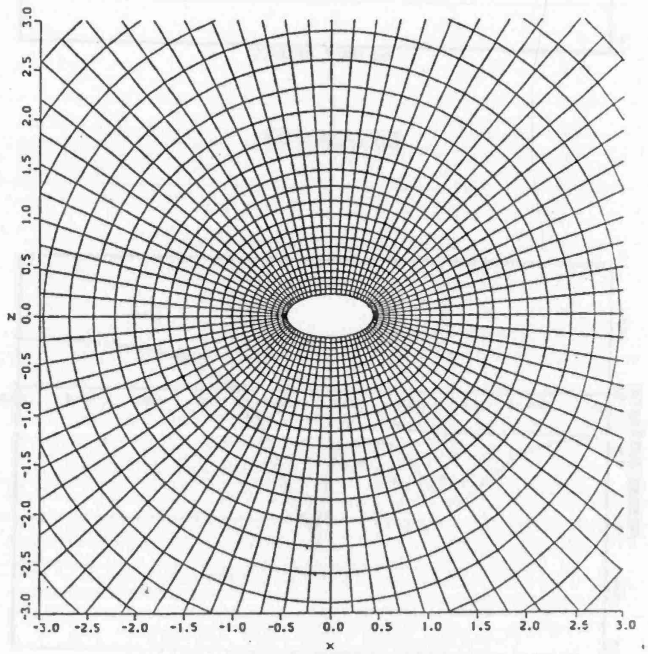

(b) Crossflow Plane

Figure 4. - Grid for Elliptic-Parabolic Body.

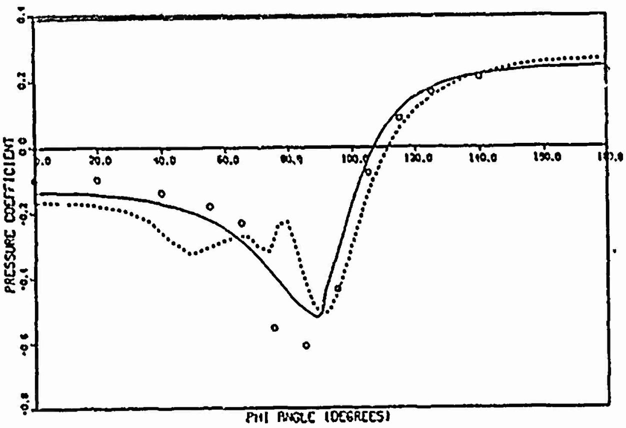

(a) x/2A = 0.4

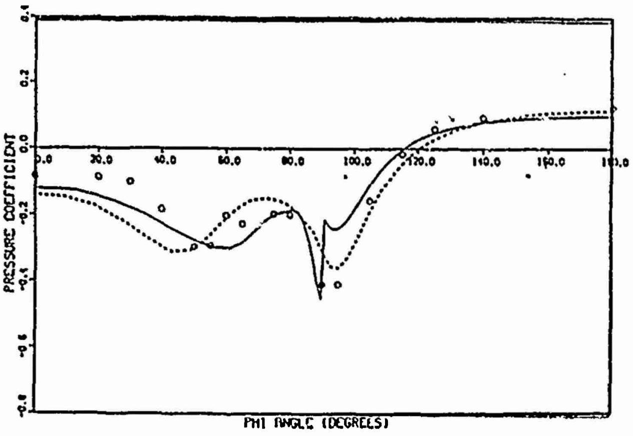

(d) x/2A = 3.0

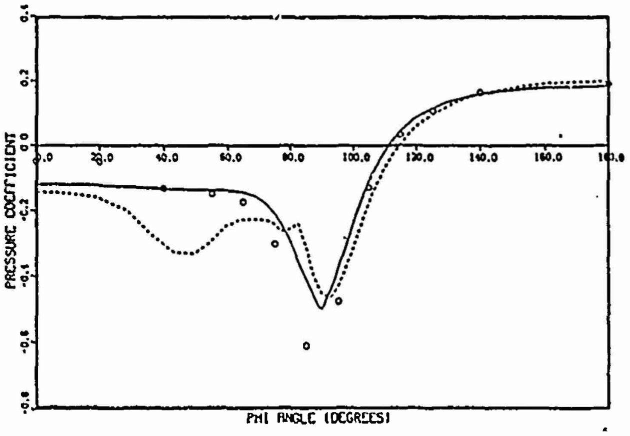

(b) x/2A = 0.8

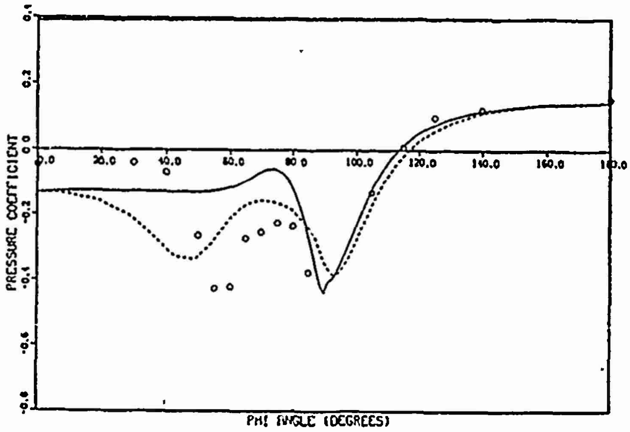

(c) x/2A = 2.0

o experimental data
—— present results
----- VTXCLD

Figure 5. - Surface Pressure for Elliptic-Parabolic Body, $M_\infty = 0.4$, $\alpha = 16.3$.

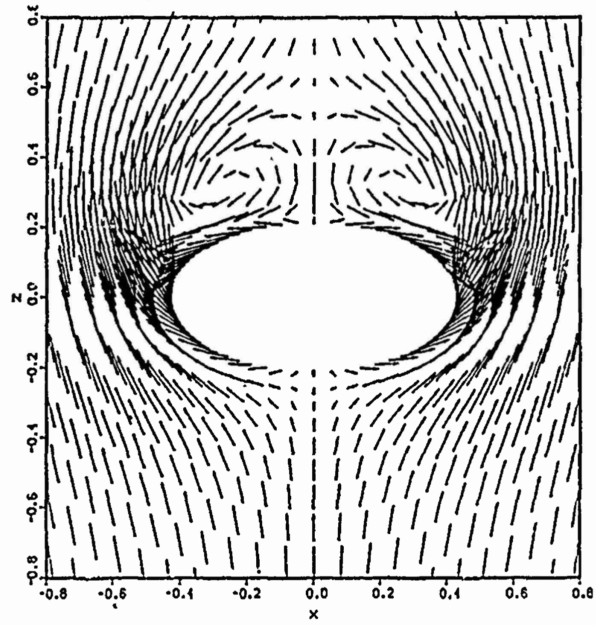

Figure 6. - Vortical Flow Field at x/2A = 3.1.

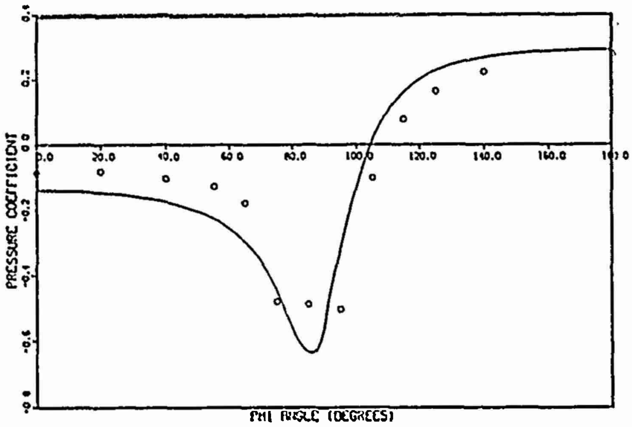

(a) x/2A = 0.4

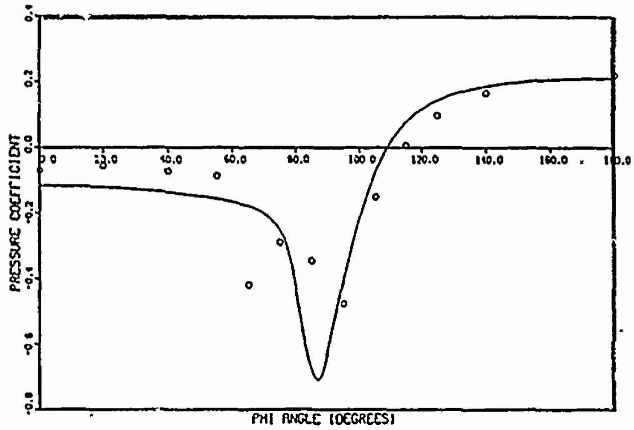

(b) x/2A = 0.8

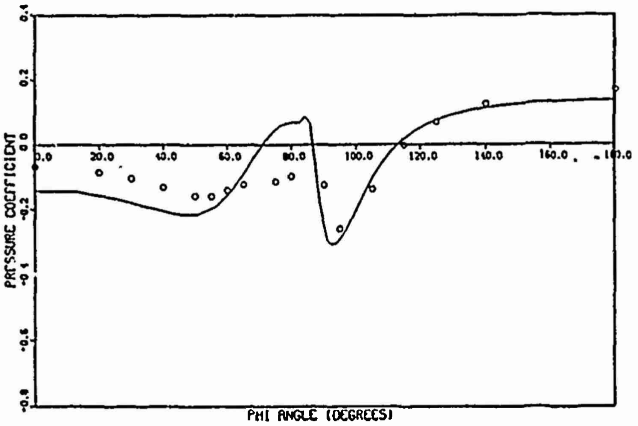

(d) x/2A = 3.0

o experimental data
—— present results

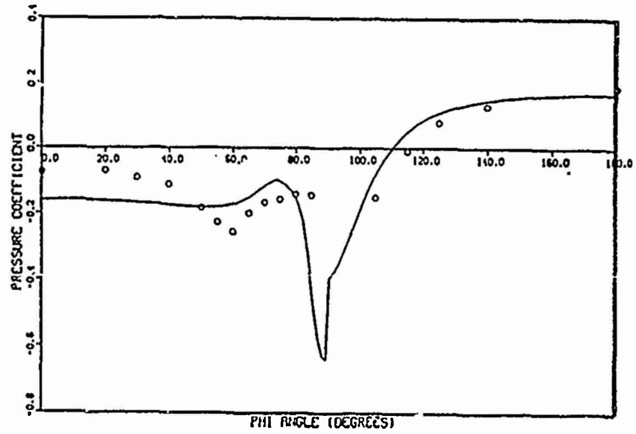

(c) x/2A = 2.0

Figure 7. - Surface Pressures for Elliptic-Parabolic Body, $M_\infty = .95$, $\alpha = 16.9$.

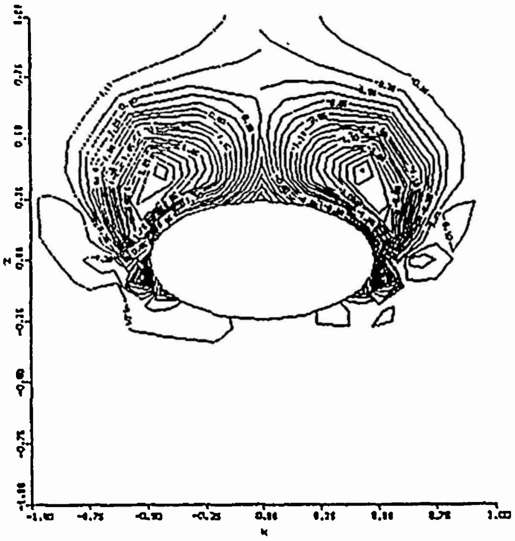

(a) upstream of shock

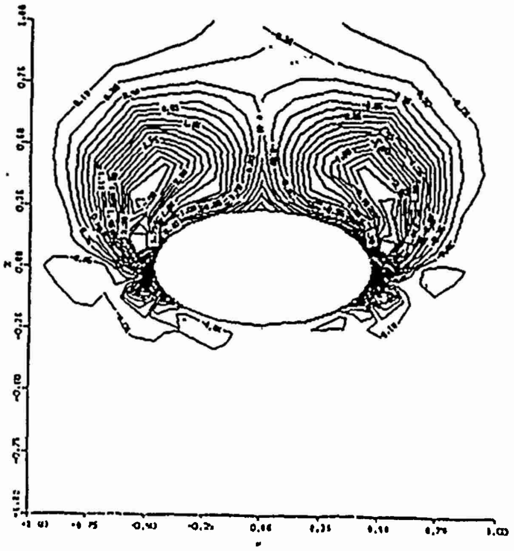

(b) downstream of shock

Figure 8. - Vorticity Distributions for Elliptic-Parabolic Body.

THE EFFECT OF VORTEX ROTATION ON THE FLOW AROUND A MISSILE AT VERY HIGH ANGLES OF ATTACK

David Nixon*
Nielsen Engineering & Research, Inc.
Mountain View, CA 94043-2287

Introduction

The problem of predicting vortical flow around a missile can be solved by using[1] the Navier-Stokes equations, which are very expensive to use, or by simpler methods, such as that by Mendenhall and Perkins[2] for subsonic flow. In the latter method, vorticity is introduced into the flow at specified locations on the body. Both the location and the amount of vorticity are determined empirically. A transonic version of the theory of Reference 2 is given by Klopfer and Nixon[3] with a more complete theory given by Nixon et. al.[4] Klopfer and Nixon[3] used slender body theory to simplify the Euler equations to approximate the flow around missiles from five three-dimensional partial differential equations to two three-dimensional equations and one two-dimensional equation. The dominant feature of this formulation is that only one component of vorticity, the streamwise component, is important. In Reference 2 and in Reference 4, it is shown that the inclusion of a second vorticity component in the analysis is critical to the success of the simplified method. This second component reflects the tilting of the separated vortex in the vertical direction. In view of the importance of this second component of vorticity, the theory of Klopfer and Nixon[3] is extended in this note to include the appropriate higher order terms in order to gain further insight into the vortical flow around missiles.

One of the conclusions of the extended analysis is that vorticity in the vortex sheet is not aligned with the local streamlines, consequently producing entropy. In contrast, the rolled up vortex is aligned with the local flow since it can produce no load. At higher Mach

---

*President

numbers, if the vorticity is introduced at a non-normal angle to the body surface, this entropy effect can lead to a significant total pressure loss in the rolled-up vortex.

Analysis

The Euler equations for steady compressible flow are

$$(\rho U)_x + (\rho V)_y + (\rho W)_z = 0 \tag{1}$$

$$(\rho U^2 + p)_x + (\rho UV)_y + (\rho UW)_z = 0 \tag{2}$$

$$(\rho UV)_x + (\rho V^2 + p)_y + (\rho VW)_z = 0 \tag{3}$$

$$(\rho UW)_x + (\rho VW)_y + (\rho W^2 + p)_z = 0 \tag{4}$$

$$[(e + p)U]_x + [(e + p)V]_y + [(e + p)W]_z = 0 \tag{5}$$

and

$$p = (\gamma - 1)\{e - \rho(U^2 + V^2 + W^2)/2\} \tag{6}$$

where ρ is the density, U, V, and W are velocity components in the cartesian coordinate system (x, y, z), e is the internal energy, and p is the pressure.

Manipulation of the Euler equations and the use of Gibbs relation leads to Crocco's equation

$$\overline{q} \times \overline{\Omega} = T\overline{\nabla}S \tag{7}$$

where S is entropy, T is temperature, $\overline{q}$ is the velocity vector given by

$$\overline{q} = \overline{i}U + \overline{j}V + \overline{k}W \tag{8}$$

and

$$\overline{\nabla} = \overline{i}\frac{\partial}{\partial x} + \overline{j}\frac{\partial}{\partial y} + \overline{k}\frac{\partial}{\partial z} \tag{9}$$

The vorticity vector $\overline{\Omega}$ defined by

$$\overline{\Omega} = \overline{\nabla} \times \overline{q} \tag{10}$$

Equation (7) can be differentiated to give

$$\overline{\nabla} \times (\overline{q} \times \overline{\Omega}) = \overline{\nabla}T \times \overline{\nabla}S \tag{11}$$

or, using Equation (7)

$$\overline{\nabla} \times (\overline{q} \times \overline{\Omega}) = \overline{\nabla} T \times (\overline{q} \times \overline{\Omega})/T \tag{12}$$

In component form Equation (12) can be written as

$$\begin{aligned} U\Omega_{1x} + (V\Omega_1)_y + (W\Omega_1)_z &= \Omega_2 U_y + \Omega_3 U_z + \\ &[T_y(U\Omega_2 - V\Omega_1) - T_z(W\Omega_1 - U\Omega_3)]/T \end{aligned} \tag{13}$$

$$\begin{aligned} (U\Omega_2)_x + V\Omega_{2y} + (W\Omega_2)_z &= \Omega_1 V_x + \Omega_3 V_z + \\ &[T_x(U\Omega_2 - V\Omega_1) - T_z(V\Omega_3 - W\Omega_2)]/T \end{aligned} \tag{14}$$

$$\begin{aligned} (U\Omega_3)_x + (V\Omega_3)_y + W\Omega_{3z} &= \Omega_1 W_x + \Omega_2 W_y + \\ &[T_x(U\Omega_3 - W\Omega_1) - T_y(W\Omega_2 - V\Omega_3)]/T \end{aligned} \tag{15}$$

where $\overline{\Omega} = \overline{i}\Omega_1 + \overline{j}\Omega_2 + \overline{k}\Omega_3$

At high angles of attack the flow separates and a vortex sheet feeds two concentrated vortices as shown in Figure 1. In the previous work by Klopfer and Nixon[3] the body was considered slender with a typical cross section/length scale of ε. At very high angles of attack the flow is similar to that around an equivalent body represented by the body itself and the recirculating region bounded by the feeding sheets. Clearly, there are two scales in the problem, namely the body width/length ratio, given by ε and the characteristic height/length ratio of the recirculating region, given by δ. The length scales ε and δ are shown in Figure 1. The dominant geometrical effect of the separation is represented by the length scales ε and δ.

Now construct inner coordinates by letting

$$\overline{x} = x, \overline{y} = y/\delta, \overline{z} = z/\varepsilon \tag{16}$$

The velocity will consist of the freestream components U_o and V_o with perturbations the order of the scales; thus

$$U = U_o + \delta^p u_1 + \varepsilon^p u_2, V = V_o + \delta v, W = \varepsilon w \tag{17}$$

where if Q_o is the resultant freestream velocity and α is the angle of attack

$$U_o = Q_o \cos\alpha, V_o = Q_o \sin\alpha \tag{18}$$

The index p is such that

$$p > 1$$

For a constant energy flow

$$h + \tfrac{1}{2}(U^2 + V^2 + W^2) = \text{constant} \tag{19}$$

where h is specific enthalpy. This suggests that since

$$h = C_p T \tag{20}$$

where C_p is the specific heat at constant pressure, the temperature T may be expanded as a series like

$$T = T_o + \delta T_1 + \varepsilon^2 T_2 + \underline{O}(\delta^2) \tag{21}$$

where the form of the velocity expansions of Equation (17) has been used. It is assumed in this analysis that

$$\delta >> \varepsilon >> \delta^2 \tag{22}$$

which reflects the experimental observation[1] that the vortex tilts upwards more than it spreads outwards. It is shown later that in order to obtain the dominant effects of vortex rotation, terms of the order of δ^2 must be retained. Expansion of Equations (13-15) to this order gives.

$$\begin{gathered}\delta U_o \Omega_{1_{\bar{x}}} + [V_o + \delta v)\Omega_1]_{\bar{y}} + \delta(w\Omega_1)_{\bar{z}} + \left[\frac{\delta^2}{\varepsilon} T_{2_{\bar{z}}} V_o + \frac{\delta^3}{\varepsilon} vT_{2_{\bar{z}}}\right] \Omega_1 = \\ \delta\varepsilon^{p-1}\Omega_3 U_{\bar{z}} + \frac{\delta^2}{\varepsilon} U_o T_{2_{\bar{z}}} \Omega_2 + \delta T_{1_{\bar{z}}} U_o \Omega_3 + \delta T_{2_{\bar{y}}} U_o \Omega_3\end{gathered} \tag{23}$$

$$\delta U_o \Omega_{2_{\bar{x}}} + (V_o + \delta v)\Omega_{2_{\bar{y}}} + \delta (w\Omega_2)_{\bar{z}} - (\delta^2 T_{2x} U_o + \delta^2 w T_{2_{\bar{z}}})\Omega_2 =$$

$$\frac{\delta^2}{\varepsilon} v_{\bar{z}}\, \Omega_3 + \delta^2 \Omega_1 v_{\bar{x}} - \delta^2 V_o \Omega_1 T_{2_x} - \frac{\delta^2}{\varepsilon} T_{2_{\bar{z}}} \Omega_3 V_o - \frac{\delta^3}{\varepsilon} v T_{2_{\bar{z}}} \Omega_3 - \delta^2 v T_{1_{\bar{z}}}\, \Omega_3 \tag{24}$$

$$\delta U_o \Omega_{3_{\bar{x}}} + [(V_o + \delta v)\Omega_3]_{\bar{y}} + \delta w \Omega_{3_{\bar{y}}} - (\delta^2 T_{2x} U_o +$$

$$\delta T_{x_{\bar{y}}} V_o + \delta^2 T_{2_{\bar{y}}} v)\Omega_3 = \delta \varepsilon w_{\bar{x}}\, \Omega_1 + \varepsilon \Omega_2 w_{\bar{y}} \tag{25}$$

By examining the dominant terms in Equations (24) and (25) it can be implied that

$$\left.\begin{aligned} \Omega_2 &\sim \underline{O}\,(\delta^2 \Omega_1) \\ \Omega_3 &\sim \underline{O}\,(\delta \varepsilon \Omega_1) \end{aligned}\right\} \tag{26}$$

Retaining terms of $\underline{O}(\delta^2)$ and using Equation (26), Equations (23) - (25) can be written as

$$U_o \Omega_{1x} + (V\Omega_1)_y + (W\Omega_1)_z + T_z V \Omega_1 = 0 \tag{27}$$

$$V_o \Omega_{2y} + (T_x U_o + T_z w)\,\Omega_2 = V_x \Omega_1 \tag{28}$$

$$\Omega_3 = 0 \tag{29}$$

Note that from Equation (26)

$$|\Omega_1| >> |\Omega_2| >> |\Omega_3| \tag{30}$$

which indicates that the vortical components are separable.

The terms involving the temperature, T, are due to entropy production. If there was no entropy then these terms would vanish. In the earlier work of Klopfer and Nixon[3], entropy effects do not appear. This is because the dominant vorticity component and the dominant velocity vector are aligned. In the present case, the second order equations do not have this property. Because entropy is produced in the vortex feeding sheet there will be a total pressure loss in the vortex. If the only vorticity component at separation is Ω_1 , then entropy production there is zero only if the separation line is a crossflow stagnation point. The initial entropy production is determined by the relative angle between the separation line and the local velocity vector. In the present model it is assumed that the vortex sheet is tangential to the body surface, as sketched in Figure 1. This implies that the windward side of the separation is not a crossflow stagnation point, an assumption which is compatible with the physical description of a separating boundary layer. If the separation line is a crossflow stagnation point, then the crossflow velocity term V cannot be split into the form given in Equation (17) because V_o and δv could become comparable in magnitude but of opposite sign. In such an event, the present perturbation analysis is not valid. Because of the closer approximation of the present flow representation to the physical problem, it is suggested that entropy production should be included in the separation model and consequently the conclusions noted above are valid. The most important of these is that given in Equation (30) which indicates that the vorticity components have separable scales of magnitude. It should be noted that the temperature effects, which represent entropy, are proportional to M_∞^2 and hence become more important at higher speeds. This in turn, implies that the effect of the flow on the relative angle of flow separation may become more important at higher Mach numbers because of the entropy contribution.

Consider now the case of incompressible flow in which the entropy effects are not present; the equations approximately governing the vorticity transport can then be found from Equations (27)-(29) to be

$$U_o \Omega_{1x} + (V\Omega_1)_y + (W\Omega_1)_z = 0 \tag{31}$$

$$V_o \Omega_{2y} = V_x \Omega_1 \tag{32}$$

$$\Omega_3 = 0 \tag{33}$$

The logical choice of the index p in Equation (19) is two since from Equation (33)

$$\Omega_3 = V_x - U_y \sim 0 \tag{34}$$

or, in inner variables to a first approximation

$$\delta v_x - \delta^{p-1} u_{1\bar{y}} \sim 0 \tag{35}$$

which requires that

$$p = 2 \tag{36}$$

Consequently, Equation (35) becomes

$$v_x = U_{\bar{y}} \tag{37}$$

If Equation (32) is written in inner variables then it becomes

$$V_o \Omega_{2\bar{y}} = \delta^2 v_x \Omega_1 \tag{38}$$

From Equation (31) it may be seen that if the retained terms are of the same order of magnitude and if V_o is $\underline{O}(1)$ then, to a first approximation

$$\Omega_{1\bar{y}} = \underline{O}(\delta\Omega_1) \tag{39}$$

which implies that Ω_1 is independent of $\bar{y}$ to a first approximation. Hence, with the help of Equation (37), Equation (38) can be integrated with respect to $\bar{y}$ to give to a first approximation

$$V_o \Omega_2 = \delta^2 u_1 \Omega_1 + F(\bar{x}, \bar{z}) + \underline{O}(\delta^3) \tag{40}$$

where F(x,z) is a function of integration.

At the separation line, $y = y_{sep}$, u_1, Ω_2 and Ω_1 are specified; hence Equation (40) becomes

$$\Omega_2 - \Omega_{2sep} = \frac{\Omega_1 (U_o + \delta^2 u_1)}{V_o} - \left[\frac{\Omega_1 (U_o + \delta^2 u_1)}{V_o}\right]_{sep} + \underline{O}(\delta^3) \qquad (41)$$

where the subscript "sep" denotes a value at separation. Reverting to the usual physical coordinates, Equation (41) becomes

$$\Omega_2 = \Omega_{2sep} + \frac{\Omega_1 U}{V_o} - \left(\frac{\Omega_1 U}{V_o}\right)_{sep} \qquad (42)$$

Equation (42) is an algebraic relation between Ω_1 and Ω_2 rather than a partial differential equation and the induced velocity could be computed fairly easily. Although the velocity due to Ω_2 can be derived from Equation (42) a simpler means that uses Equation (30) is derived in Reference 4. However, the present formulation leads to more insight. It's possible that an extended analysis would produce a similarly simple relationship for Ω_3.

The extra component of vorticity, Ω_2, is derived by a stretching of Ω_1 as implied by the differential equation, Equation (14). Because of the relation given in Equation (40) the total magnitude of the vorticity, Ω is given by

$$|\Omega| = [\Omega_1^2+\Omega_2^2+\Omega_3^2]^{1/2} \sim |\Omega_1| + \underline{O}(\delta^2)\,|\Omega_1| \qquad (43)$$

However, the vortex is inclined at an angle θ_v given by

$$\theta = \arctan\left(\frac{\Omega_2}{\Omega_1}\right) \quad . \qquad (44)$$

which, from Equation (42), is given by

$$\theta_v = \arctan \left[\frac{U}{V_o} - \left(\frac{U\Omega_1}{V_o} \right)_{sep} \Big/ \Omega_1 + \Omega_{2sep}/\Omega_1 \right] + \underline{O}(\delta^3) \tag{45}$$

Since the local flow vector, θ_f, is given by

$$\theta_f = \arctan (V/U) \tag{46}$$

it may be seen that in general the vorticity in the vortex sheet is not aligned with the flow vector. Although the above analysis is for incompressible flow, this result is consistent with the argument regarding entropy production given earlier.

At the end of the vortex sheet the rolled up vortex cannot support a load and therefore must be aligned with the flow vector, that is

$$\theta_V = \theta_f \tag{47}$$

and hence to $\underline{O}(\delta)$

$$\left(\frac{V}{U} \right)_C = \left[\frac{U}{V_o} - \left(\frac{U\Omega_1}{V_o} \right)_{sep} /\Omega_2 + \frac{\Omega_2}{\Omega_1} \, sep \right]_C + \underline{O}(\delta^3) \tag{48}$$

where the subscript "C" denotes a value at the rolled up vortex. If the angle of the rolled up vortex is denoted by θ_c then it follows from Equation (48) that

$$\tan\theta_c = \frac{V_c}{V_o} (\tan\Theta_C)^{-1} R \tag{49}$$

where

$$R = \frac{-\Omega_{2sep}}{\Omega_{1c}} + \left(\frac{U\Omega_1}{V_o} \right)_{sep} \Big/ \Omega_{1c} \tag{50}$$

From Equation (30) Ω_{2sep} is much less than Ω_1, and since U and V_o are of the same order of magnitude, R is positive.

Equation (49) can be solved to give

$$\tan\theta_c = \tfrac{1}{2}\{-R \pm [R^2 + 4V_c/V_o]^{1/2}\} \qquad (51)$$

which gives a relation for the angle of the rolled up vortex. Since θ_c mus. zero if no vorticity is shed, as is the case when $\alpha = 0$, it follows that the positive sign in Equation (51) must be taken. Thus

$$\tan\theta_c = \tfrac{1}{2}\{-R + [R^2 + 4V_c/V_o]^{1/2}\} \qquad (52)$$

For a long body the strength of the rolled up vortex will increase as more body shed vorticity reaches it. From experimental[2] evidence the angle of the rolled up vortex becomes constant and hence

$$\tan\theta_c = \frac{V_c}{U_c} = \frac{V_c}{V_o}\frac{V_o}{U_c} = \frac{V_c}{V_o}\tan\alpha + \underline{O}(\delta^2) - \text{constant} \qquad (53)$$

since $U_c = U_o + \underline{O}(\delta^2)$ from Equations (17) and (36). Thus V_c/V_o is approximately constant and hence, from Equation (52) R must be constant. If the shedding rate is constant, that is $(\Omega_2 V_o)_{sep}$ and $(U\Omega_1)_{sep}$ are constant, it follows that Ω_{1c} is constant. Because the vorticity in the rolled up vortex accumulates along the vortex because of the steady shedding rate, it then follows that the vortex must expand in size as the distance downstream increases in order to keep Ω_{ic} constant. This is in accordance with experimental data.

Concluding Remarks

An analysis for vortical flows that includes two components of vorticity has been derived. The analysis indicates that vorticity in the vortex sheet does not align with stream lines if it is introduced at a non-normal angle to the body. Because of this fact, entropy is produced which will cause a loss of total pressure in the rolled up vortex. The analysis also indicates that the rolled up vortex will widen as it progresses down the body, provided the shed vorticity is constant, a fact known from other sources, but a corroborating factor in the present theory. A critical result is that the three vorticity components are separable in magnitude for a slender body leading to a less restrictive theory than in Reference 3. Thus it is possible that for the flow around slender missiles at very high angles of attack a much simpler set of equations than the Euler equations may model the flow. This simpler set of equations would consist of two three-dimensional partial differential equations, one two-dimensional partial differential equation and two algebraic equations.

References

1. Klopfer, G. H. and Nielsen, J. N.: Computational Fluid Dynamics Applications to Missile Aerodynamics, Paper No. 3 in AGARD CP-336, Missile Aerodynamics, September 1982.
2. Mendenhall, M. R. and Perkins, S. C., Jr.: Cloud Model for Body Vortex Shedding and Tracking. In Tactical Missile Aerodynamics, (edited by M. J. Hemsch and J. N. Nielsen), Vol. 104, Progress in Astronautics and Aeronautics, AIAA 1986.
3. Klopfer, G. H. and Nixon, D.: Transonic Flows with Vorticity Transport Around Slender Bodies, AIAA Journal, Vol. 27, No. 10, 1989, pp. 1461-1464.
4. Nixon, D., Caruso, S. C., and Klopfer, G. H.: Prediction of Transonic Flow with Vortex Effects. AIAA Paper 90-0389, 1990.
5. Batina, J. T.: An Efficient Algorithm for solution of the Unsteady Transonic Small Disturbance Equation, AIAA Paper 87-0109, 1987.
6. Nixon, D.: The Effect of Vortex Rotation on the Flow Around a Missile. NEAR Paper No. 266, Nielsen Engineering & Research, January 1990.

7. Stratford, B. S.: The Prediction of Separation of the Turbulent Boundary Layer. Journal of Fluid Mechanics, Vol. 4, 1959, pp. 1-16.

8. Spangler, S. B. and Mendenhall, M. R.: Further Studies of Aerodynamic Loads at Spin Entry, Report ONR-CR-212-225-3, 1977.

Acknowledgement

The work described in this manuscript was sponsored by the Army Research Office under contract DAAL03-87-C-0008.

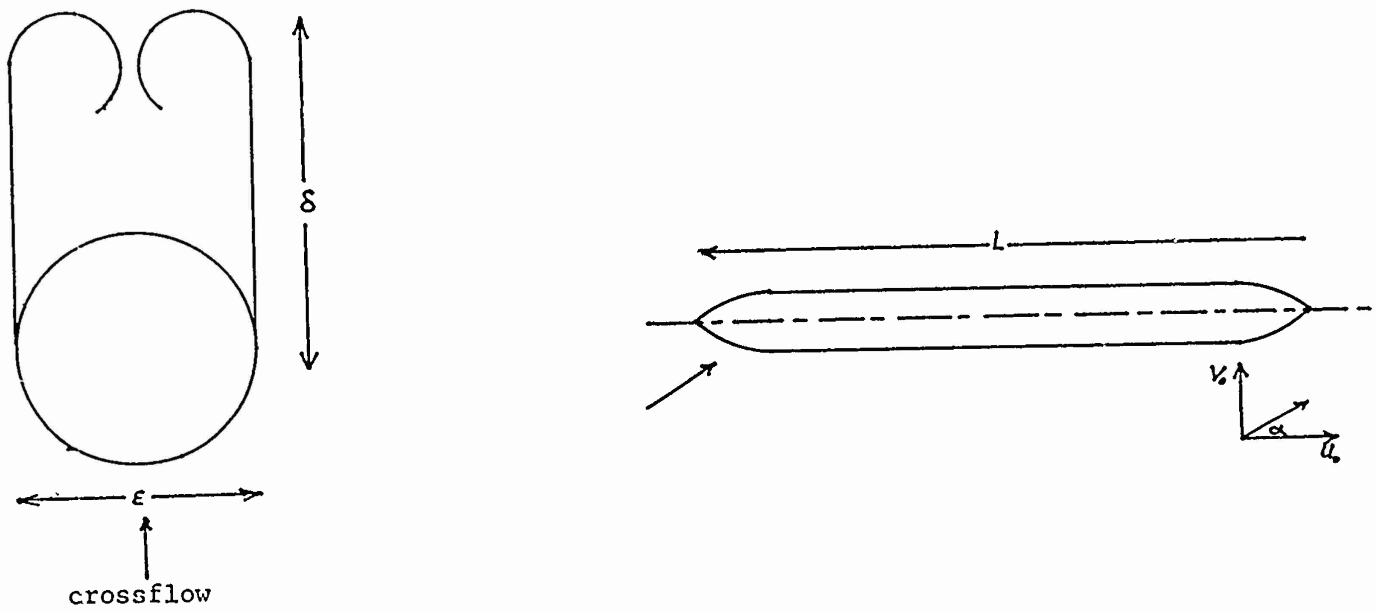

Figure 1. - Relative Scales of Equivalent Body.

AIAA

AIAA 90-0934

Prediction of Unsteady Transonic Flow Around Missile Configurations

D. Nixon, P.H. Reisenthel,
T.O. Torres,
Nielsen Engineering & Research
Mountain View, CA
and
G. H. Klopfer,
NASA-Ames
Moffett Field, CA

31ST AIAA/ASME/ASCE/AHS/ASC Structures, Structural Dynamics and Materials Conference

Long Beach, CA / April 2-4, 1990

For permission to copy or republish, contact the American Institute of Aeronautics and Astronautics
370 L'Enfant Promenade, S.W., Washington, D.C. 20024

PREDICTION OF UNSTEADY TRANSONIC FLOW AROUND MISSILE CONFIGURATIONS

D. Nixon,* P. H. Reisenthel,** T. O. Torres†
Nielsen Engineering & Research, Inc.
Mountain View, CA

and

G. H. Klopfer‡
NASA Ames Research Center
Moffett Field, CA

1. Introduction

In recent years it has been possible to predict the unsteady transonic flow around a wing, especially those typical of commercial aircraft, in a fairly efficient manner. Frequently, the computer codes that are used are based on potential theory and are considerably faster than a corresponding calculation using the Euler equations. These methods have been developed for aircraft and are not really applicable to missile flows where the effects of vorticity due to flow separation are important; the potential approximation cannot predict the effects of vorticity other than by representing a vortex wake by an infinitely thin sheet which is excluded from the computational domain. This model is complicated and may not be a viable option for routine calculations around real aircraft or missile configurations because the geometry of the vortex sheet can get quite complex.

Missiles generally have low aspect ratio fins and slender bodies, neither of which are features of commercial aircraft, and the airflow is dominated by vortex effects; this is in contrast to the flow over a commercial aircraft which is attached. For steady missile flow a variety of prediction methods are available, ranging from panel methods with the addition of nonlinear vortex dynamics to the Euler equations or Navier-Stokes equations. The Navier Stokes equations will model flow separation and track the resulting vorticity but are only as accurate as the turbulence model used in the calculation. This is critical in defining the separation line. The prediction methods based on the Euler equations need some empirical criteria to predict the location and strength of the separating vortex sheet; the Euler equations will then model the transport of this vorticity reasonably accurately.

A detailed discussion of the methods used to predict steady flows over missiles is given in Reference 1. In order to predict unsteady flow over a missile to adequate accuracy, the method must be able, therefore, to treat unsteady separated flow. Furthermore, if it is necessary to predict the steady flow at transonic, rather than supersonic, speeds the method must be computationally efficient since unlike supersonic flow problems which can use a marching procedure, transonic flow methods require numerous sweeps of the computational domain, leading to large computational times.

It would be ideal to use the Navier-Stokes equations to model unsteady transonic flow around missiles, but there are several difficulties with this approach. The most obvious difficulty is the computer time required, which is several orders of magnitude greater than that required for a potential calculation. Even if a dedicated supercomputer is available for such calculations, the computation of the necessary flow separation may be inaccurate because of the inherent inaccuracy in many present turbulence models. The next best approach is to use the time dependent Euler equations which require some empirical factor to initiate separation and compute the shed vorticity. This empiricism would be a development of the steady flow criteria described in Reference 1. If the separation line and shed vorticity can be predicted, then the Euler equations would be a viable model. However, since missiles are slender some further approximations can be made. This paper is concerned with developing a method of predicting the unsteady pressure distribution on missiles at transonic and supersonic speeds. The concepts developed in this work are extensions of an earlier analysis[2] for steady flow. The approach is to make as much use of the existing technology as possible. The final goal is to develop a computer code capable of predicting the unsteady transonic flow about missiles for use in aeroelastic calculations or during maneuver. The present paper is an account of the second phase of the work, namely the preliminary development of an unsteady flow variant of the method.

The approach is based on experience gained in steady subsonic and supersonic flow predictions for missiles, in particular, the fact that if a separation line and the strength of the vorticity introduced at that line can be estimated empirically, the governing equations (such as the Euler equations) will represent the transport

---

*President
**Research Scientist, Member AIAA
†Research Engineer, Member AIAA
‡Research Scientist, Member AIAA

of this vorticity accurately. Because the computational time for the Euler equations for an unsteady calculation is considerably greater than that for a potential calculation, a simplified model is used.

The basic equations are an extension of those derived by Klopfer and Nixon[3] for steady flow and are a subset of the Euler equations. For slender bodies, the five Euler equations are reduced to an equation similar to the three-dimensional unsteady potential equation, a three-dimensional vorticity transport equation, and a two-dimensional Poisson equation. Apart from the reduced set of equations, a second advantage is that one of the equations is almost identical to the potential equation for which there are well tested computer codes. This allows the development of a prediction method based considerably on proved technology. A derivation of the equations is given in the Appendix.

2. Basic Equations

From the Appendix, the basic equations are as follows:

Vorticity Transport

$$\Omega_t + \Omega_x + (v\Omega)_y + (w\Omega)_z = 0 \qquad (1)$$

Rotational Crossflow

$$A_{yy} + A_{zz} = -\Omega \qquad (2)$$

Mass Conservation

$$\rho_t + (\rho u)_x + (\rho v)_y + (\rho w)_z = 0 \qquad (3)$$

where

$$u = 1 + \phi_x;\ v = \phi_y + A_z;\ w = \phi_z - A_y \qquad (4)$$

and

$$\rho = \rho_\infty \left\{ 1 + \frac{(\gamma-1) M_\infty^2}{2} (1 - 2\phi_t - u^2 - v^2 - w^2) \right\}^{\frac{1}{\gamma-1}} \qquad (5)$$

ϕ is the velocity potential, A is the vector potential, ρ is the density, M_∞ is the freestream Mach number, Ω is the vorticity in the streamwise direction, and u, v, and w are velocities in the coordinate directions x, y, z respectively.

Using Equations (3), (4), and (5) and making the usual transonic small disturbance (TSD) approximation leads to the following modified, TSD equation.

$$\frac{\partial f_o}{\partial t} + \frac{\partial f_1}{\partial x} + \frac{\partial f_2}{\partial y} + \frac{\partial f_3}{\partial z} = 0 \qquad (6)$$

where

$$\left.\begin{aligned} f_o &= -M_\infty^2 \phi_t - 2M_\infty^2 \phi_x \\ f_1 &= (1-M_\infty^2)\phi_x - \frac{1}{2}(\gamma+1) M_\infty^2 \phi_x^2 \\ &\quad + \frac{1}{2}(\gamma-3) M_\infty^2 (\phi_y + A_z)^2 \\ f_2 &= \phi_y + A_z - (\gamma-1) M_\infty^2 \phi_x (\phi_y + A_z) \\ f_3 &= \phi_z - A_y \end{aligned}\right\} \qquad (7)$$

The boundary conditions on the body are zero flow through the body. There is zero flux of vorticity through the body except at the specified separation line.

3. Computer Code and Numerical Methods

Equation (6) is identical in form to that solved by Batina et al[4] in the CAP-TSD code. This code is capable of predicting the unsteady transonic and supersonic flow over an aircraft with stores. Consequently, CAP-TSD is used as a basis for the present method. In thi. initial phase, only a body or fuselage is considered; in the near future, fins will be added to the model.

The algorithm used in CAP-TSD is approximate factorization with time stepping as an option; this algorithm is retained in solving Equation (7). A modified version of this algorithm is used to solve the vector potential equation, Equation (2). The vorticity transport equation is solved by using another modified variant of the approximate factorization algorithm.

3.1 Continuity Equation:

Because CAP-TSD uses a shearing transformation described by: $\xi = \xi(x, y)$; $\eta = y$; $\zeta = z$; $\tau = t$, Equation (6) is reformulated as:

$$\frac{\partial}{\partial \tau} \bar{f}_o + \frac{\partial}{\partial \xi} \bar{f}_1 + \frac{\partial}{\partial \eta} \bar{f}_2 + \frac{\partial}{\partial \zeta} \bar{f}_3 = 0 \qquad (8)$$

where:

$$
\left.
\begin{aligned}
\bar{f}_o &= \frac{-M_\infty^{\ 2}}{\xi_x}\,\phi_\tau - 2M_\infty^{\ 2}\phi_\xi \\
\bar{f}_1 &= \left[\frac{(1 - M_\infty^{\ 2})\,\xi_x^{\ 2} + \xi_y^{\ 2}}{\xi_x} - 2M_\infty^{\ 2}\xi_y A_\zeta\right]\phi_\xi \\
&\quad - \frac{1}{2}(\gamma + 1)M_\infty^{\ 2}\left[\xi_x^{\ 2} + \xi_y^{\ 2}\right]\phi_\xi^{\ 2} \\
&\quad - 2M_\infty^{\ 2}\xi_y\phi_\xi\phi_\eta + \frac{1}{2}(\gamma - 3)M_\infty^{\ 2}\phi_\eta^{\ 2} \\
&\quad + \left[(\gamma - 3)M_\infty^{\ 2}A_\zeta + \frac{\xi_y}{\xi_x}\right]\phi_\eta \\
&\quad + \frac{1}{2}(\gamma - 3)M_\infty^{\ 2}A_\zeta^{\ 2} \\
\bar{f}_2 &= \left[\frac{\xi_y}{\xi_x} - (\gamma - 1)M_\infty^{\ 2}A_\zeta\right]\phi_\xi \\
&\quad - (\gamma - 1)M_\infty^{\ 2}\phi_\xi\phi_\eta + \frac{\phi_\eta}{\xi_x} \\
&\quad - (\gamma - 1)M_\infty^{\ 2}\xi_y\phi_\xi^{\ 2} \\
\bar{f}_3 &= \frac{\phi_\zeta}{\xi_x}
\end{aligned}
\right\} \quad (9)
$$

The time-marching procedure is performed using a second order accurate implicit scheme, thus

$$
\left.
\begin{aligned}
&- \frac{M_\infty^{\ 2}}{\xi_x}\left[\frac{2\phi^{n+1} - 5\phi^n + 4\phi^{n-1} - \phi^{n-2}}{\Delta t^2}\right] \\
&- 2M_\infty^{\ 2}\,\frac{\left[3\phi_\xi^{n+1} - 4\phi^n{}_\xi + \phi^{n-1}_\xi\right]}{2\Delta t} + \left[\bar{f}_1\right]_\xi^{n+1} \\
&+ \left[\bar{f}_2\right]_\eta^{n+1} + \left[\bar{f}_3\right]_\zeta^{n+1} = R'(\phi^{n+1})
\end{aligned}
\right\} \quad (10)
$$

Linearizing about $\phi^{n+1} = \phi^* + \Delta\phi$ and recasting the problem in approximate factorization form yields:

$$
\left.
\begin{aligned}
&\left[I + \left[\frac{3}{2}\,\xi_x\Delta t\right]\partial_\xi - \left[\frac{(\Delta t)^2\xi_x}{2M_\infty^{\ 2}}\right]\partial_\xi\left[\bar{F}_1\partial_\xi\right]\right] \\
&\times \left[I - \left[\frac{(\Delta t)^2\xi_x}{2M_\infty^{\ 2}}\right]\partial\eta\left[\bar{F}_2\partial\eta\right]\right] \\
&\times \left[I - \left[\frac{(\Delta t)^2\xi_x}{2M_\infty^{\ 2}}\right]\partial_\zeta\left[\bar{F}_3\partial_\zeta\right]\right]\Delta\phi = -R(\phi^*)
\end{aligned}
\right\} \quad (11)
$$

with

$$
\left.
\begin{aligned}
\bar{F}_1 &= \left[1 - M_\infty^2\right]\xi_x + \frac{\xi_y^2}{\xi_x} - 2M_\infty^2\xi_y A_\zeta \\
&\quad - (\gamma + 1)\left[\xi_x^2 + \xi_y^2\right]\phi_\xi^* - 2M_\infty^2\xi_y\phi_\eta^{\ *} \\
\bar{F}_2 &= -(\gamma - 1)M_\infty^{\ 2}\phi_\xi^{\ *} + \frac{1}{\xi_x} \\
\bar{F}_3 &= \frac{1}{\xi_x}
\end{aligned}
\right\} \quad (12)
$$

and

$$
\left.
\begin{aligned}
R(\phi^*) &= \frac{-\Delta t^2\xi_x}{2M_\infty^{\ 2}} \\
&\quad \times \left[-\frac{M_\infty^2}{\xi_x}\left[\frac{2\phi^* - 5\phi^n + 4\phi^{n-1} - \phi^{n-2}}{(\Delta t)^2}\right]\right. \\
&\quad - M_\infty^2\left[\frac{3\phi_\xi^{\ *} - 4\phi_\xi^{\ n} + \phi_\xi^{\ n-1}}{\Delta t}\right] \\
&\quad \left. + \partial_\xi\bar{f}_1^* + \partial_\eta\bar{f}_2^* + \partial_\zeta\bar{f}_3^*\right]
\end{aligned}
\right\} \quad (13)
$$

3.2 Vector Potential Equation:

Equation (2) does not have explicit time-dependence. It is solved at each time step and in each individual streamwise plane by using successive over-relaxation. For the continuity and vorticity transport equations, if the Newton iteration option is used, then $\Delta\phi$ and $\Delta\Omega$ approach zero at each time step, and the solution is time-[illegible]te. For the vector potential equation, the solution is also time-accurate, since at each iteration, ΔA can be made arbitrarily close to zero.

3.3 Vorticity Transport Equation:

The time-dependent vorticity transport Equation (1) can be rewritten as

$$\left.\begin{aligned} &\left(\frac{\Omega}{\xi_x}\right)_\tau + \left(\left[U + \frac{\xi_y}{\xi_x} V\right]\Omega\right)_\xi \\ &+ \left(\frac{V\Omega}{\xi_x}\right)_\eta + \left(\frac{W\Omega}{\xi_x}\right)_\zeta = \Omega u_\xi \end{aligned}\right\} \quad (14)$$

The corresponding finite difference equation is formulated similarly to Equation (10) and yields:

$$\left.\begin{aligned} &\left(\Omega^{n+1} - \frac{4}{3}\Omega^n + \frac{1}{3}\Omega^{n-1}\right) \\ &+ \frac{2\Delta t}{3}\,\xi_x\left\{\left(\left[U + \frac{\xi_y}{\xi_x} V\right]\Omega\right)_\xi^{n+1}\right. \\ &\left. + \left(\frac{V\Omega}{\xi_x}\right)_\eta^{n+1} + \left(\frac{W\Omega}{\xi_x}\right)_\zeta^{n+1} - (\Omega U_\xi)^{n+1}\right\} = 0 \end{aligned}\right\} \quad (15)$$

Using Newton's method ($\Omega^{n+1} = \Omega^* + \Delta\Omega$), and expressing the problem in approximate factorization form leads to the equation:

$$\begin{aligned} &[I + \beta\partial_\xi\tilde{F}_1]\,[I + \beta\partial_\eta\tilde{F}_2]\,[I + \beta\partial_\zeta\tilde{F}_3]\Delta\Omega \\ &= -\beta R(\Omega^*) \end{aligned} \quad (16)$$

where:

$$\beta = \frac{1}{\dfrac{3}{2\Delta t\xi_x} - U_\xi^*} \quad (17)$$

$$\left.\begin{aligned} \tilde{F}_1 &= 1 + \frac{\xi_x^2 + \xi_y^2}{\xi_x}\phi_\xi^* \\ &\quad + \frac{\xi_y}{\xi_x}\phi_\eta^* + \frac{\xi_y}{\xi_x}A_\zeta^* \\ \tilde{F}_2 &= \frac{1}{\xi_x}\left[\xi_y\phi_\xi^* + \phi_\eta^* + A_\zeta^*\right] \\ \tilde{F}_3 &= \frac{1}{\xi_x}\left[\phi_\zeta^* - \xi_y A_\xi^* - A_\eta^*\right] \end{aligned}\right\} \quad (18)$$

and

$$\begin{aligned} R(\Omega^*) = &\left(\frac{3\Omega^* - 4\Omega^n + \Omega^{n-1}}{2\xi_x\Delta t}\right) + \left(\tilde{F}_1\Omega^*\right)_\xi \\ &+ \left(\tilde{F}_2\Omega^*\right)_\eta + \left(\tilde{F}_3\Omega^*\right)_\zeta - \xi_x\phi_{\xi\xi}^*\Omega^* \end{aligned} \quad (19)$$

4. Boundary Conditions

The solution to Equations (1), (2), and (3) requires that properly formulated boundary conditions be specified for ϕ, A, and Ω. For the farfield, these boundary conditions are based on the fact that the disturbance velocities must vanish away from the solid boundary. At the body, the flow is tangential to the surface, and a normal vorticity jet is introduced in the inviscid flowfield at the point of flow separation.

With CAP-TSD's cartesian grid, the farfield boundary conditions can be formulated as:

$$\begin{aligned} \vec{\nabla}\phi &= \vec{0} \\ A &= A_\infty \\ \Omega &= 0 \end{aligned} \quad (20)$$

About the symmetry plane, V and Ω are antisymmetric in y; therefore at y = 0:

$$\begin{aligned} \phi_y + A_z &= 0 \\ \Omega &= 0 \end{aligned} \quad (21)$$

The main problem with the boundary conditions is the representation of the fuselage. In CAP-TSD the fuselage cross-section is assumed to be elliptic, and the zero flux boundary condition on the body surface is transferred to a bounding cartesian grid (the "computational fuselage") by using ideas from slender body theory. For angles of attack typical of missile flight, however, the existing treatment of the fuselage is inadequate and an alternative scheme was developed.

In this modified scheme, the assumption of slender body flow is still used, in particular, the consequence that only the crossflow is important. The boundary conditions on the cartesian computational boundary are found from the "change in thickness" effect, which is relatively accurate, and by using the analytic solution for the crossflow around an ellipse to give the value of the normal velocity on the computational boundary. The magnitude of the crossflow is $U_\infty \sin\alpha$, where U_∞ is the freestream velocity and α is the instantaneous angle of attack.

The fact that, in the absence of vorticity, the "standard" form of the TSD Equation (i.e., when the product $\phi_x\phi_y$ is negligible in Equation (7) (no swept shocks)) reduces to Laplace's equation in the crossflow plane suggests the use of an analytic solution. For an elliptical body with semi-axes a and b in the y and z directions respectively, this analytical solution is obtained by using conformal mapping of an ellipse onto a flat plate. Such a transformation is given by:

$$\sigma = \frac{Z + (Z^2 - a^2 + b^2)^{1/2}}{a + b} + \frac{a + b}{Z + (Z^2 - a^2 + b^2)^{1/2}} = \chi(Z) \qquad (22)$$

with: $Z = -z + iy$.

In σ-space, the elliptical boundary and the symmetry plane ($y = 0$) are mapped into the real axis. This mapping is used to transfer boundary conditions from the true body surface to the computational fuselage. At each streamwise cross-section, the model which is used to represent the flow between these two surfaces is that associated with a point vortex in a crossflow. In σ-space, the irrotational crossflow is represented by a uniform stream of complex velocity:

$$\frac{dF_P}{d\sigma} = -\sin(\alpha)\,\frac{(a + b)}{2} \qquad (23)$$

In addition, a point vortex is used to model the rotational component of the flowfield. Its strength Γ is calculated numerically by integrating the vorticity in the computational domain, and its location in Z-space is determined as the vorticity centroid (Z_0). The corresponding induced velocity at point σ is then given by:

$$\frac{dF_R}{d\sigma} = \frac{i\Gamma}{2\pi}\left(\frac{1}{\sigma - \bar{\sigma}_0} - \frac{1}{\sigma - \sigma_0}\right) \qquad (24)$$

where $\sigma_0 = \chi(Z_0)$, and σ_0 represents its complex conjugate.

In Equations (23) and (24), F_P and F_R designate the complex potentials representing the effects of potential and rotational components of the flow respectively.

For any point Z along the top or bottom of the computational fuselage, the normal velocity is then prescribed according to:

$$W_P = \mathrm{Re}\left\{-\frac{dF_P}{d\sigma}\frac{d\chi}{dZ}\right\} = \phi_z + \sin(\alpha) \qquad (25)$$

and

$$W_R = \mathrm{Re}\left\{-\frac{dF_R}{d\sigma}\frac{d\chi}{dZ}\right\} = -A_y \qquad (26)$$

Along the vertical sides of the cartesian computational box, the spanwise component of velocity is similarly given by:

$$V_P = \mathrm{Im}\left\{-\frac{dF_P}{d\sigma}\frac{d\chi}{dZ}\right\} = \phi_y \qquad (27)$$

and

$$V_R = \mathrm{Im}\left\{-\frac{dF_R}{d\sigma}\frac{d\chi}{dZ}\right\} = A_z \qquad (28)$$

Equations (25) and (27) are used directly to supply CAP-TSD with the required Neumann boundary conditions on ϕ. On the other hand, Equations (26) and (27) specify the tangential derivative of A along the computational boundary. Therefore, A must first be integrated along the boundary to provide the proper Dirichlet condition for Equation (2).

The addition of $\sin(\alpha)$ to ϕ_z in (25) simply reflects the fact that in CAP-TSD the grid is aligned with the freestream. Consequently, the slender body is in effect considered to be inclined at an angle ($-\alpha$) within the computational fuselage, and W represents the downwash effect, as seen from a referential aligned with $\vec{U}_\infty$. This configuration, however, leads to considerable inaccuracies in resolving the vortex close to the body. More importantly, in the physical case where vorticity is introduced at the top or upper right-hand side of the cartesian boundary, Ω can only be transported outside the computational flowfield, towards the body, and cannot be resolved explicitly.

This problem is circumvented by placing the body parallel to the grid and considering the freestream flow to be inclined at an angle of attack α. As a first approximation, the disturbance potential ϕ can be solved using Equation (11), as long as α remains small, although one of the goals of the present study is to push the theory well beyond its limits, i.e., for finite α. In the vorticity transport equation, Equation (20), ϕ is therefore replaced by ($\phi + \sin(\alpha)\, z$) in order to effectively allow the transport of vorticity away from the computational fuselage.

The transfer of boundary conditions from the body surface to the cartesian computational boundary using potential flow around an ellipse can be justified on the basis of the following arguments. First, the use of an incompressible boundary condition is warranted because the crossflow Mach number $M_c = M_\infty \sin\alpha$ is order α, and, therefore, compressibility effects in the crossflow plane are of order α^2 and can be neglected, since the angle of attack can be initially assumed to be itself of order ε (Ref. 6). Second, the strictly two-dimensional analysis must be valid for L >> D, i.e., to the order of slender body theory. Finally, if τ is a characteristic time scale for the transfer of boundary conditions from the true body surface to the computational fuselage (length scale D), then an upper bound for τ is given by $\tau = D/(C(1-M_c))$. In an unsteady flow of reduced frequency $k = \omega L/U_\infty$ the characteristic unsteady time scale is: $T = 2\pi L/(U_\infty k)$, and the ratio of these time scales is given by:

$$\frac{\tau}{T} \le \left[\frac{D}{L}\right]\left[\frac{M_\infty}{1 - M_c}\right]\frac{k}{2\pi} = O(\varepsilon k) \qquad (29)$$

thus justifying the use of an effectively quasi-steady boundary condition, valid for reduced frequencies up to order unity.

A flow separation condition is simulated by the injection of vorticity into the inviscid flowfield at the point of separation. For steady flow, a modified version of the Stratford criterion[7] is used to determine the separation line:

$$C_p'\left[s\frac{dC_p'}{ds}\right]^{1/2}\left[Re_s \times 10^{-6}\right]^{0.1} = 0.35\ \sin\alpha \qquad (30)$$

where C_p' is the modified pressure coefficient, and s is the virtual length of the turbulent boundary layer, as seen in the crossflow plane[8].

The strength of the vorticity jet is derived from the observation that for a flat plate boundary layer of thickness δ, the streamwise vorticity flux per unit span is given by:

$$\int_0^\delta U\Omega dy = \frac{U_e^{\,2}}{2} \qquad (31)$$

where U_e is the velocity at the edge of the boundary layer. At the point of separation, it is assumed that a net fraction λ of this vorticity flux is injected into the freestream. This method has been formally shown[2] to be equivalent at subsonic speeds to the "vortex cloud" method used by Mendenhall and Perkins[4]. In its numerical implementation, the incremental normal vorticity flux released between x and x + Δx is derived from:

$$\int_x^{x+\Delta x}\int_{s_1}^{s_2} V_n\Omega ds = \frac{1}{2}W_{sp}^{\;2}\lambda\Delta x \qquad (32)$$

where the subscript "sp" denotes a value at separation, and s_1 and s_2 are values of the curvilinear coordinate along the body in the crossflow plane, placed on either side of the separation point. The empirical "vortex reduction factor" λ determines the amount of vorticity shed at that point and is set to be equal to 0.6.

The transfer of the vorticity jet boundary condition to the computational box requires further analysis. For consistency with the model used to transfer velocity boundary conditions, the Stratford criterion can be implemented by using a transformation which inverts Equation (22), to obtain C_p at the body surface (see Sec. 6). Knowing the resulting separation point, Z^*, one can obtain the value of the stream function $\psi^* = \mathrm{Im}\{F(\sigma^*)\}$, at $\sigma^* = \chi(Z^*)$. The location of the vorticity jet at the computational boundary could then be determined as that which satisfies $\psi = \psi^*$. At the present time, the computer code is set up to prescribe any distribution of normal vorticity fluxes along the computational fuselage boundary. The results presented in this paper, however, consider only the model case of a concentrated vorticity flux placed at the top surface and designed to approximate the above scenario.

5. Second Order Correction

Nixon et al[2] have shown that a second order extension of the theory is required in order to account for the vortex tilting phenomenon. The tilting away from the axial direction is obtained by retaining the rotational component of streamwise velocity, U_R. This is achieved by integrating the spanwise vorticity in the normal direction, which yields to leading order:

$$U_R = \int^z \frac{\partial}{\partial x}\left[W_R\right]dz \qquad (33)$$

The inclusion of this higher order term was shown to give more accurate results and laid a theoretical foundation for the "empirical correction" used by Mendenhall and Perkins[4].

6. Pressure Coefficient Calculation

The pressure coefficient at the surface of the body is calculated using the isentropic relation

$$C_p = \frac{2}{\gamma M_\infty^2}\left\{\left[1 - \frac{(\gamma - 1)}{2} M_\infty^2 \left[2\frac{\partial\phi}{\partial t} + q^2 - q_\infty^2\right]\right]^{\frac{\gamma}{(\gamma-1)}} - 1\right\} \tag{34}$$

where q^2 is the squared modulus of the total velocity $\vec{V}_P + \vec{V}_R$, including the second order correction U_R.

Since q^2 and $\partial\phi/\partial t$ are not readily available at the body surface, owing to the use of the cartesian computational boundary, it is necessary to use an inverse transformation relating $\partial\phi/\partial t$ and q^2 at the computational fuselage to $\partial\phi/\partial t|_s$ and q_s^2 at the body surface.

This can be achieved by using the inverse conformal mapping transformation:

$$Z = \frac{(a + b)}{4}\left(\sigma + (\sigma^2 - 4)^{1/2}\right) + \frac{a - b}{\sigma + (\sigma^2 - 4)^{1/2}} = \chi^{-1}(\sigma) \tag{35}$$

For any first grid point away from the computational boundary, Z is projected orthogonally onto a point Z_s which belongs to the true body surface. From Equations (23) and (24), the crossflow surface velocity at Z_s can then be related to the velocity calculated at Z by observing that in σ-space:

$$\left.\frac{dF}{d\sigma}\right|_{\sigma_s} = \left.\frac{dF}{d\sigma}\right|_{\sigma} + \kappa(\sigma,\sigma_s,\sigma_o,\Gamma) \tag{36}$$

where κ is a complex transfer function given by:

$$\kappa = \frac{i\Gamma}{2\pi}\left\{\frac{1}{\sigma_s-\bar{\sigma}_o} + \frac{1}{\sigma-\sigma_o} - \frac{1}{\sigma_s-\sigma_o} - \frac{1}{\sigma-\bar{\sigma}_o}\right\} \tag{37}$$

Instead of $dF/d\sigma|_\sigma$, the actual velocity calculated at Z is mapped in σ-space, so that:

$$\left.\frac{dF}{d\sigma}\right|_{\sigma_s} = \left.(-w-iv)\frac{d\chi}{d\sigma}^{-1}\right|_{\sigma} + \kappa(\sigma,\sigma_s,\sigma_o,\Gamma) \tag{38}$$

Finally, the complex velocity at the surface can be evaluated in Z-space, using the original transformation expressed in Equation (22):

$$-w_s-iv_s = \left\{\left.(-w-iv)\frac{d\chi}{d\sigma}^{-1}\right|_{\sigma} + \kappa(\sigma,\sigma_s,\sigma_o,\Gamma)\right\}\left.\frac{d\chi}{dZ}\right|_{Z_s} \tag{39}$$

The squared modulus is then calculated by assuming that the dominant (streamwise) component of velocity is equal to that calculated at Z, hence:

$$q_s^2 = (1+\phi_x+U_R)^2 + v_s^2 + w_s^2 \tag{40}$$

Similarly, the complex potentials at σ_s and σ can easily be related using the following relation:

$$\phi_s = \phi + \mathrm{Re}\left\{\frac{i\Gamma}{2\pi}\ln\left[\frac{(\sigma_s-\bar{\sigma}_o)(\sigma-\sigma_o)}{(\sigma_s-\sigma_o)(\sigma-\bar{\sigma}_o)}\right] - \sin(\alpha)\frac{a+b}{2}(\sigma_s-\sigma)\right\} \tag{41}$$

Hence $\partial\phi/\partial t|_s$ is not equal to $\partial\phi/\partial t$, and must be modified in order to account, in particular, for the temporal variations of Γ and σ_o, which can be the source of additional phase lags.

7. Results

A time-accurate calculation was performed for a missile-shaped body of 11:1 aspect ratio and 2:1 elliptical cross-section. A planform section of the body in the symmetry plane is shown in Figure 1. The body was configured at a mean angle of attack $\alpha = 15°$, and the freestream Mach number was set to $M_\infty = 0.3$.

The mesh size was 45 x 25 x 54, and its full extent in the crossflow plane is represented in Figure 2. The location of the computational fuselage is indicated by the inner boundary of the grid, within which the elliptical cross-section of the body has been outlined. A vorticity flux was introduced along the central portion of the body ($0.26 \le X/D \le 0.78$) in the form of a vertical vorticity jet (the arrow in Figure 3). Figure 3 also indicates the convention used for the definition of the roll angle θ. To avoid any possible confusion, a note should be made that throughout the remainder of this manuscript, the symbol D is used as a reference length scale and refers to the half-axis of the elliptical cross-section in the spanwise direction. Similarly, X, Y, and Z are used to refer to the streamwise, spanwise, and vertical coordinates respectively.

In order to verify the accuracy of the analytic "transfer of boundary conditions" derived in Section 4 (Equations (25) through (28)), pressure distributions were computed for a purely irrotational calculation.

Figure 4 shows C_p distributions as a function of the roll angle θ, taken at the mid-chord of the body. The pressure distribution for the 2:1 ellipse corresponds to the body previously described, whereas the case labeled '1:1' corresponds to an equivalent body with a circular cross-section. In the latter case, the C_p distribution reveals the expected cosine-shaped profile, with a minimum of $Cp_{min} = -0.29$, which is the value expected from potential flow, since the cross-flow at $\theta = \pi/2$ is $q_s^2 = (2\tan\alpha)^2 = 0.287$.

Converged time-accurate solutions were also computed with flow separation (i.e., with the vorticity jet turned on). Vorticity contours in the crossflow plane are shown at successive locations along the body (Figures 5(a) through 5(d)), for a steady calculation at $\alpha = 15°$. These indicate the occurrence of vortex roll-up and intensification of the vortex strength with downstream distance. Further examination of the cross-sectional vorticity contours and of similar contours in the x-z plane indicates that the lowest vorticity levels tend to propagate in space at an angle of approximately 15° from the body (i.e., similarly to passive advection). The larger vorticity levels, on the other hand, remain close to the body surface, as expected from the induction due to the image vorticity. This behavior is consistent with experimental observation.

The decomposition of the flowfield into rotational and irrotational velocity fields is illustrated in Figure 6. Figure 6(a) shows the potential velocity component (i.e., $\nabla\phi + \sin(\alpha)\mathbf{k}$, where $\mathbf{k}$ is a unit vector in the positive z-direction) at X/D = 0.67. The rotational component $\nabla \times A$ is represented in Figure 6(b) and illustrates the presence of a formed vortex. The total velocity field (Figure 6(c)) is obtained by the superposition of rotational and irrotational flow components. The corresponding spatial evolution of the flowfield along the body is documented in Figure 7, illustrating vortex formation, strengthening, and lift-up away from the body surface.

A comparison of pressure coefficient distributions with and without the introduction of vorticity into the flowfield is provided in Figure 8 for various downstream locations. Upstream of the location where separation first occurs, irrotational and vortical C_p distributions are virtually indistinguishable from one another, as shown in Figure 8(a) for X/D = 0.23. This location incidently corresponds to the end of the nose section of the body (see Figure 1). Therefore, the asymmetric pressure distribution is a consequence of the forebody configuration. At X/D = 0.34 (Figure 8(b)), the weak rotational component of the flow produces a net reduction of surface velocities in the vicinity of the separation point and therefore an increase in pressure on the lee-ward side. This results in a local reduction in cross-sectional lift. The effect becomes more pronounced as the strength of the vortex increases (Figure 8(c)). However, at sufficiently large downstream distances (Figures 8(d) and 8(e)), the strength of the vortex becomes such that high-speed reverse flow occurs at the top surface, resulting in low pressures and increased lift. The full distributions of cross-sectional lifts and pitching moments are compared to a purely irrotational calculation in Figures 9(a) and 9(b) respectively. Although incipient separation takes place at X/D = 0.26, the enhanced lift due to flow separation is only apparent for X/D ≥ 0.4, in accordance with the above mentioned threshold in vortex strength. The total lift coefficient for this case was found to be: $C_L = 1.20$. For reference, the equivalent lift calculation using potential theory without the inclusion of vorticity effects yields $C_L = 0.54$. Similarly, the total pitching moment taken about $X_{ref}/D = 0.45$ is $C_M = -0.07$ (versus -0.25 for a purely potential calculation).

Hence, the inclusion of the rotational flow is seen to be responsible for drastic differences in the flow-induced loads on the body.

The results described in Figures 3 through 9 correspond to a steady configuration at $\alpha = 15°$. The following results examine the case of flutter about a mean angle of attack. The body motion is approximated to leading order by imposing an oscillating freestream in the crossflow plane equal to $U_\infty \sin(\alpha)$, for which α describes a simple harmonic motion: $\alpha(t) = \alpha_0 + \alpha_1 \sin(kt)$, where $\alpha_0 = 15°$ is the mean angle of attack, $\alpha_1 = 3°$ represents the motion amplitude, $k = 2\pi f L/U_\infty$ is the reduced angular frequency based on body length, and t is non-dimensional time. For most of the unsteady results presented in this manuscript, k is equal to 2π, corresponding to a flutter period of unity. For $M_\infty = 0.3$ and, say, L = 10 m, the dimensional frequency is: f = 10 Hz, which is within the range of interest for aeroelastic computations and/or active control.

The vector plots of Figure 10 illustrate the motion experienced by the vortex, as an entire cycle of the oscillation is completed. At phase $kt = \pi/2$ (Figure 10(a)), the angle of attack is maximum. In a quasi-steady sense, the strength of the vortex would also be maximum. This is not the case, however, and the vortex continues to grow in strength during the 'pitch-down' part of the motion (Figure 10(b)). This is because the excess vorticity accumulated upstream takes a finite time to convect to the current location of X/D = 0.67. As the motion proceeds (Figures 10(c) and (d)), the vortex strength diminishes. A strong correlation can also be noticed between the strength of the vortex and its spanwise location, as expected from the induced velocity due to its image.

The corresponding pressure coefficient distributions on the body surface are shown in Figure 11. These indicate the sensitivity of the vortex strength and position, as well as the associated dynamic loads to the unsteady motion. In particular, the largest negative pressures on the lee-ward side of the body ($\theta \geq 120°$) actually occur around $kt = \pi$, i.e., at the half-point of the downstroke. The global effects of unsteadiness on cross-sectional lift distributions can be assessed from Figure 12. At X/D = 0.67, the lift is maximum at $kt = \pi$, in accordance with the results of Figure 10. The crossing of the lines also indicates that the value of kt associated with, e.g., maximum lift may vary with downstream position. Finally, it is interesting to notice that for kt = 0 and kt = π, the lift distributions are almost identical upstream of flow separation (i.e., $X/D < 0.26$), whereas they differ greatly when vortical effects are present.

The total oscillating lift and pitching moment were calculated by integrating c_l and c_m. Figure 13 represents the instantaneous angle of attack and lift, as a function of non-dimensional time, for $k = 2\pi$. Substantial phase lags (approximately $\pi/2$ for the lift) with respect to the motion are observed. Similarly, the pitching moment was calculated to lag the motion by approximately $5\pi/6$. Figure 14 presents the lift coefficient time history for 1.6 periods of the oscillation, at the same reduced frequency, for the transonic case: $M_\infty = 0.9$. The solution was started from rest. It illustrates, as in the results of Figure 13, the finite physical time required for the vorticity to build up and produce the enhanced lift

8. Concluding Remarks

A theory was developed to treat flow separation and related vortex effects in unsteady transonic flow around slender bodies. This theory involves the simultaneous solution of a modified TSD equation, a vector potential equation, and a three-dimensional unsteady vorticity transport equation.

The implementation of the theory was performed using a modified version of the CAP-TSD[5] computer code. This modified versaon yields convergent and time-accurate solutions. It is shown for the first time that realistic high angle of attack configurations may be calculated using CAP-TSD, thus showing considerable potential for aeroelastic computations and unsteady aerodynamics.

Appendix

Derivation of Equations

Analysis:

The Euler equations for a steady compressible flow are

$$\rho_t + (\rho U)_x + (\rho V)_y + (\rho W)_z = 0 \tag{1}$$

$$(\rho u)_t + (\rho U^2 + p)_x + (\rho UV)_y + (\rho UW)_z = 0 \tag{2}$$

$$(\rho v)_t + (\rho UV)_x + (\rho V^2 + p)_y + (\rho VW)_z = 0 \tag{3}$$

$$(\rho x)_t + (\rho UW)_x + (\rho VW)_y + (\rho W^2 + p)_z = 0 \tag{4}$$

$$[\rho(h+1/2q^2)-p]_t + [\rho U(h+1/2q^2)]_x + [\rho V(h+1/2q^2)]_y + [\rho W(h+1/2q^2)]_z = 0 \tag{5}$$

and

$$q^2 = U^2 + V^2 + W^2 \tag{6}$$

where ρ is the density, U, V, and W are velocity components in the cartesian coordinate system (x,y,z), h is the specific enthalpy, and p is the pressure.

Manipulation of the Euler equations and the use of Gibbs relation leads to Crocco's equation

$$\bar{\nabla} h_o + \frac{\partial \bar{q}}{\partial t} + \bar{q} \times \bar{\Omega} = T \cdot \bar{\nabla} S \tag{7}$$

where S is entropy, T is temperature, $\bar{q}$ is the velocity vector given by

$$\bar{q} = \bar{i}U + \bar{j}V + \bar{k}W \tag{8}$$

and

$$\bar{\nabla} = \bar{i}\frac{\partial}{\partial x} + \bar{j}\frac{\partial}{\partial y} + \bar{k}\frac{\partial}{\partial z} \tag{9}$$

h_o is the stagnation enthalpy. The vorticity vector $\bar{\Omega}$ is defined by

$$\bar{\Omega} = \bar{\nabla} \times \bar{q} \tag{10}$$

Equation (7) can be differentiated to give

$$\bar{\nabla}\frac{\partial \bar{q}}{\partial t} + \bar{\nabla} \times (\bar{q} \times \bar{\Omega}) = \bar{\nabla} T \times \bar{\nabla} S \tag{11}$$

or, using Equation (7)

$$\frac{\partial}{\partial T}\bar{\Omega} + \bar{\nabla}(\bar{q} \times \bar{\Omega}) = \bar{\nabla} T(\bar{q} \times \bar{\Omega})/T \tag{12}$$

It may be shown that to a first approximation, Equation (12) can be written in component form as

$$\Omega_{1t} + U\Omega_{1x} + (V\Omega_1)_y + (W\Omega_1)_z = \Omega_2 U_y + \Omega_3 U_z \tag{13}$$

$$\Omega_{2t} + (U\Omega_2)_x + V\Omega_{2y} + (W\Omega_2)_z = \Omega_1 V_x + \Omega_3 V_z \tag{14}$$

$$\Omega_{3t} + (U\Omega_3)_x + (V\Omega_3)_y + W\Omega_{3z} = \Omega_1 W_x + \Omega_2 W_y \tag{15}$$

where

$$\bar{\Omega} = \bar{i}\Omega_1 + \bar{j}\Omega_2 + \bar{k}\Omega_3$$

Assume that the vorticity is produced on a slender body where the thickness to length ratio is characterized by the small parameter ε. Thus, the dimensions of the body in the y and z directions are of order ε. In order to make the dimensions of the body equal, the following transformation is used.

$$\tilde{x} = x$$

$$\tilde{y} = y/\varepsilon \qquad (16)$$

$$\tilde{z} = z/\varepsilon$$

In addition it is assumed that the velocity components U, V, W can be expanded in the usual slender body expansion to give

$$\left.\begin{aligned} U &= U_\infty\ (1 + \varepsilon^2 u) \\ V &= \varepsilon\ U_\infty v \\ W &= \varepsilon U_\infty w \end{aligned}\right\} \qquad (17)$$

The temperature, T, is also expanded as a series; thus

$$T = T_\infty(1 + \varepsilon^m T_1) \qquad (18)$$

where $m \geq 1$. Using Equations (16), (17), and (18) it can be shown that a first approximation to Equations (13), (14), and (15) is

$$\Omega_{1t} + \Omega_{1\tilde{x}} + (v\Omega_1)_{\tilde{y}} + (w\Omega_1)_{\tilde{z}} = 0 \qquad (19)$$

$$\Omega_{2t} + \Omega_{2\tilde{x}} + v\Omega_{\tilde{y}} + (w\Omega_2)_{\tilde{z}} = \varepsilon\Omega_1 v_{\tilde{x}} + \Omega_3 v_{\tilde{z}} \qquad (20)$$

$$\Omega_{3t} + \Omega_{3\tilde{x}} + v\Omega_{3\tilde{y}} + (w\Omega_3)_{\tilde{z}} = \varepsilon\Omega_1 w_{\tilde{x}} + \Omega_2 w_{\tilde{y}} \qquad (21)$$

If at some boundary the vorticity that is initiated has a vector in the x direction, then Equations (19), (20), and (21) show that to a first approximation Ω_2 and Ω_3 are negligible in comparison with Ω_1 which is then given by

$$\Omega_{1t} + \Omega_{1\tilde{x}} + (v\Omega_1)_{\tilde{y}} + (w\Omega_1)_{\tilde{z}} = 0 \qquad (22)$$

Thus, in the slender body approximation one component, the crossflow vorticity, is dominant to a first approximation, and this vorticity is transported throughout the fluid without interchanging with the other components. The neglected terms are of the order $\varepsilon\Omega_1$. In order to solve Equation (22) it is necessary to specify the boundary conditions. These boundary conditions are the location of the separation line and the magnitude of the shed vorticity. These must be found from empirical relations such as those used by Mendenhall and Perkins (Ref. 1).

Assume that the velocity field is composed of an irrotational part, denoted by the subscript i, and a rotational part, denoted by the subscript r. Assume also that only the Ω_1 component of vorticity is significant; that is, terms of order $\varepsilon\Omega_1$ are negligible. The vorticity equations then become (dropping the superscript tilde in the following for convenience)

$$V_{iz} - W_{iy} = 0; \quad V_{rz} - W_{ry} = \Omega_1 \qquad (23a)$$

$$U_{iy} - V_{ix} = 0; \quad U_{ry} - V_{rx} = \Omega_2 \approx 0 \qquad (23b)$$

$$U_{iz} - W_{ix} = 0; \quad U_{rz} - W_{rx} = \Omega_3 \approx 0 \qquad (23c)$$

In Equations (23b) and (23c) the equations for the rotational components simply duplicate the irrotational component, which suggests that a velocity potential, ϕ, exists such that

$$\begin{aligned} U_i &= 1 + \phi_x \\ V_i &= \phi_y \\ W_i &= \phi_z \end{aligned} \qquad (24)$$

and that

$$U_r = 0; \ V_{rx} = 0; \ W_{rx} = 0 \qquad (25)$$

A vector potential, $\bar{A}$ is defined as

$$\bar{q}_r = \bar{\nabla} \times \bar{A} \qquad (26)$$

where

$$\bar{q}_r = \bar{i}U_r + \bar{j}V_r + \bar{k}W_r \qquad (27)$$

and

$$\bar{A} = \bar{i}A_1 + \bar{j}A_2 + \bar{k}A_3 \qquad (28)$$

Substituting Equations (27) and (28) into Equation (23) gives

$$\left.\begin{aligned} A_{1yy} + A_{1zz} &= -\Omega_1 \\ A_2 &= 0 \\ A_3 &= 0 \end{aligned}\right\} \qquad (29)$$

and

$$V_r = A_{1z}; \quad W_r = -A_{1y} \qquad (30)$$

Since

$$A_2 = A_3 = 0$$

the subscript "1" will be omitted in the following discussion.

The equations governing the transport of vorticity are Equation (22) and the following equations

$$A_{yy} + A_{zz} = -\Omega_1 \tag{31}$$

$$\left.\begin{aligned} U &= 1 + \phi_x \\ V &= \phi_y + A_z \\ W &= \phi_z - A_y \end{aligned}\right\} \tag{32}$$

where ϕ is the velocity potential.

From Equations (25) and (32) it follows that

$$A_{zx} = A_{yx} = 0$$

The standard transonic potential wing theory can be deduced from Equations (1) and (2) with the irrotational assumption and the isentropic relation

$$p/\rho^{\gamma} = p_\infty/\rho_\infty^{\gamma} \tag{33}$$

Equation (2) can be written, using Equation (1)

$$U_t + UU_x + VU_y + WU_z = -\frac{1}{\rho}p_x \tag{34}$$

Using Equations (32) and (34), Equation (35) becomes

$$\phi_{wt} + (1+\phi_x)\phi_{xx} + (\phi_y + A_z)\,\phi_{xy} + (\phi_z - A_y)\,\phi_{xz} = \frac{1}{(\gamma-1)M_\infty^2}\left[\frac{\rho}{\rho_\infty}\right]^{\gamma-1}_{x} \tag{35}$$

Since, from Equation (33), A is not a function of x, Equation (36) can be integrated to give

$$\rho = \rho_\infty\left\{1 + \frac{(\gamma - 1)M_\infty^2}{2}\left[-2\phi_t - 2\phi_x - \phi_x^2 - \phi_y^2 - \phi_z^2 - 2A_z\phi_y + 2A_y\phi_z\right]\right\}^{\frac{1}{\gamma - 1}} \tag{36}$$

Equation (37) is an equation for ρ in terms of ϕ, A. The set of equations, Equation (1), the irrotational equations, and Equation (37) with

$$A_z = A_y = 0 \tag{37}$$

are the equations solved by the traditional potential method. In order to solve for a flow with vorticity, two additional equations, namely Equations (22) and (31), must be solved. Equation (22) gives the vorticity transport and Equation (31) the rotational velocity induced by the vorticity.

References

[1] Klopfer, G. H. and Nielsen, J. N.: Computational Fluid Dynamics Applications to Missile Aerodynamics, Paper No. 3 in AGARD CP-336, Missile Aerodynamics, September 1982.

[2] Nixon, D., Caruso, S. C., and Klopfer, G. H.: Prediction of Transonic Flow with Vortex Effects, AIAA Paper 90-0389.

[3] Klopfer, G. H. and Nixon, D., Transonic Flows with Vorticity Transport Around Slender Bodies, AIAA Journal, Vol. 27, No. 10, 1989, pp. 1461-1464.

[4] Mendenhall, M. R. and Perkins, S. C., Jr., Vortex Cloud Model for Body Vortex Shedding and Tracking. In Tactical Missile Aerodynamics, (edited by M. J. Hemsch and J. N. Nielsen), Vol. 104, Progress in Astronautics and Aeronautics, AIAA 1986.

[5] Batina, J. T.: An Efficient Algorithm for Solution of the Unsteady Transonic Small Disturbance Equation, AIAA Paper 87-0109.

[6] Nixon, D.: The Effect of Vortex Rotation on the Flow Around a Missile, NEAR Paper No. 266, Nielsen Engineering & Research, January 1990.

[7] Stratford, B. S., The Prediction of Separation of the Turbulent Boundary Layer, Journal of Fluid Mechanics, Vol. 5, 1959, pp. 1-16.

[8] Spangler, S. B. and Mendenhall, M. R.: Further Studies of Aerodynamic Loads at Spin Entry, Report ONR-CR-212-225-3, 1977.

Acknowledgement

The work described in this manuscript was sponsored by the Army Research Office under contract DAAL03-87-C-0008. The authors also wish to thank Dr. Steven C. Caruso for numerous helpful discussions.

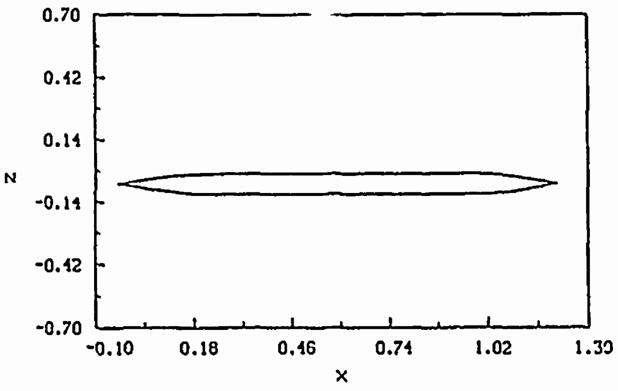

Figure 1. Planform View of the Body Geometry.

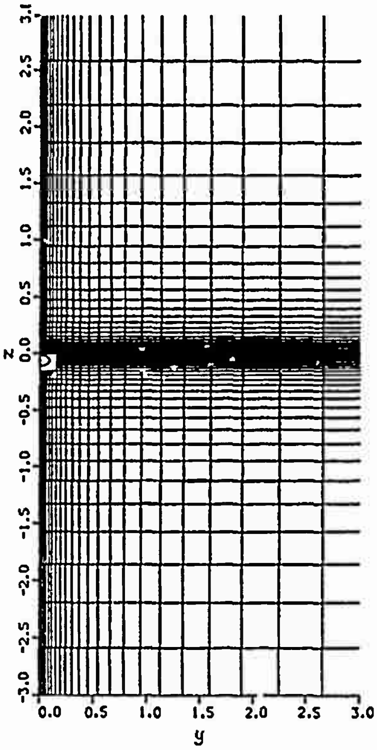

Figure 2. Cross-sectional View of the Cartesian Grid.

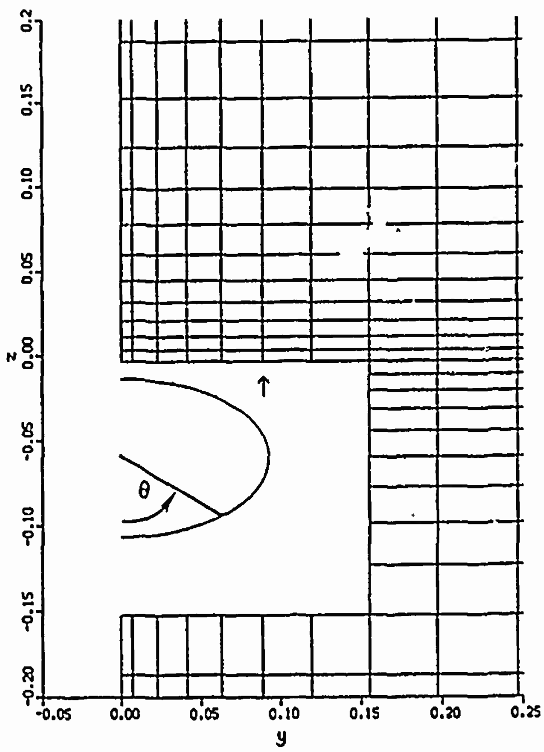

Figure 3. Body Cross-section and Roll Angle Convention.

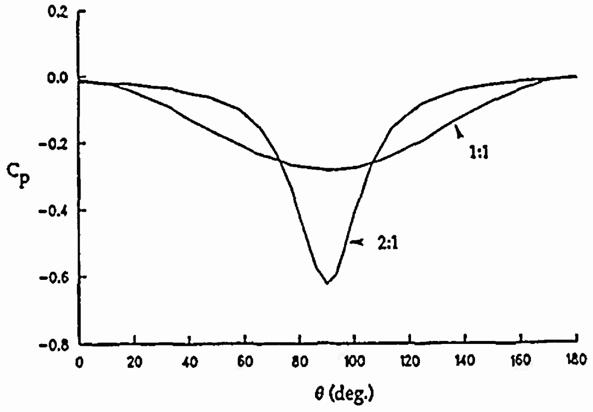

Figure 4. Calculated Irrotational Pressure Coefficient Distributions for 1:1 and 2:1 ellipses.

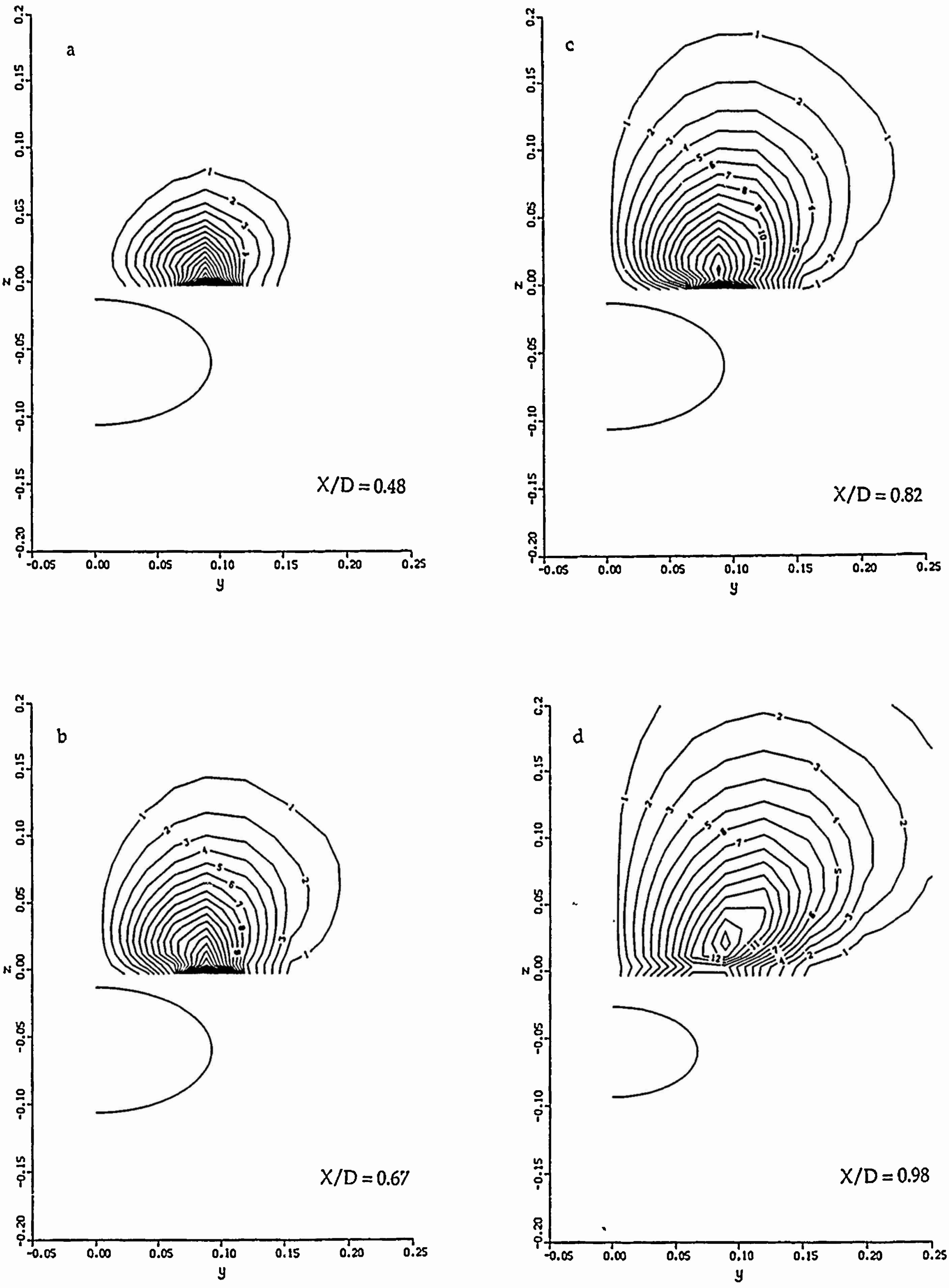

Figure 5. Cross-sectional Vorticity Contours at Various Streamwise Locations (M_∞=0.3, α=15°).

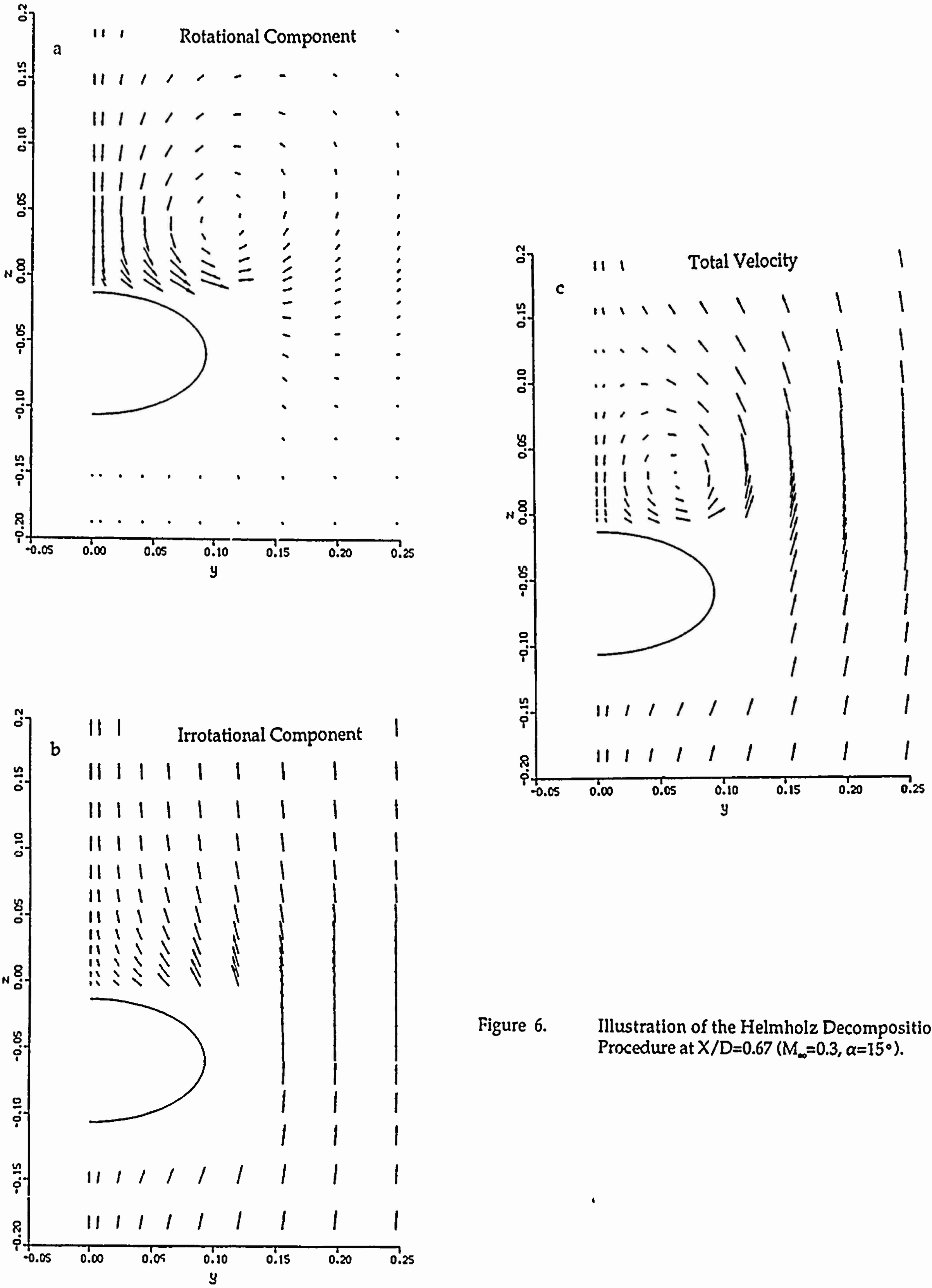

Figure 6. Illustration of the Helmholz Decomposition Procedure at X/D=0.67 (M_∞=0.3, α=15°).

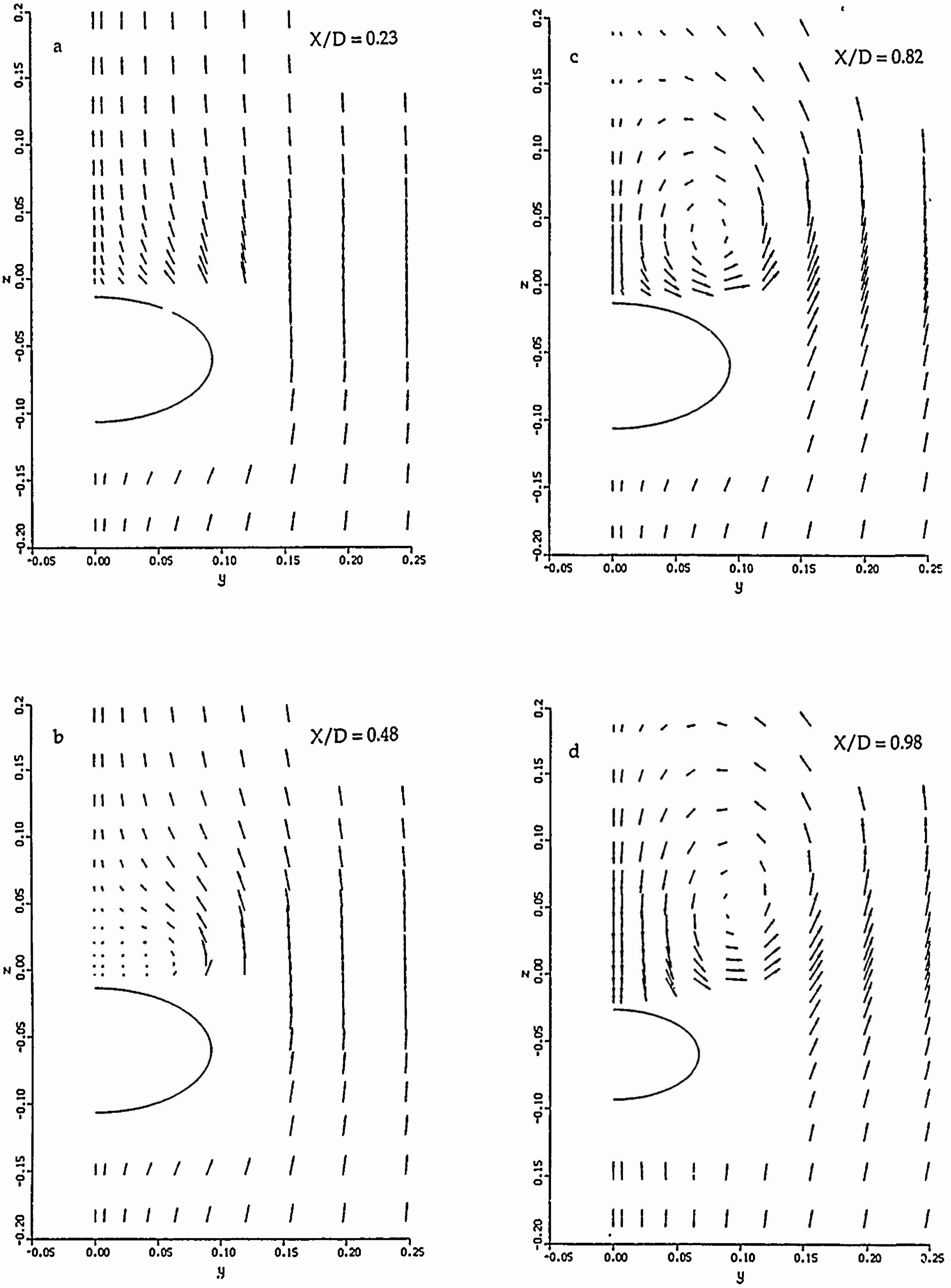

Figure 7. Streamwise Evolution of the Vertical Crossflow ($M_\infty=0.3$, $\alpha=15°$).

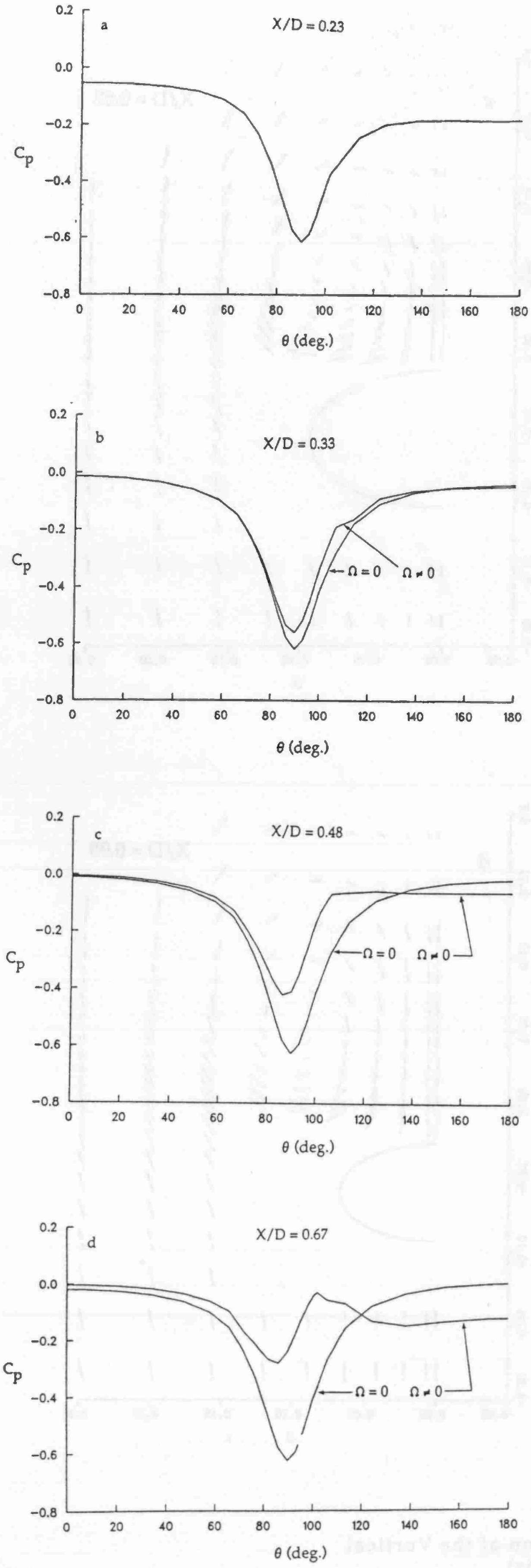

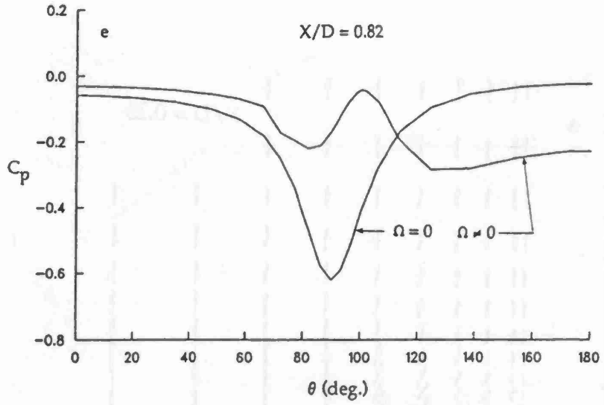

Figure 8. Comparison of Potential and Vortical Pressure Coefficient Distributions at Various Downstream Locations (M_∞=0.3, α=15°).

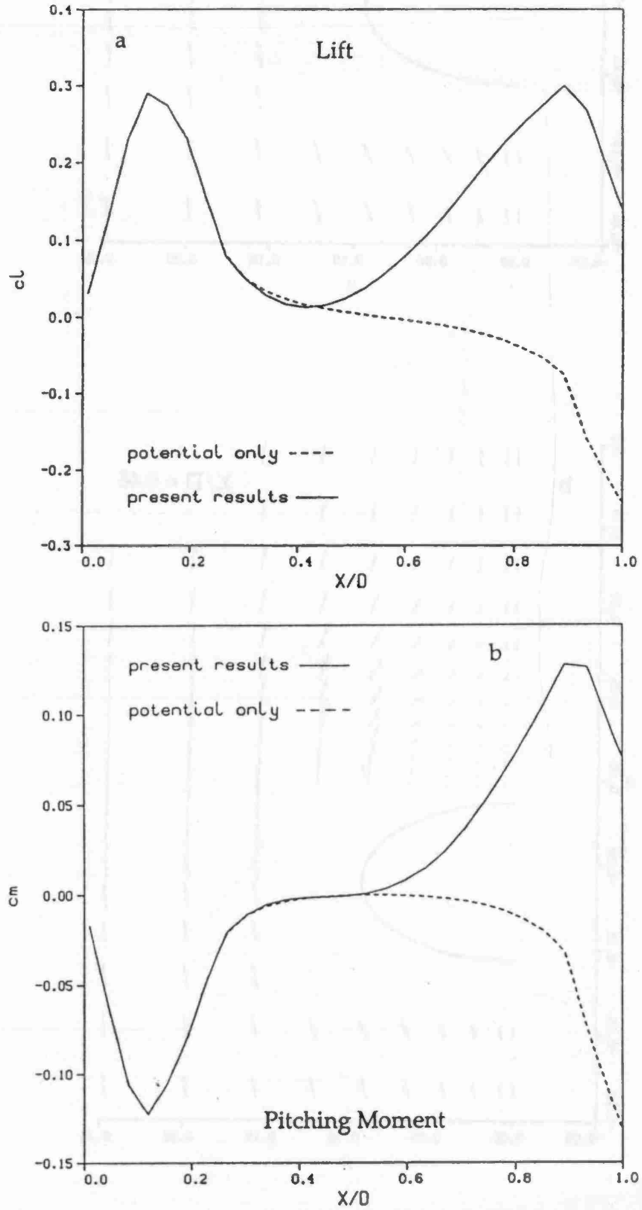

Figure 9. Comparison of Potential and Vortical Cross-sectional Lift and Pitching Moment Coefficient Profiles (M_∞=0.3, α=15°).

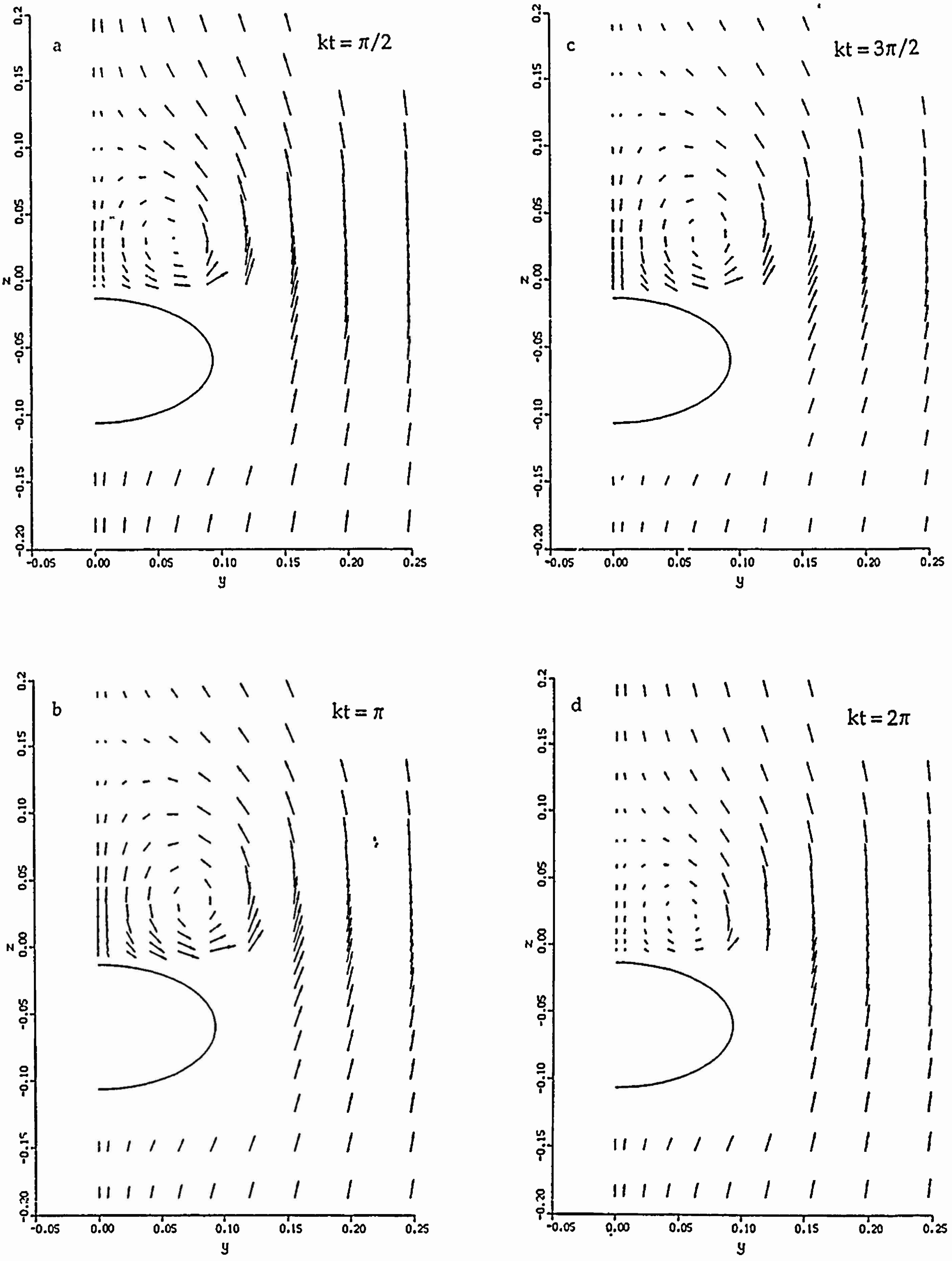

Figure 10. Comparison of Vortical Crossflows at Various Times of the Oscillatory Cycle for X/D=0.67 (M_∞=0.3, α_0=15°, α_1=3°, k=2π).

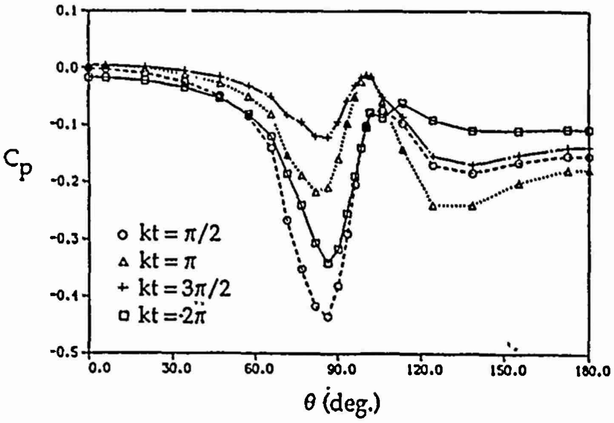

Figure 11. Comparison of Pressure Coefficient Distributions at Various Times of the Oscillatory Cycle (M_∞=0.3, α_0=15°, α_1=3°, k=2π).

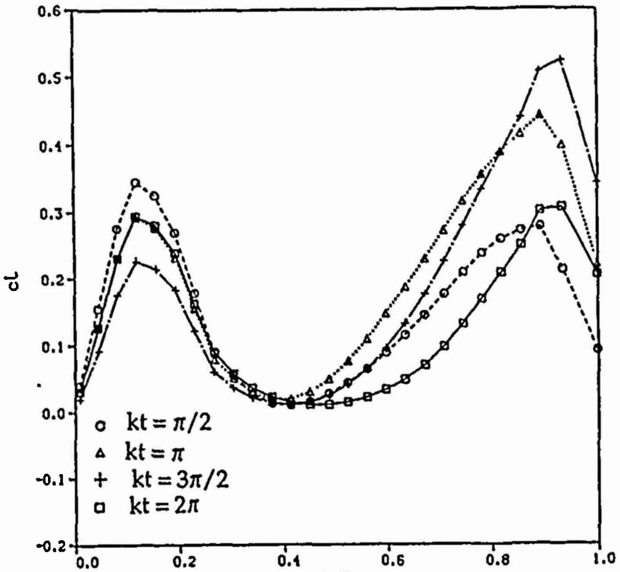

Figure 12. Comparison of Cross-sectional Lift Profiles at Various Times of the Oscillatory Cycle (M_∞=0.3, α_0=15°, α_1=3°, k=2π).

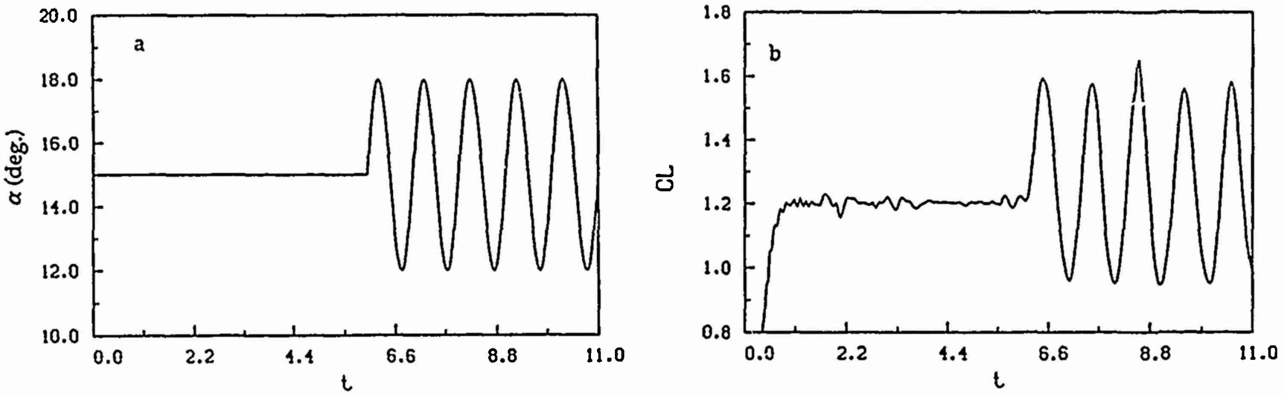

Figure 13. Time History of Angle of Attack and Total Lift Coefficient for M_∞=0.3 (α_0=15°, α_1=3°, k=2π).

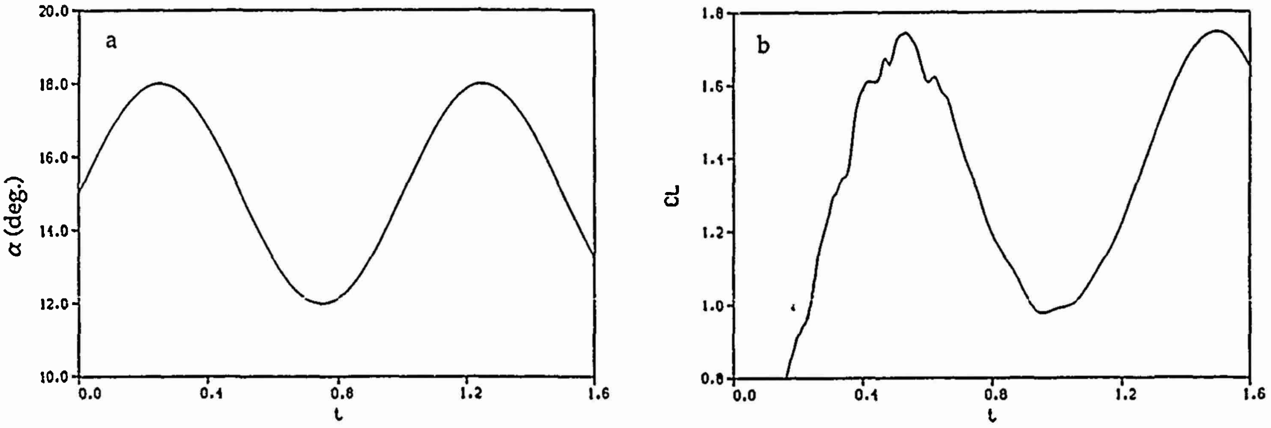

Figure 14. Time History of Angle of Attack and Total Lift Coefficient for M_∞=0.9 (α_0=15°, α_1=3°, k=2π).

APPLICATION OF INDICIAL THEORY TO THE PREDICTION OF UNSTEADY SEPARATION

Extended abstract submitted for the
AIAA 22nd Flüid and Plasmadynamics Conference,
Honolulu, Hawaii, June 24-26, 1991.

by

P. Reisenthel*
D. Nixon**
Nielsen Engineering & Research, Inc.
510 Clyde Avenue
Mountain View, CA 94123

1. Introduction

During flutter or unsteady maneuver of slender bodies, such as missiles at angle of attack, important phase delays can be observed between the unsteady loads acting on the body and the body motion itself. These phase delays result from dynamic effects, and in particular the fact that the position and strength of vortices can lag the motion of the body significantly. One of the principal causes for this effect is that the position and strength of a vortex at any streamwise location along the body are the integral consequence of vorticity transport dynamics on the one hand, and the unsteady rate at which vorticity is fed into the vortex sheet on the other. Therefore, the "history effect" may be thought of as a delay due to convection *and* to the separation process itself. It is to the latter that this manuscript is devoted.

The problem can be stated as follows: given a small change in instantaneous "outer flow conditions" at a given downstream location (these conditions already include the various convective phase delays), what are the additional delays, if any, that are associated with the separation of the boundary layer?

If Ref 1, the essence of boundary layer separation at high Reynolds numbers is characterized by a normal vorticity jet. With this representation in mind, the goal of this paper is to establish whether the unsteady characteristics of boundary layer separation, i.e., the motion of the separation point and the unsteady vorticity flux shed at that point, can be predicted.

The approach is to analyze the motion of the separation point as well as the vorticity flux in a given cross-flow plane, i.e. on a circular body, using two-dimensional Navier-Stokes calculations. The final goal is to incorporate the finding of this study into a modified version of the Stratford criterion,[2] relating the separation roll angle to the pressure gradient

---

* Research Scientist, Member AIAA

** President

history at the surface. An innovative avenue of research has been undertaken, in which an attempt is made to predict the characteristics of unsteady separation based on the knowledge of the impulse response of the separated flowfield.

2. Indicial Theory

Assume that a quantifiable entity $\mu(t)$ characterizing some aspect of flow separation can be defined (in our case μ might typically represent the separation roll angle θ_s or the normal vorticity flux associated with boundary layer separation, but is not restricted to these quantities). Consider a hypothetical change in $\mu(t)$ due to an infinitesimal change in some parameter $\varepsilon(\tau)$ at some time τ. The parameter ε represents a change in outer flow conditions which affects separation, e.g. ε may represent a small change in angle of attack, or a small change in crossflow velocity. Following the derivations of Reference 3, if μ varies continuously with ε, then the change in $\mu(t)$ may be expanded according to

$$\delta\mu(t) = \mu_\varepsilon(t,\tau)\,\frac{d\varepsilon(\tau)}{d\tau}\,\delta\tau + O(\delta\tau)^2 \qquad (1)$$

where t is time, $\delta\mu(t)$ is the change in μ resulting from a change in the forcing parameter ε at some time τ, and $\mu_\varepsilon(t,\tau)$ designates the rate of change with respect to ε of $\mu(t)$ at time τ.

Neglecting the higher order terms in Equation (1), the total integrated effect of such steps in ε from $t = 0$ until time t can be expressed as:

$$\Delta\mu(t) = \mu_\varepsilon(t,\tau)\,\varepsilon(0) + \int_0^t \mu_\varepsilon(t,\tau)\,\frac{d\varepsilon(\tau)}{d\tau}\,d\tau \qquad (2)$$

If, in addition it can be assumed that the behavior of μ with ε is linear, then $\mu_\varepsilon(t,\tau)$ can be represented by its value at $\tau = 0$ provided that t is taken relative to τ. Thus

$$\mu_\varepsilon(t,\tau) = \mu_\varepsilon(t-\tau,0) \equiv \mu_\varepsilon(t-\tau) \qquad (3)$$

where the functional form of μ_ε has been contracted for notational convenience.

Substituting Equation (3) in Equation (2) yields, after a simple change of variable

$$\Delta\mu(t) = \mu_\varepsilon(t)\,\varepsilon(0) - \int_0^t \mu_\varepsilon(\tau)\,\frac{d\varepsilon(t-\tau)}{d\tau}\,d\tau \qquad (4)$$

Equation (4) states that, under the linearity assumptions afore mentioned, one can analytically predict the change $\Delta\mu(t)$ due to an arbitrary change in the forcing parameter ε, provided that the *indicial response*, μ_ε, is known. Equation (4) illustrates the power of the indicial method, since the response $\Delta\mu$ may be calculated from the knowledge of the excitation parameter ε, and that of the indicial response μ_{ε}, which requires only a single experimental or numerical determination.

Although indicial theory has traditionally been used in unsteady aerodynamics (see e.g. Tobak,[4] 1954, Jenkins,[5] 1988) the work presented in this manuscript is, to the authors' knowledge, the first attempt at applying this concept to the problem of flow separation.

The approach is to impose a step change in Mach number (the case of Reynolds number changes is deferred to the Appendix) to the separated flowfield about a circular cylinder, and record the indicial responses of separation roll angle, shed vorticity flux, and drag. Once these indicial responses are recorded, the validity of the indicial method is tested by evaluating the accuracy of the prediction given by Equation (4) against the actual (numerically computed) change $\Delta\mu(t)$ due to some arbitrary change in ε. Details of this procedure are given in the Results section.

3. Computer Code and Boundary Conditions

The two-dimensional Navier-Stokes calculations were implemented on a 245 x 79 C-mesh grid. The grid was a four-fold spatial refinement of that used by Rodman,[6] with a symmetry boundary condition on the centerline. This symmetry condition ('inviscid splitter plate' condition) at $y = 0$ was imposed upstream and downstream of the circular cylinder so as to prevent vortex shedding beyond the critical Reynolds number. This was a necessary precaution since this regime is not observed in the three-dimensional flow (i.e. slender body at moderate angle of attack) of which the two-dimensional cylinder constitutes a simplified crossflow representation. The C-grid had a total streamwise extent of 25 diameters, and extended 5 diameters in the normal direction, away from the centerline.

A detail of the grid is shown in Fig. 1. In this Figure, the flow direction is from left to right, and the sign convention for the roll angle, θ, is taken to be in the clockwise direction, for consistency with references 1 and 7. (i.e. $\theta = 0°$ at the windward stagnation point). The computer code that was used for all of the calculations presented in this paper was ARC2D.[8] This code uses an approximate factorization finite difference scheme. The time integration was performed with a 3-point second order accurate implicit method. At the outer boundaries, a characteristic-like boundary condition procedure using locally one-dimensional Riemann invariants (see Pulliam,[8] 1984) is implemented. At the cylinder surface, the no-slip boundary condition is applied.

In order to simulate instantaneous changes in angle of attack of the three-dimensional slender body, the two-dimensional cylinder is accelerated through the flow by moving the computational grid. The ARC2D code possesses time-metric terms which allowed the computational grid to be translated with relative ease. Using a minor amount of post-processing it is then possible to examine the solution flowfield in a frame of reference attached to the body, therefore simulating a change in freestream velocity.

For a viscous compressible flow, conservation of momentum may be expressed as:

$$\frac{\partial}{\partial t}(\rho u_i) + \frac{\partial}{\partial x_j}(\rho u_i u_j) = -\frac{1}{\gamma M_\infty^2}\frac{\partial p}{\partial x_i} + \frac{1}{Re}\frac{\partial}{\partial x_j}\left[\mu\left(\frac{\partial u_i}{\partial x_j} + \frac{\partial u_j}{\partial x_i}\right) + \mu_v \delta_{ij}\frac{\partial u_k}{\partial x_k}\right] \quad (5)$$

where the velocity components u_i are non-dimensionalized by the freestream velocity U_∞. The coordinates x_i are non-dimensionalized by the cylinder diameter D, and ρ, p, and μ are non-dimensionalized by their respective freestream values. In Equation (5), use is made of the perfect gas assumption

$$\frac{1}{\gamma M_\infty^2} = \frac{p_\infty}{\rho_\infty U_\infty^2} \quad (6)$$

and the Reynolds number Re is based on the freestream velocity: $Re = \rho_\infty U_\infty D/\mu_\infty$. Hence, with this formulation, a change ΔU_∞ in freestream velocity results in the simultaneous change of both Mach number ($\Delta M_\infty = \Delta U_\infty / a_\infty$) and Reynolds numbers ($\Delta Re = \rho_\infty \Delta U_\infty D/\mu_\infty$).

It is possible to vary only one parameter if, instead, the velocity components are non-dimensionalized by the freestream speed of sound a_∞. Substituting $u_i' = M_\infty u_i$ and $t' = t/M_\infty$ in Equation (5) and using continuity yields (dropping the prime superscript for notational convenience).

$$\rho\frac{\partial u_i}{\partial t} + u_j\frac{\partial}{\partial x_j}\cdot u_i = -\frac{1}{\gamma}\frac{\partial p}{\partial x_i} + \frac{1}{Re_a}\frac{\partial}{\partial x_j}\left[\mu\left(\frac{\partial u_i}{\partial x_j} + \frac{\partial u_j}{\partial x_i}\right) + \mu_v \delta_{ij}\frac{\partial u_k}{\partial x_k}\right] \quad (7)$$

where

$$Re_a = \frac{Re}{M_\infty} = \frac{\rho_\infty a_\infty D}{\mu_\infty} \quad (8)$$

is the Reynolds number based on freestream sound speed.

Equation (7) is precisely the form of the momentum equations being solved by ARC2D. Therefore, for a fixed cylinder diameter D and given fluid properties, the Reynolds number Re_a remains constant. Hence any change of the freestream velocity is obtained either by changing the Mach number (which then affects the solution through the farfield boundary conditions), or by translating the computational grid and imposing that the velocity at the cylinder surface equals that of the grid.

Since the non-reflective characteristic outer boundary conditions use locally one-dimensional approximations, it was determined that the most accurate way of implementing a change in freestream velocity is to set the computational grid in motion.

An example of this procedure is shown in Figure 2. A steady state solution with crossflow Mach number $M_c = 0.25$ is first computed. At t = 0, the cylinder is impulsively translated either with or against the flow (top and bottom graphs respectively), at a speed equal to some percentage of the freestream velocity. Figure 2 illustrates typical velocity profiles in a reference frame attached to the cylinder, at a time $tU_c/D = 1.0$ after the initiation of the grid motion. The top graph corresponds to an effective Mach number change $\Delta M_c = -0.025$, while the bottom graph (cylinder moving against the flow) corresponds to $\Delta M_c = +0.025$.

4. Results

In order to simulate the steady symmetric leeward vortex system present in slender body flow at moderate angle of attack, the asymmetric vortex shedding phenomenon was inhibited by imposing a symmetry boundary condition at y = 0. At the high Reynolds numbers typical of missile flow, the separating boundary layer takes the form of a thin vortex sheet. The separation process can therefore be simulated[7] using a concentrated normal vorticity jet placed at the body surface. In a two-dimensional simulation of the crossflow, however, the Reynolds number based on diameter must remain low (i.e. of the order of 100 or less) in order to best approximate the topology of the flowfield. This constraint originates from the fact that in two dimensions vortex shedding occurs beyond a critical Reynolds number $Re \simeq 40$. If shedding is suppressed by means of a splitter plate, the flow exhibits elongated regions of separated flow which do not adequately represent the leeside vortices of an inclined cylinder. For this reason, the two-dimensional Navier-Stokes calculations presented here are restricted to the Reynolds number range $20 \leq Re \leq 90$.

At these relatively low Reynolds numbers, the separating boundary layer does not take the form of a vortex sheet, but rather that of a thick vorticity layer separating from the surface, as seen from the vorticity contours of Figure 3. A close examination of these typical vorticity contours reveals that the vorticity jet representation may not be adequate at the low Reynolds numbers which are needed to match the range of observed separation angles in the three-dimensional configuration.

These observations suggest that a criterion which should emulate the asymptotic (high Reynolds number) vorticity jet representation must be based on the tracking of the line of vorticity maximum. Such a criterion should also prove to be superior, in principal, to the detection of flow reversal at the surface since the latter is known to be inadequate in unsteady flow as an indicator of flow separation location.

A typical plot of the radial location of vorticity maximum as a function of roll angle is shown in Figure 4. It can be established from this plot and an analysis of the corresponding steady flowfield that as long as the flow remains attached, the maximum of vorticity lies along the surface (i.e. $r/D = 0.5$ in Figure 4). At a critical roll angle θ_s (separation roll angle), the vorticity maximum departs from the surface. In the asymptotic high Reynolds number case, the locus of vorticity maxima presumably coincides with the location of the separating vortex sheet. Based on these remarks, the separation roll angle was defined as follows: according to the previously described detection criterion, the maximum of vorticity is found at the surface when the boundary layer is attached. Hence in that region, the normal gradient $\partial\Omega/\partial n$ (where n designates the outward normal coordinate) is negative. On the other hand, when the flow is separated, the vorticity maximum occurs away from the surface ($r/D > 0.5$) and the normal vorticity gradient $\partial\Omega/\partial n$ becomes positive.

Therefore, the zero-crossing of the normal vorticity gradient can be found by linear interpolation of $\partial\Omega/\partial n$ with respect to θ, and subsequently used as a continuous indicator of the separation roll angle. The linear interpolation scheme also allows to partially overcome an inherent lack of spatial resolution, since changes in the separation location θ_s are often quite small and typically of the order of the grid resolution itself (see Appendix A). As mentioned in Section 2, θ_s thus defined represents one of the quantifiable entities $\mu(t)$ characterizing flow separation. The second quantity of interest is the vorticity flux at the point of separation. The Stratford criterion[2] assumes that a fraction λ of the tangential vorticity flux across the attached boundary layer gets injected into the freestream at the point of separation. It is justified, therefore, to consider the time-dependent behavior of the tangential vorticity flux across a fixed contour which cuts the boundary layer independent of the instantaneous location of the separation point. For convenience, such a contour was chosen to coincide with the normal grid line such that the roll angle of its intersection with the cylinder surface was 90°. This line is the baseline of the centered velocity profiles in both graphs of Figure 2.

The tangential vorticity flux across this line was numerically integrated at each time step between $r = D/2$ and the outward boundary of the computational domain. By convention, it will be denoted $\int \Omega u_\theta dr$ and referred to as the "vorticity flux" throughout the remainder of this manuscript.

Typical indicial responses are shown in Figure 5 for the separation point and the vorticity flux, in the case of a 1% velocity increase at $M_c = 0.25$. In both graphs, $t = 0$ is the time at which the cylinder was set in motion. The two graphs are plotted on the same time scale, so that the time responses $\Delta\theta_s$ and $\Delta\int \Omega u_\theta dr$ can be easily compared. It is evident that the separation roll angle reacts to the instantaneous change in velocity with a relatively short time constant: after undergoing a sharp positive spike (instantaneous reattachment), the separation point relaxes back to a position slightly upstream of the initial separation angle. The time constant associated with the relaxation process is seen to be quite small, since θ_s approaches its asymptotic value within a fraction of a unit convection time.

The vorticity flux, on the other hand, experiences a significantly longer transient behavior, and exhibits a broad overshoot after the initial step. As can be anticipated from Equation (4), θ_s and $\int \Omega u_\theta dr$ will therefore display significantly different responses to arbitrary stimuli.

In order to establish the validity bounds of the indicial theory described in Section 2, the test disturbance $\varepsilon = \Delta M_c$ is taken to be of the form $e^{ik't}$, where $i^2 = -1$ and k' is the reduced angular frequency based on diameter and crossflow velocity. The advantages of using a sinusoidal disturbance include: *i)* ease to quantify the accuracy of the prediction through a decomposition into phase and amplitude responses, and *ii)* establishing frequency bounds for the application range of Equation (4). One of the objectives of the present study is to determine whether indicial theory can be used to predict the unsteady motion of the separation angle and the unsteady vorticity flux. Such predictions ought to be possible if these processes are time-linearizable.[3] The extent to which this condition is satisfied in unknown a priori, but is likely to be a function of amplitude.

Substituting $\varepsilon = e^{ik't}$ into Equation (4) yields

$$\Delta\mu(t) = \mu_\varepsilon(t) + ik' e^{ik't} \int_0^t \mu_\varepsilon(\tau) e^{-ik'\tau} d\tau \tag{9}$$

Let $\mu_\varepsilon(\tau)$ be arbitrary but such that

$$\begin{cases} \mu_\varepsilon(\tau) = 0 & \text{for } \tau < 0 \\ \mu_\varepsilon(\tau) = \mu_{\varepsilon,\infty} & \text{for } \tau > T \end{cases} \tag{10}$$

Substituting in Equation (9) and keeping only time periodic terms (i.e. considering the transient-free response as t→+∞) yields:

$$\Delta\mu(t) \underset{t\to\infty}{=} e^{ik't} \left\{ \left[k' \int_0^T \mu_\varepsilon(\tau) \sin(k'\tau) d\tau + \mu_{\varepsilon,\infty} \cos(k'T) \right] + \right.$$

$$\left. i \left[k' \int_0^T \mu_\varepsilon(\tau) \cos(k'\tau) d\tau - \mu_{\varepsilon,\infty} \sin(k'T) \right] \right\} \tag{11}$$

Hence the phase difference between the excitation and the response is given by

$$\Delta\phi = \operatorname{atan} \left\{ \frac{k' \int_0^T \mu_\varepsilon(\tau) \cos(k'\tau) d\tau - \mu_{\varepsilon,\infty} \sin(k'T)}{k' \int_0^T \mu_\varepsilon(\tau) \sin(k'\tau) d\tau + \mu_{\varepsilon,\infty} \cos(k'T)} \right\} \tag{12}$$

while the amplitude A(k') of the response is given by the modulus of Equation (11). If A(k') is normalized by its value at k' = 0 (i.e. the quasi-steady amplitude of the response), one obtains the *attenuation factor*:

$$\frac{A(k')}{A(0)} = \sqrt{ \left[k' \int_0^T \frac{\mu_\varepsilon(\tau)}{\mu_{\varepsilon,\infty}} \sin(k'\tau) d\tau + \cos(k'T) \right]^2 + \left[k' \int_0^T \frac{\mu_\varepsilon(\tau)}{\mu_{\varepsilon,\infty}} \cos(k'\tau) d\tau - \sin(k'T) \right]^2 } \tag{13}$$

Equations (12) and (13) are the indicial method prediction of phase delays and attenuation factors, as a function of the angular reduced frequency k'.

The accuracy of this prediction was tested against the solution of actual integrations of the Navier-Stokes equations at specific frequencies. These frequencies were typically chosen to be at critical points (i.e. extrema, inflection points, etc...) of the analytically predicted response curves, or based on the range of reduced frequencies of practical interest. The most severe unsteady effects (highest frequencies) occur in situations of missile flutter, rather than maneuver. In this worst case scenario the range of amplified frequencies[9] is $5\text{Hz} < f < 30\text{Hz}$. Let $k = 2\pi fL/U_\infty$ be the reduced angular frequency based on body length and freestream velocity, then at an angle of attack α, the reduced frequency seen in the crossflow plane (i.e. based on crossflow velocity and diameter) is: $k' = 2\pi fD/U_c = 2\pi Da_\infty^{-1}(\sin\alpha)^{-1}\ f/M_\infty$. The reduced frequency k' is therefore maximized with maximum frequency, f, maximum diameter D, minimum freestream Mach number, and minimum angle of attack. Since for typical missile aspect ratios, steady separation does not occur until $\alpha \geq 10°$, one may deduce that a value $k' - 10$ represents the "flutter boundary". For this reason, direct numerical verification of frequency effects were constrained to the range $k' \leq 20$.

A comparison of analytically predicted and numerically computed phase delays and attenuation factors is presented in Figure 6, for the vorticity flux. The solid line represents the prediction based on the convolution (Equation (4)) with the indicial response of the vorticity flux (Figure 5), corresponding to a 1% step in Mach number. The equivalent prediction corresponding to a 10% change in velocity (computed to evaluate linearity bounds) is also displayed for comparison (dashed line). In both cases, the predictions are based on an "averaged" indicial response (i.e. the average of the response to a positive step on the one hand and the negative of the response to a negative step on the other). In the present case, the "positive" and "negative" responses were fairly symmetric, so that the averaging process is not fundamental to the results, but rather was performed for consistency of the data processing with cases of more pronounced asymmetry.

As may be seen from Figure 6 the results of the numerical integrations (symbols) follow closely the analytical curves, with an overall better agreement with the 10% amplitude case. This may be due to the higher resolution of the large amplitude case. In any event, a significant (50%) *overshoot* of the vorticity flux amplitude is predicted and observed at a frequency $k' = 2$, which is well within the range of observed flutter frequencies. A phase lag of approximately 30° is reached around $k' = 5$. Both of these dynamic effects may have profound consequences for flow prediction using quasi-steady implementations of separation criteria.

Unlike the vorticity flux, the indicial responses (positive and negative) of the separation angle θ_s become asymmetric at large amplitudes, as illustrated in Figure 7. As will be shown shortly, this asymmetry (which reflects nonlinearity) is associated with a severe deterioration of the prediction accuracy of the indicial method. The positive step case (cylinder moving against the flow at 10% of the freestream velocity) is characterized by the instantaneous creation of vorticity at the body surface, which translates into a negative vorticity gradient at the wall.

Hence the flow reattaches instantly (according to the detection criterion presented above) at time t = 0. This spike in $\Delta\theta_s$ is followed by a long transient (of the order of one unit convective time), corresponding to a period of upstream-moving separation. When the cylinder is impulsively translated with the flow (dashed line), the boundary layer instantly detaches (negative spike), and slowly recovers to a separation angle located downstream of the original location. a comparison with the small amplitude step response of Figure 5 indicates that the transient time increases with amplitude. At small amplitudes (1% or less), the indicial responses in θ_s were observed to be symmetric within a few percent. At larger amplitudes, the asymmetry seems to stem from the fact that the speed at which the separation point travels along the surface depends on whether the separation is "upstream-moving" or "downstream-moving".

The predictive accuracy of the indicial method for the separation point location was evaluated against selected numerical experiments, similarly to the vorticity flux. The results of these comparisons is shown in Figure 8. As expected from the above discussion, the computations at the low (one percent) amplitude are in good agreement with the solid-curve prediction. At the low amplitude the shape of the indicial response was observed to be independent of the direction of the step, which is consistent with the idea of local linearity which underlies the applicability of indicial theory as outline in Section 2.

For the large amplitude oscillations (i.e. peak cylinder velocity equal to 10% of freestream), a significant amount of harmonic distortion of the separation angle was observed, as shown in the inset of Figure 8. The harmonic distortion is indicative of the nonlinearities which are also reflected in the asymmetry illustrated in Figure 7. Because the numerically computed time-series $\theta_s(t)$ covered too few cycles of the fundamental (forcing) oscillation, adequate narrow-band frequency filtering was not attempted. Instead, the amplitude of the oscillation was simply defined as the half of the peak to peak amplitude, while the phase was calculated from the average of temporal offsets of minima and maxima between forcing and response signals. Due to the severe asymmetry of the waveforms, the uncertainty on the phase delays thus measured was considerable, as indicated by the uncertainty bars in Figure 8. Despite the uncertainty, it may be seen that the estimated phase delay remains close to the predicted curve for $k' < 10$. At the highest frequency, the numerical solution appears to follow more closely the small amplitude prediction. For the attenuation factor, $A(k')/A(0)$, the prediction remained within 25% of measurement at all frequencies.

In spite of these inaccuracies, several important features may be extracted from the results of Figure 8. First, there is a very rapid phase adjustment from 0° to -90° occurring before $k' = 1$. As will be demonstrated in Appendix B, this adjustment can be theoretically predicted based on a simple model for the indicial response involving the superposition of a Heaviside step function with an exponential relaxation curve. It may be shown in particular, that the width of this frequency window is inversely proportional to the time constant of the relaxation phase and to the square root of the amplitude of the initial pulse. The narrowing of the adjustment window with increasing amplitude is visible in Figure 8 Secondly, the attenuation factor is seen to be larger than unity at all frequencies, indicating an amplification of fluctuations of the separation angle. As shown in Figure 8, a tenfold amplification factor can be obtained at relatively low reduced frequencies, underlining once again the importance of unsteady effects on the dynamics of flow separation.

As a final test of the applicability of indicial theory to boundary layer separation, an investigation was also made into the prediction of oscillatory drag for viscous flow around a two-dimensional cylinder. The goal of this investigation was to establish whether concepts of indicial theory would also be applied to predict oscillatory lift on a missile-like body undergoing flutter.

Typical indicial responses are shown in Figure 9 for viscous and pressure drag components, as well as for the total drag. It may be seen that although it is the viscous drag which is responsible for the ultimate decrease in total drag coefficient with increasing velocity, the overall character of the transient response is imposed by the behavior of the pressure drag. While the viscous drag indicial response is characterized by an extremely narrow initial pulse, both pressure and total drags qualitatively exhibit the same features as the indicial response of the separation angle. The existence of an initial adjustment window for the phase response should therefore be expected, as well as the rapid amplification of fluctuations with reduced frequency (a feature also predicted by the model discussed in Appendix B).

This is numerically verified in Figure 10. In the top graph the quasi-steady phase of the pressure drag is -180°, reflecting a sign inversion that was applied so that the final (quasi-steady) value of all drag component indicial response have the same sign, in order to facilitate the comparison. At all tested amplitudes and frequencies, the agreement is seen to be excellent.

5. Concluding Remarks

It has been shown for viscous flow about a two-dimensional cylinder, that several key aspects characterizing the time-dependent behavior of boundary layer separation can be predicted within a reasonable degree of accuracy over a large range of frequencies. The analytical prediction involved only a convolution integral based on the knowledge of the step response of the flowfield to a small perturbation. The perturbations under consideration were changes in Mach number and Reynolds number. The test functions that were used to evaluate the range of applicability of indicial theory to the separation process were: the separation angle, the vorticity flux across the separating boundary layer, and the drag coefficient.

Although the overall agreement between the indicial method prediction and the results of direct numerical simulations was clearly superior in the case of integral quantities such as drag and vorticity flux, the location of the separation point was found to be satisfactorily predicted within the range of frequencies corresponding to missile flutter. The breakdown of the method appears to coincide with the advent of nonlinearity, which is first conveyed by an asymmetric response to positive and negative step inputs.

Although the present results are limited to low Reynolds number, laminar flow, they establish for the first time that the unsteady characteristics of two-dimensional flow separation may be predicted using indicial theory. Whether such ideas are applicable to high Reynolds number turbulent flow remains to be established.

6. Acknowledgment

The authors gratefully acknowledge the support of this work by the Army Research Office, under contract DAAL03-87-C-0008.

List of References

[1] Reisenthel, P. and Nixon, D.: Prediction of Unsteady Separated Transonic Flow Around Missile Configurations, AIAA Paper 91-0601, to be presented at the AIAA 29th Aerospace Sciences Meeting, Reno, NV, January 7-10, 1991.

[2] Stratford, B. S.: The Prediction of Separation of the Turbulent Boundary Layer, Journal of Fluid Mechanics, Vol. 5, 1959, pp. 1-16.

[3] Nixon, D.: Alternative Methods for Modeling Unsteady Transonic Flows, Unsteady Transonic Aerodynamics, Vol. 120 of Progress in Astronautics and Aeronautics, ed. by D. Nixon, AIAA 1989.

[4] Tobak, M.: On the Use of the Indicial Function Concept in the Analysis of Unsteady Motion of Wings and Wing-Tail Combinations, NACA Rept. 1188, 1954.

[5] Jenkins, J. E.: Relationships Among Nonlinear Aerodynamic Indicial Response Models, Oscillatory Motion Data, and Stability Derivatives, AIAA Paper.

[6] Rodman, L. C.: The Application of Non-Reflecting Boundary Conditions to 2-D Unsteady Computations on Curvilinear Grids, AIAA Paper 90-1587.

[7] Nixon, D., Reisenthel, P., Torres, T. O., and Klopfer, G. H.: Prediction of Unsteady Transonic Flow Around Missile Configurations, AIAA Paper 90-0934.

[8] Pulliam, T. H.: Euler and Thin Layer Navier Stokes Codes ARC2D-ARC3D, Notes for Computational Fluid Dynamics User's Workshop, Tullahoma, TN, March 12-16, 1984.

[9] Lesieutre, D. J., Nixon, D., Dillenius, M. F. E., and Torres, T. O.: Analysis of Missiles Flying Low Over Various Sea States, NEAR TR-408, November 1989.

APPENDIX A

PERTURBATIONS IN REYNOLDS NUMBER

It was shown in Section 3 that the process of impulsively translating the entire computational grid is that closest to a crossflow plane simulation of a change in angle of attack. In this section, the concept of perturbing a separated flow solution of the Navier-Stokes equations is pursued further by considering the effect of Reynolds number change. As explained earlier, the Reynolds number in the ARC2D code is that based on cylinder diameter and speed of sound. Hence, any change in $Re = M_\infty Re_a$ at a fixed Mach number should be interpreted as either a change in cylinder diameter or (more appropriately in the present case) as a change in kinematic viscosity. The present section addresses the problem of evaluating the limits of applicability of indicial theory when a solution is perturbed in Reynolds number.

Figure 11 documents the change in separation angle θ_s as a function of Reynolds number, for steady-solutions of the Navier-Stokes equations. Thus, the Reynolds number can be chosen to control the initial angle at which the boundary layer separates.

A methodology similar to that described in Section 4 was employed here. The impulse response of the separation angle θ_s is first recorded. The responses associated with positive and negative steps in Re are suitably averaged and used with a hypothetical Reynolds number oscillation in the convolution integral, Equation (4). From Equation (11), phase and attenuation frequency responses are obtained (Equations (12) and (13)). These prediction curves are then compared to the results of direct numerical simulations where Re is oscillated sinusoidally about a mean.

Figure 12 presents such results for the phase delay prediction at various Reynolds numbers. Since Reynolds number and separation angle are quasi-statically anticorrelated (see Figure 11), the phase difference $\Delta\phi$ actually involves the negative of the Reynolds number variation, so a to have $\Delta\phi = 0°$ at $k' = 0$. The phase prediction is seen to be highly accurate at Re = 40 and Re = 60. In these two graphs the dashed line indicates a simplified prediction replacing Equation (11). This prediction substitutes an exponential least square fit to the actual indicial response, i.e. it is assumed that the indicial response is of the type $\theta_s(t) = \theta_s(0) + (\theta_s(\infty)-\theta_s(0))(1 - e^{-bt})$. It is then easily shown[3] that in response to a purely periodic perturbation $\varepsilon(t)$ of angular reduced frequency k', the asymptotic response $\theta_s(t)$, as $t \to \infty$, will exhibit a phase lag equation

$$\Delta\phi = -\mathrm{atan}(k'/b) \tag{14}$$

and an amplitude attenuation factor

$$A(k')/A(0) = \frac{1}{\sqrt{1 + \left(\frac{k'}{b}\right)^2}} \tag{15}$$

It is clear that the simplified prediction of Equation (14) becomes at the higher frequencies, therefore stressing the importance of the details of the indicial response.

At Re = 90 (bottom graph, Figure 12), the prediction is quite poor. A possible explanation resides in the reduced resolution in the determination of θ_s. As may be seen from Figure 11, the decreased sensitivity $d\theta_s/dRe$ at Re = 90 implies total angular variations $\Delta\theta_s$ of only a few degrees, which is of the order of the grid resolution itself. The lack of spatial resolution is illustrated in Figure 13. The dashed line represents the average of the two roll angles delimiting the computational cell in which the normal vorticity gradient $\partial\Omega/\partial n$ crosses zero at any point in time. The solid lines represent the actual (positive and negative) indicial responses, obtained by linear interpolation of $\partial\Omega/\partial n$. Finally, the dotted lines represent crude exponential fits to the indicial responses. Figure 13 shows that a significant amount of asymmetry is already present at Re = 40 but does not seem to significantly impair the accuracy of the prediction (top graph, Figure 12). At Re = 90, a deterioration of both the angular resolution and the degree of symmetry of the step responses was observed. It is believed that these factors account for the poor agreement observed in Figure 12 (bottom graph). The influence of the asymmetry between positive and negative indicial responses is also shown in this Figure.

Figure 14 depicts similar comparisons for the attenuation factor of the oscillatory separation angle at Re = 40, Re = 60, and Re = 90. The validity of the simplified predictions based on an exponential fit of the indicial response applies to a smaller frequency range than for the case of phase lag prediction. The numerically computed results are in qualitative agreement with the full analytical prediction. The apparently large errors (~20%) may be attributable to the lack of spatial resolution for all cases involving Reynolds number perturbations.

Figures 15 and 16 depict the phase and attenuation results at a fixed initial Reynolds number, for crossflow Mach numbers of $M_c = 0.1$, $M_c = 0.25$, and $M_c = 0.4$. At the lowest Mach numbers, the phase lag prediction are in excellent agreement with the results of the direct numerical simulations. However, in the case $M_c = 0.4$, both predicted phase lags and attenuation factors strongly deviate from the numerical results. As in the higher Reynolds number case, the importance of the asymmetry between positive and negative step response is indicated by the corresponding individual predictions in Figures 15 and 16 (bottom). In this case, the origin of the asymmetrical responses is not known, although is may be conjectured that compressibility effects may have come into play, since shocks are known to appear at freestream Mach numbers as low as ≈0.55. In any event, the lack of spatial resolution may also have played an important role, since the total variation in static separation angle θ_s between $M_c = 0.1$ and $M_c = 0.4$ at Re = 60 was less than 0.7°, in comparison with a total spread of approximately 9° between Re = 40 and Re = 90 at $M_c = 0.1$.

Finally it is worthwhile noting that the phase response of the separation angle shows only a weak dependence on Reynolds number, but a relatively strong dependence on the Mach number. This can be seen by comparing the evolution of phase lag distributions between Figures 12 and 15. Furthermore, the time constants of the exponential fits were found to be numerically close in the case of the Reynolds number variation, but exhibited a definitive trend with Mach number, as shown in Figure 17.

To test the ability of the indicial method to predict the dynamic characteristics of the vorticity flux with oscillatory Reynolds number, a sample calculation was performed in the vicinity of the frequency which indicated theoretically (i.e. according to Equation (11)) a 150% amplification in fluctuating amplitude. As shown in Figure 18, the predicted behavior faithfully reproduced the results of the numerical simulation. The presence of an overshoot at the same frequency of k′ = 2.5 was previously noticed in Section 4 under the same nominal conditions of Mach and Reynolds number, but for totally different types of perturbations.

APPENDIX B

ANALYSIS OF A MODEL INDICIAL RESPONSE

Let $\xi(t)$ designate the indicial response of a function $\mu(t)$ in response to a perturbation ε, then, under the conditions outlined in Section 2, Equation (4) must hold:

$$\mu(t) = \xi(t)\varepsilon(0) - \int_{0}^{t} \xi(\tau)\frac{d}{d\tau}\,\varepsilon(t-\tau)\,d\tau \tag{16}$$

Let H designate the Heaviside step function. If the following form is assumed for the indicial response:

$$\xi(\tau) = \left[(1 - e^{-b\tau}) + \xi_{o}\right]H(\tau) \tag{17}$$

then Equation (17) is seen to represent a step function of magnitude ξ_o to which is superimposed an exponential relaxation function of unit amplitude. the ratio $(\xi_o/(1+\xi_o))$ therefore, measures the ratio of the initial value (or "spike", if $\xi_o < 0$) to the final value (i.e. after all transients have decayed).

Substituting Equation (17) into Equation (16) and assuming the perturbation ε to be of purely oscillatory form ($\varepsilon(t) = e^{iwt}$, $i^2 = -1$) yields for large times:

$$\mu(t) = e^{iwt}\left[1 + \xi_{o} - \frac{iw(b - iw)}{w^{2} + b^{2}}\right] \tag{18}$$

Hence the phase response ϕ is given by:

$$\phi = -\text{atan}\left|\frac{w}{b + c}\right| \tag{19}$$

where

$$c = \left(\frac{w^{2} + b^{2}}{b}\right)\xi_{o} \tag{20}$$

while the attenuation factor can be expressed as

$$\frac{A(w)}{A(0)} = \sqrt{1 + \left(\frac{1}{1 + \left(\frac{w}{b}\right)^{2}} - 1\right)\gamma} \tag{21}$$

where

$$\gamma = 1 - \left[\frac{\xi_o}{1 + \xi_o}\right]^2 \tag{22}$$

At finite frequency, Equation (21) becomes singular at $\xi_o = -1$. This situation arises when the final value of μ equals its amplitude immediately before the initiation of the step. This does not typically occur in practice. However, it is useful to examine the behavior of the amplitude (attenuation) response in the case where the indicial response is characterized by a large initial spike followed by a relaxation phase back to a value which is very close to the initial value. This type of indicial response was observed for the separation angle θ_s and the drag coefficient (Figures 7 and 9), and may be examined in detail by considering first order expansions of Equations (19) and (21) about $\xi_o = -1$.

Let $\xi_o = -1 + \delta$, where $|\delta| \ll 1$. It may be shown that

$$\frac{A(w)}{A(0)} \underset{\delta \to 0}{=} \frac{1}{\delta} \sqrt{1 - \frac{1}{1 + \left[\frac{w}{b}\right]^2}} \tag{23}$$

Hence, the shape of the amplitude response curve is given by the square root in (23), while at any given frequency, the response A(w)/A(0) gets amplified by a factor δ^{-1}, i.e. the magnitude of the spike of the indicial response, relative to the final value. This behavior is exemplified by the amplitude response curves associated with pressure and total drag (Figure 9).

A similar analysis of the phase response (Equation (19)) reveals that the phase asymptotes to -180° for large frequencies (a fact corroborated by the present results, Figure 10, top graph), and that the initial rate of change of the phase lag ϕ with respect to w is

$$\left.\frac{d\phi}{dw}\right|_{w=0} \xrightarrow[\delta \to 0]{} -\frac{1}{b\delta} \tag{24}$$

It can be shown that for δ fixed and $w \to 0$, then $\phi \to 0$. However, in the limit where $0 < w \ll 1$ is fixed and $\delta \to 0$, the phase asymptotes instead to a value of $-\pi/2$. Since δ is never zero in practice, it is the zero limit which is observed. Nevertheless, $\phi(w)$ may be viewed as the composite of two solutions which match at a frequency w^* such that $\phi(w^*) = -\pi/2$. Therefore w^* represents the frequency window of rapid adjustment of the phase between $\phi = 0$ and $\phi = -\pi/2$. The frequency w^* at which $\tan\phi$ becomes singular is given by the estimate

$$w^* \xrightarrow[\delta \to 0]{} b\sqrt{\delta} \tag{25}$$

Hence for a fixed relaxation constant b^{-1}, the width w^* of the region of rapid phase adjustment decreases like the square root of the spike amplitude.

A wealth of additional information can be extracted from such simple models as that expressed in Equation (17). In particular, the analysis can be easily extended to the case $\xi_o > 0$, corresponding to the initial transient of the vorticity flux indicial response (Figure 5).

The analysis of the model indicial response (17) with $\xi_o > 0$ did not yield the observed overshoot in the attenuation curve of the vorticity flux. Since such a model is unable to represent the local maximum exhibited by the indicial response itself, it is likely that this maximum is the cause of the overshoot. In any event, the sensitivity of the results to the magnitude ξ_o was found to be small for $\xi_o > 0$, but very significant for $\xi_o < 0$ (i.e. in the presence of an initial spike).

Since the magnitude of the initial spike appears to condition strongly the phase and amplitude responses for θ_s and C_D, an attempt at determining its scaling properties with respect to the step amplitude was performed. Using the perturbation technique described in Section 3, the Mach number was stepped up from an initial value $M_c = 0.25$ with various amplitudes covering five orders of magnitude, from $\Delta M/M_i = 0.001\%$ to $\Delta M/M_i = 100\%$. The results are presented on a logarithmic scale in Figure 19. In both graphs, the subscript i designates the initial value (i.e. immediately before the cylinder was set in motion). The round symbols represent the peak value of the indicial responses (at $t = 0^+$) while the square symbols correspond to the post-transient value ($t \to +\infty$). The solid curves are lines of unit slope which were added as an aid in determining the range of linearity of the data.

Both base and peak values for the indicial response of the total drag coefficient behave very linearly with forcing amplitude. Therefore, the ratio $(\xi_o/(1 + \xi_o))$ is a constant. Consequently, if the relaxation constant, b, is a constant, the phase and amplitude characteristics of C_D should be independent of Mach number change over the investigated range. This result is essentially in agreement with the data of Figure 10. In the case of the separation angle θ_s, an approximate linearity range exists below $\Delta M/M_i = 1\%$, followed by a saturation of the response. Therefore, it is expected that the phase and attenuation characteristics should exhibit a larger dependence on the initial perturbation magnitude, a fact also corroborated by the numerical experiments reported in this manuscript.

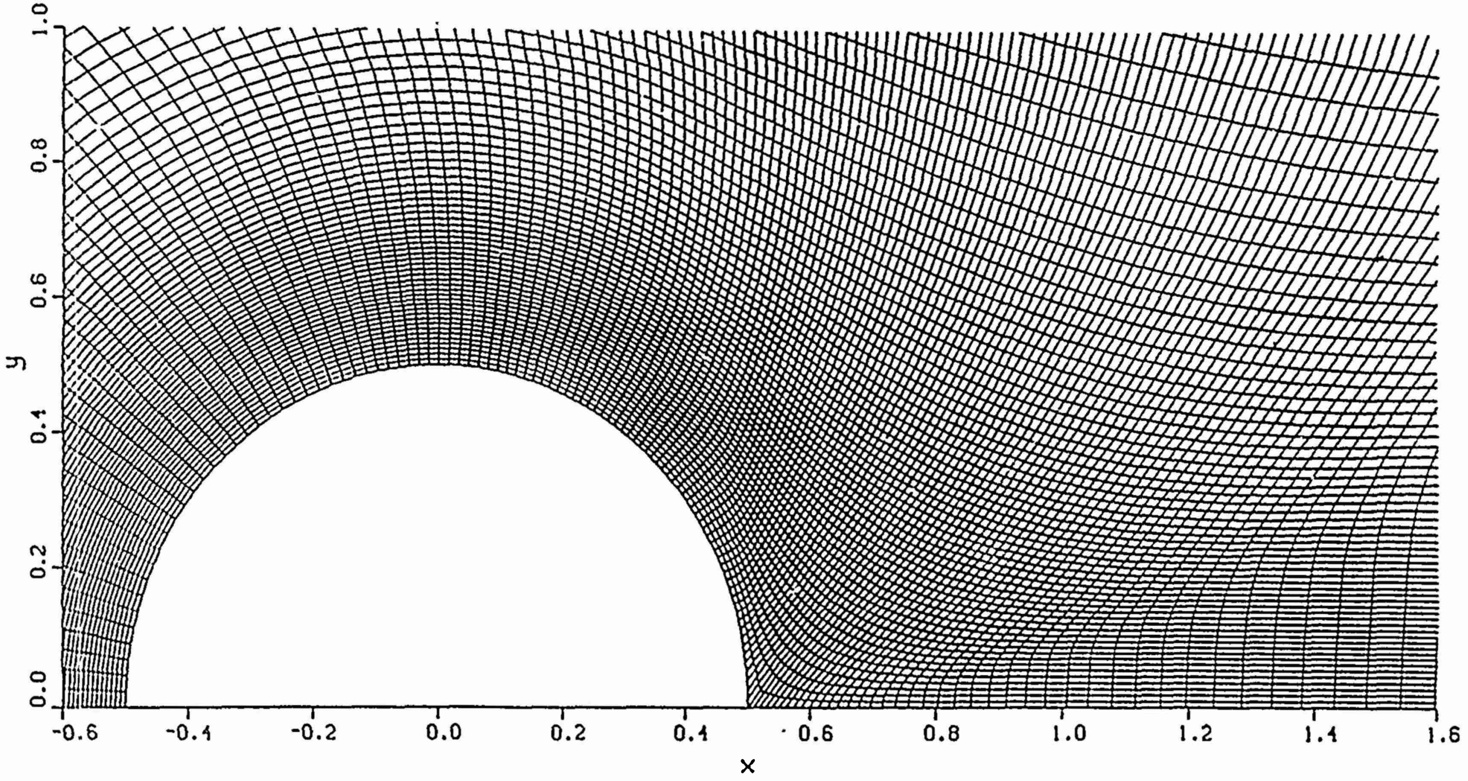

Fig. 1. Close-Up View of Two-Dimensional Grid Used for Navier Stokes Calculations of Unsteady Flow Around a Circular Cylinder.

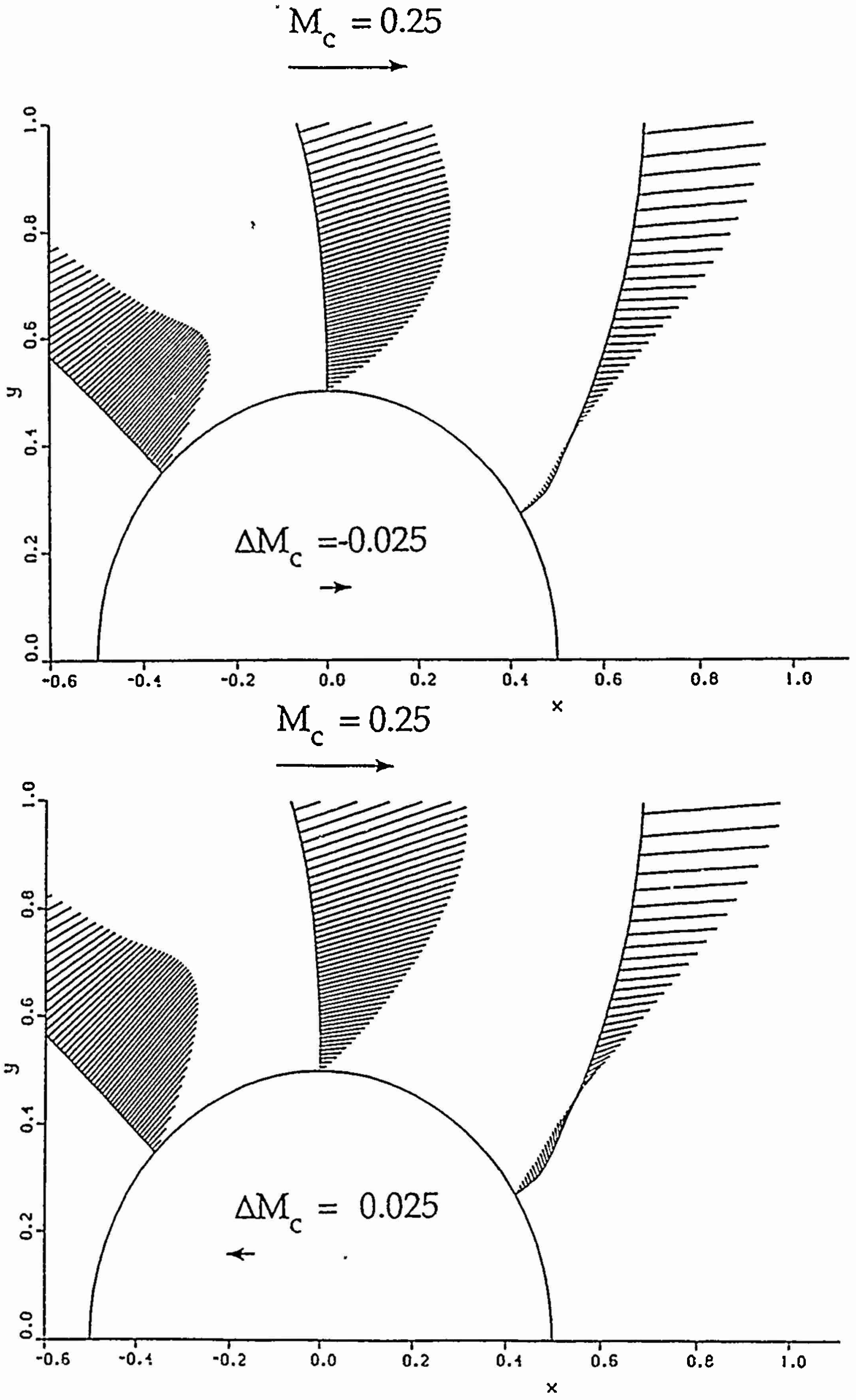

Fig. 2. Velocity Profiles Taken at $tU_c/D = 1.0$ After the Impulsive Start of the Cylinder, With (Top) and Against (Bottom) Freestream ($Re = 60$, $M_c = 0.25$).

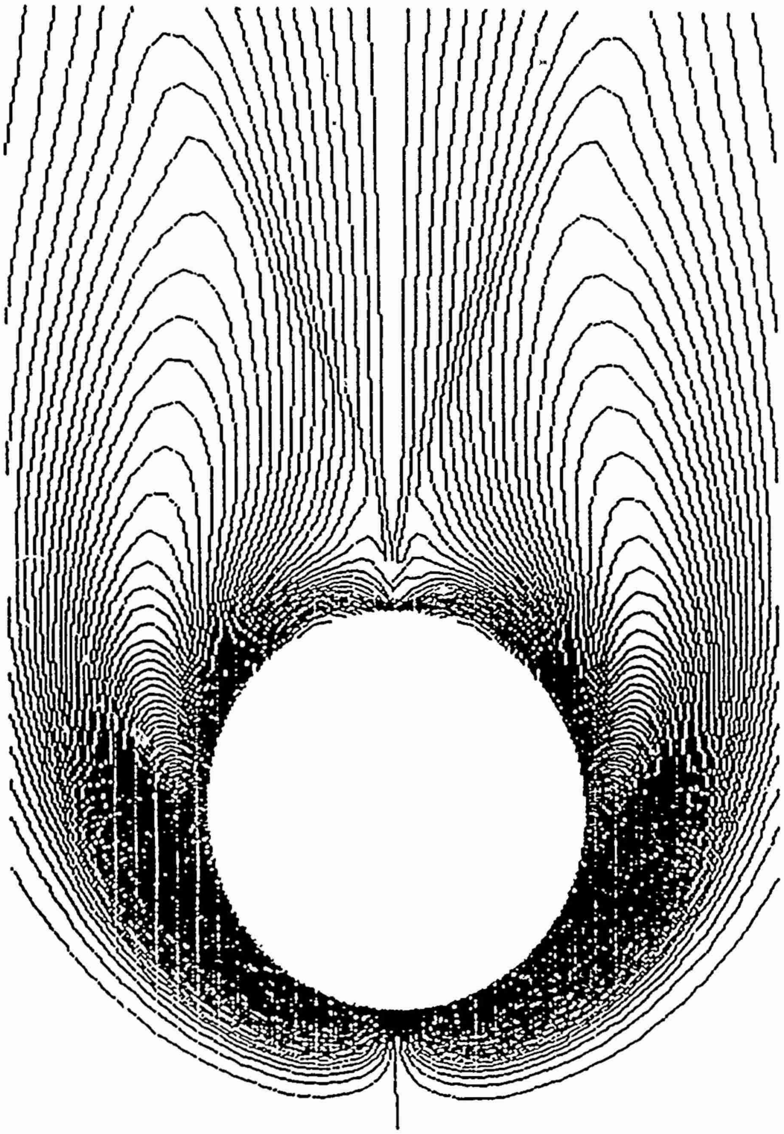

Fig. 3. Illustration of Vorticity Shedding in the Model Two-Dimensional Problem at $Re = 40, M_c = 0.1$.

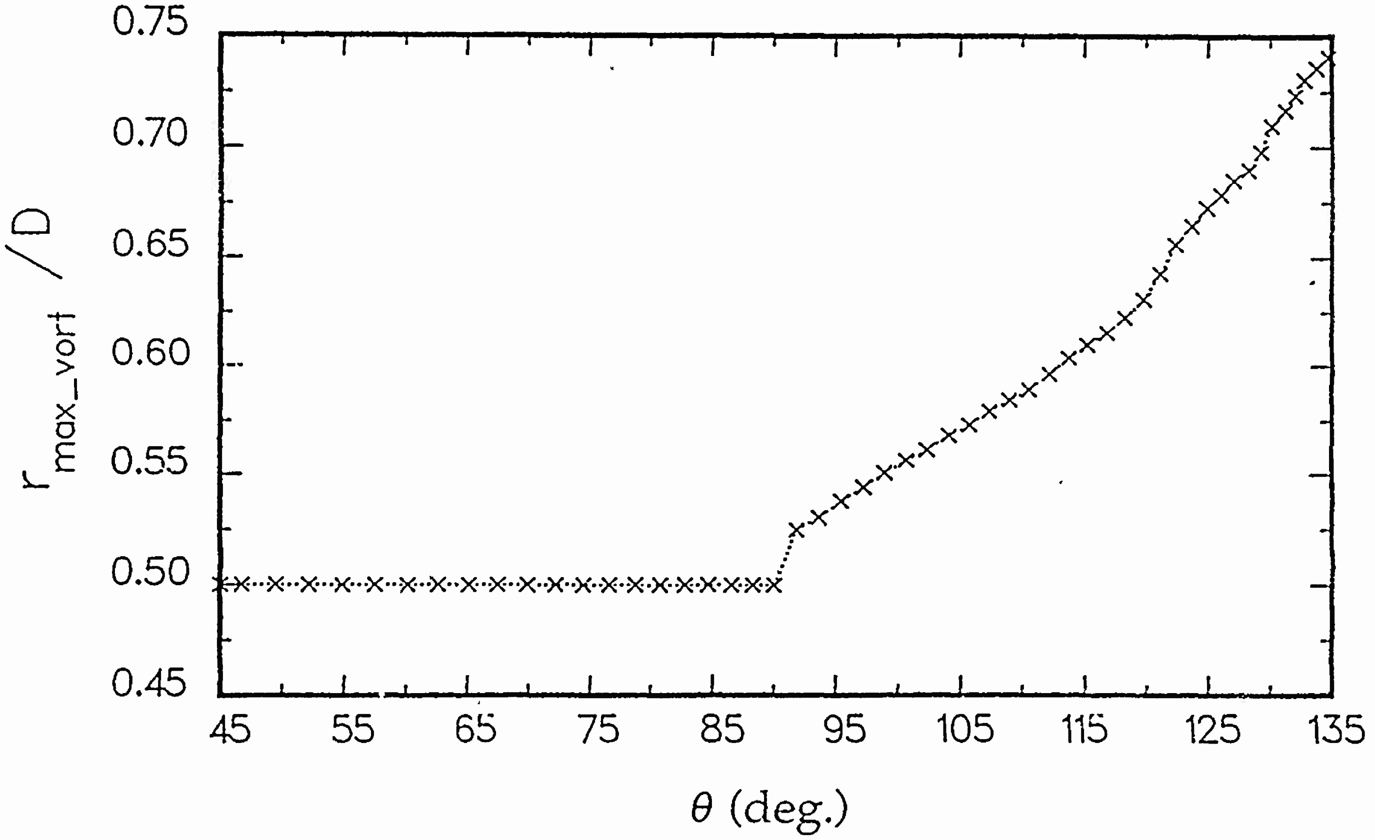

Fig. 4. Steady-State Radial Location of Vorticity Maximum as a Function of Roll Angle (Re = 36, M_c = 0.1).

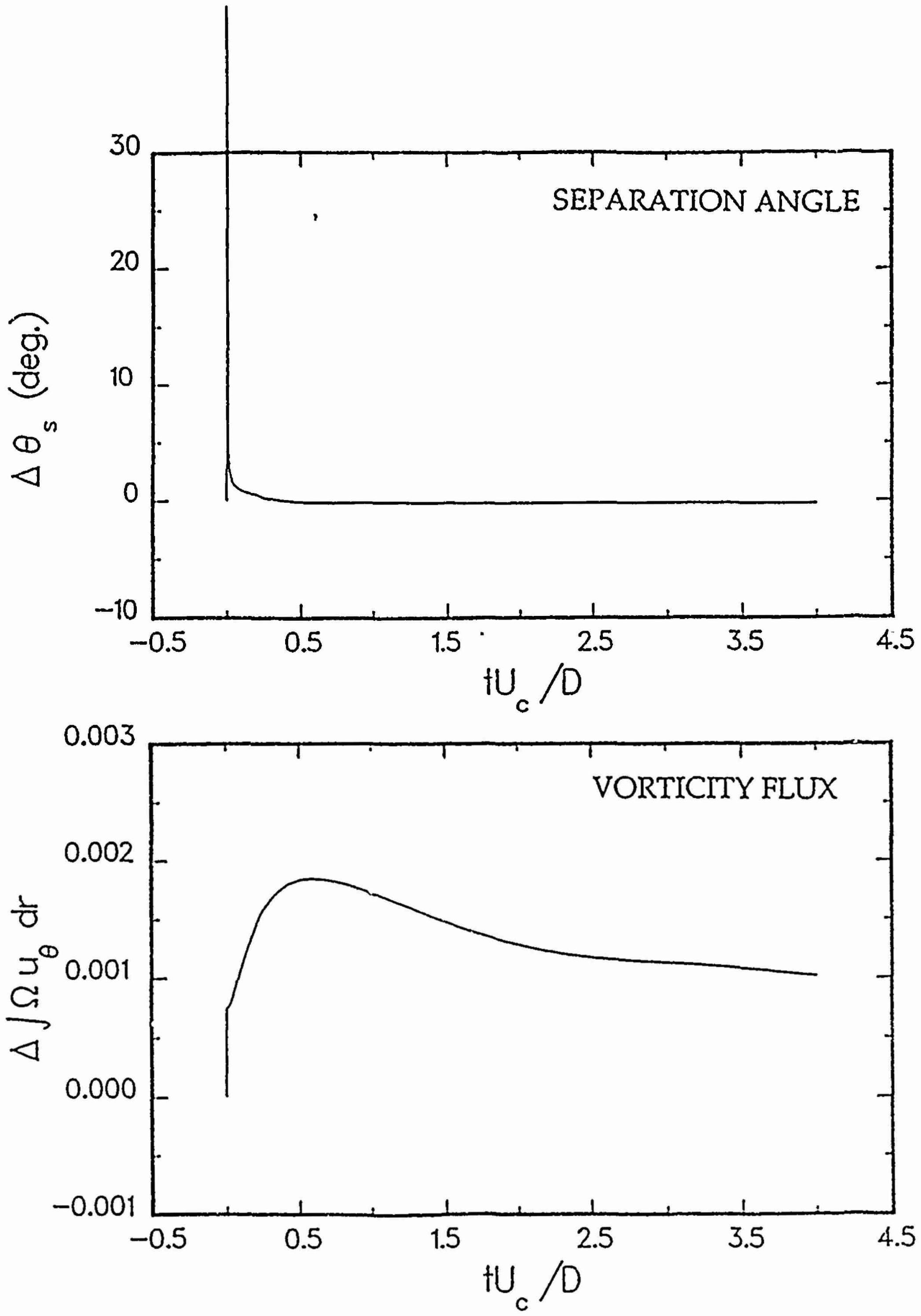

Fig. 5. Typical Indicial Responses for the Separation Point θ_s (Top) and the Vorticity Flux (Bottom), for Flow Around a Circular Cylinder Subjected to a 1% Change in Velocity ($M_c = 0.25$, Re = 60).

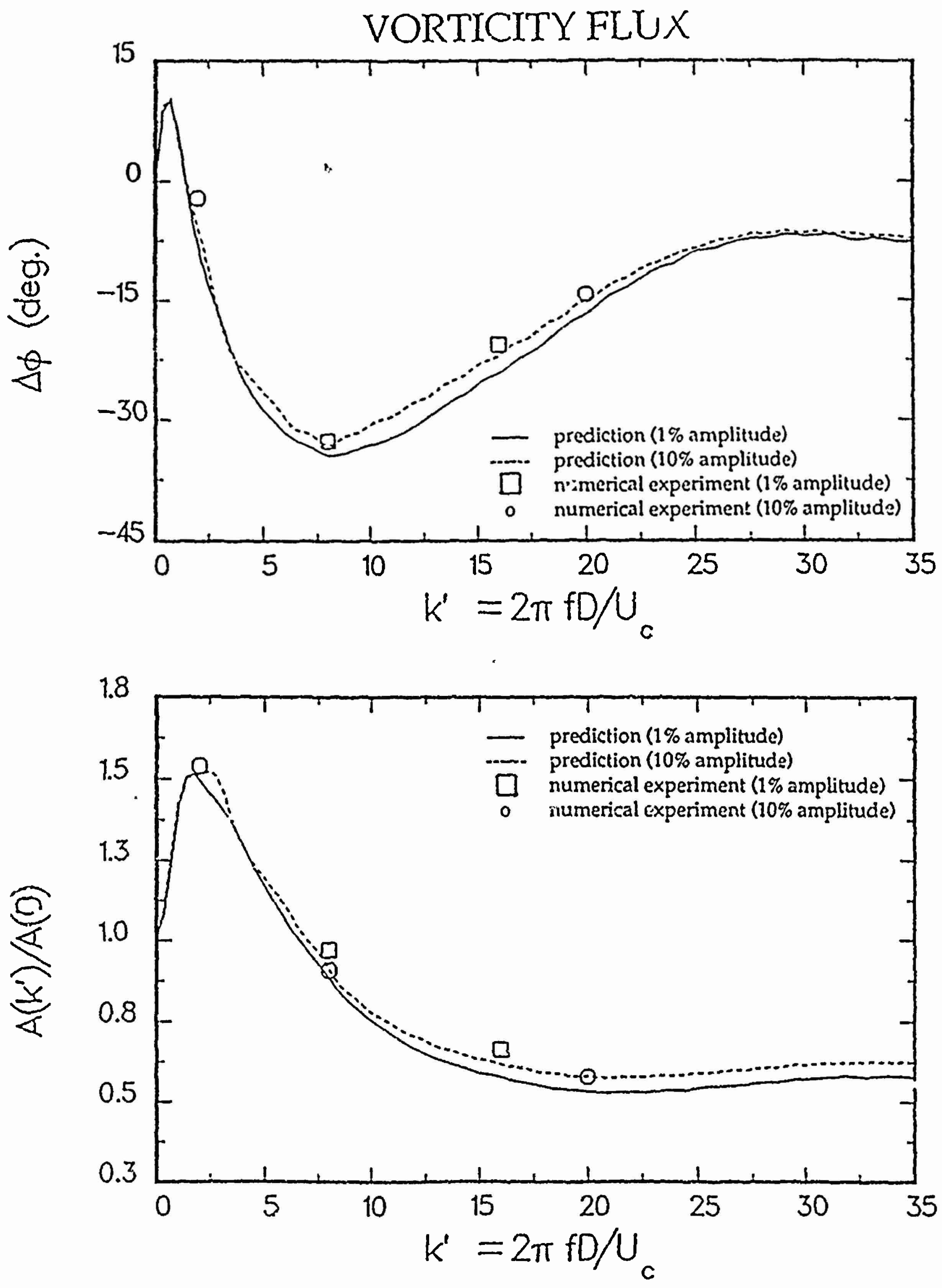

Fig. 6. Comparisons Between Theoretical Predictions (Based on the Indicial Responses) and Numerical Experiments for the Vorticity Flux. Top Graph: Phase Delays Bottom Graph: Amplitude Attenuation Factors. (M_c = 0.25, Re = 60).

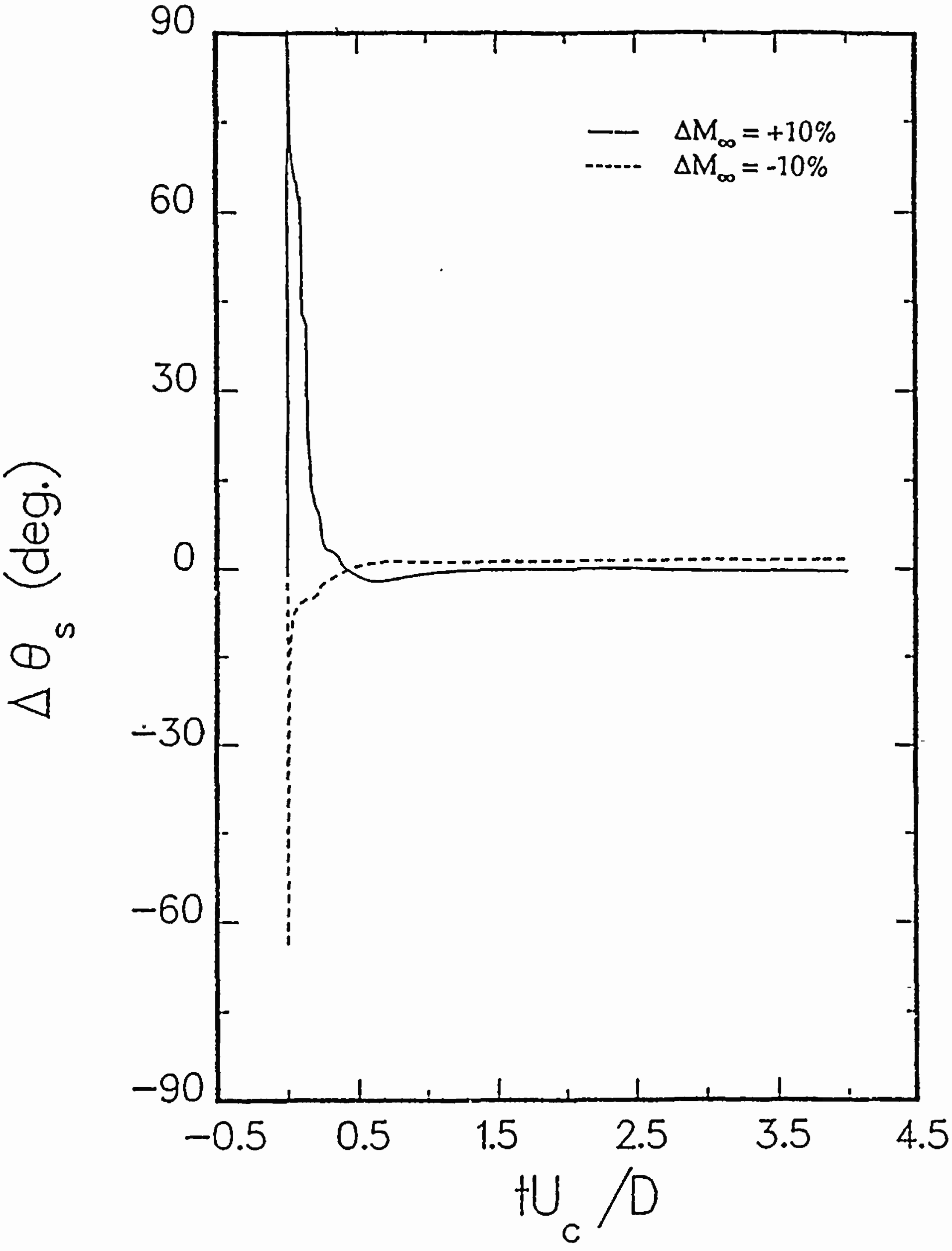

Fig. 7. Illustration of Asymmetrical Indicial Responses for the Separation Point when the Cylinder is Subjected to a Large Amplitude (10%) Step Change in Velocity ($M_c = 0.25$, Re = 60).

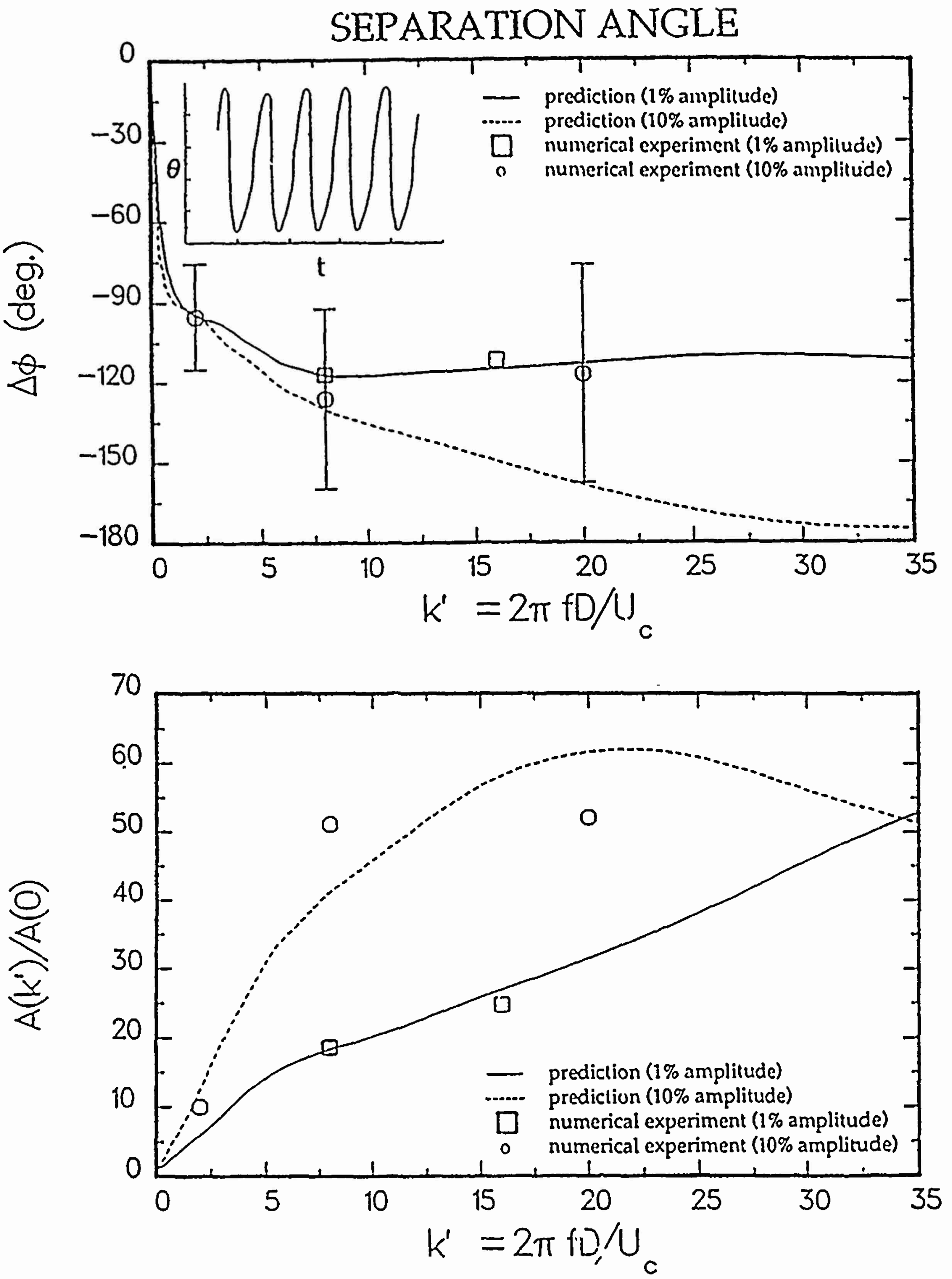

Fig. 8. Comparisons Between Theoretical Predictions (Based on the Indicial Responses) and Numerical Experiments for the Separation Angle. Top Graph: Phase Delays. Bottom Graph: Amplitude Attenuation Factors. (M_c = 0.25, Re = 60). The Inset Illustrates the Harmonic Distortion which Occurs when Positive and Negative Indicial Responses are Not Symmetric (From Direct Navier Stokes Simulation).

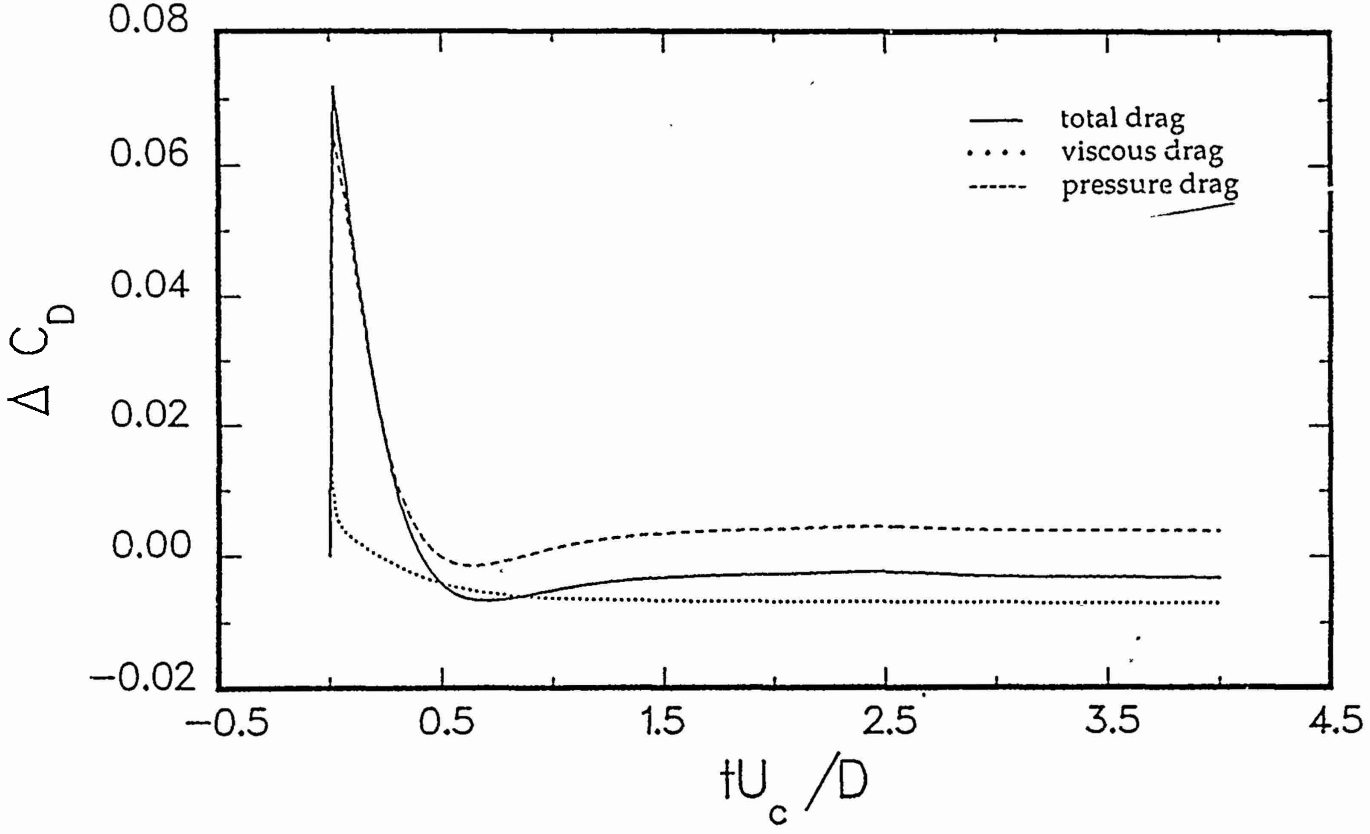

Fig. 9. Indicial Responses of Viscous, Pressure and Total Drag for a 1% Change in Velocity ($M_c = 0.25$, $Re = 60$).

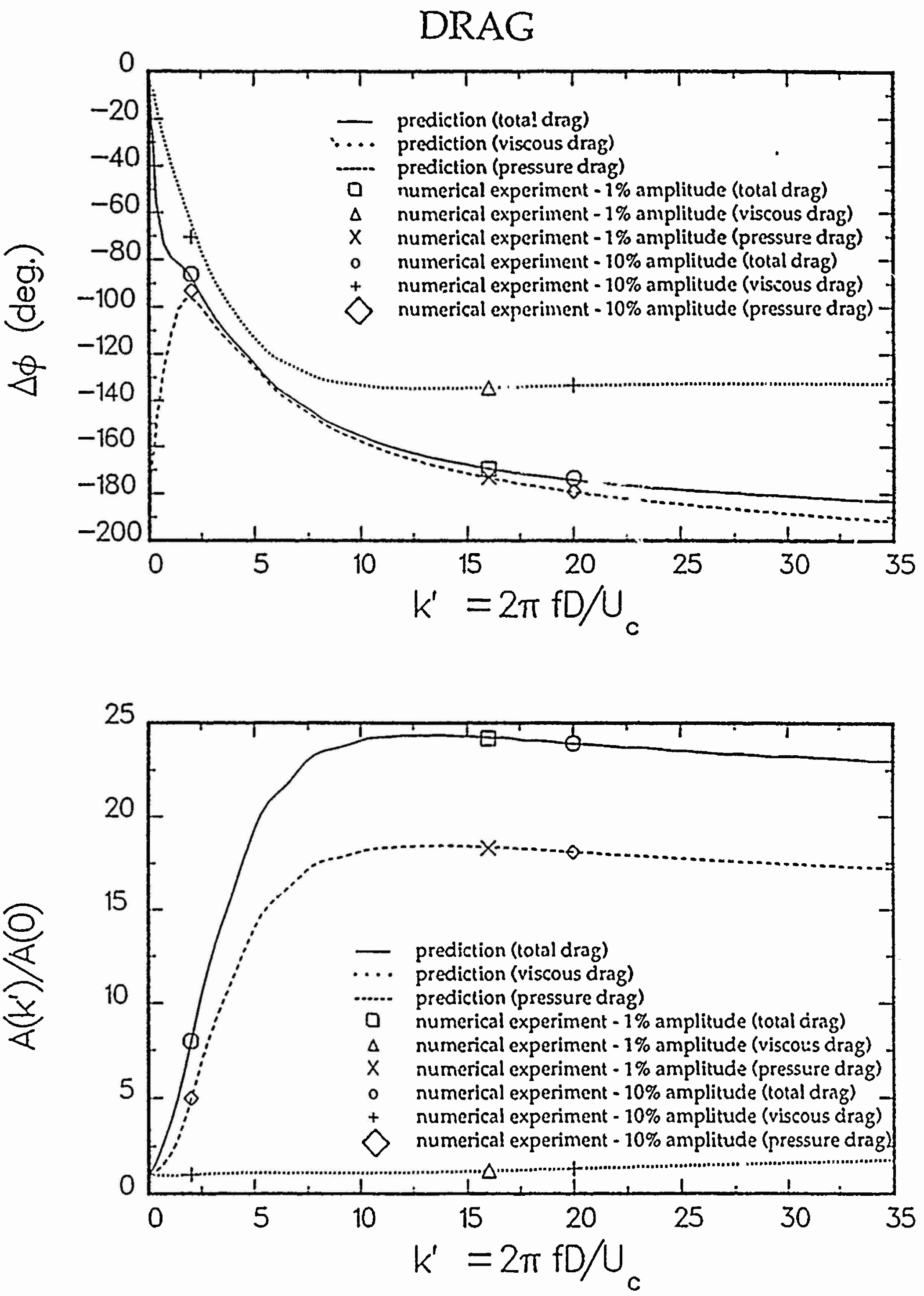

Fig. 10. Comparisons Between Theoretical Predictions (Based on the Indicial Responses) and Numerical Experiments for Viscous, Pressure, and Total Drag. Top Graph: Phase Delays. Bottom Graph: Amplitude Attenuation Factors. (M_c = 0.25, Re = 60).

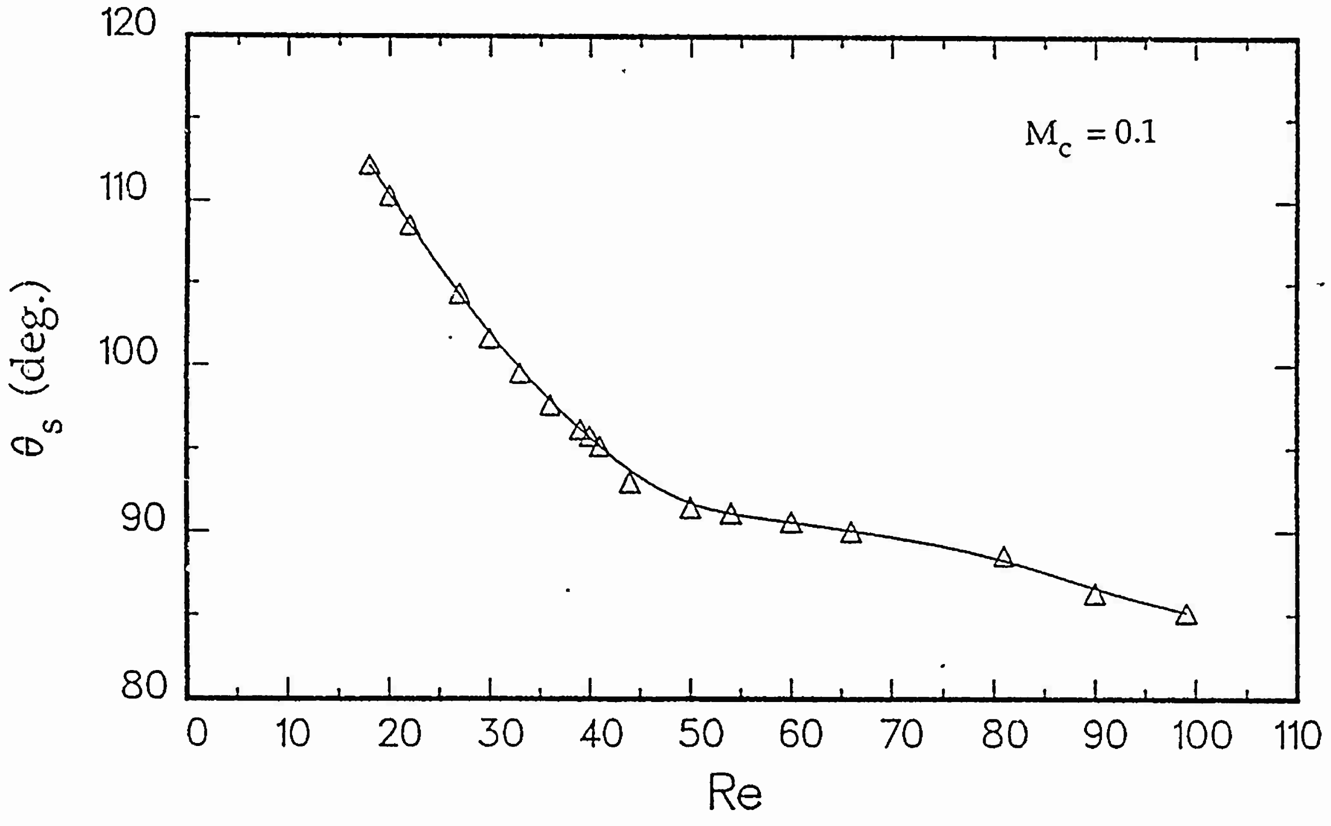

Fig. 11. Mapping of the Steady-State Separation Angle as a Function of Reynolds Number.

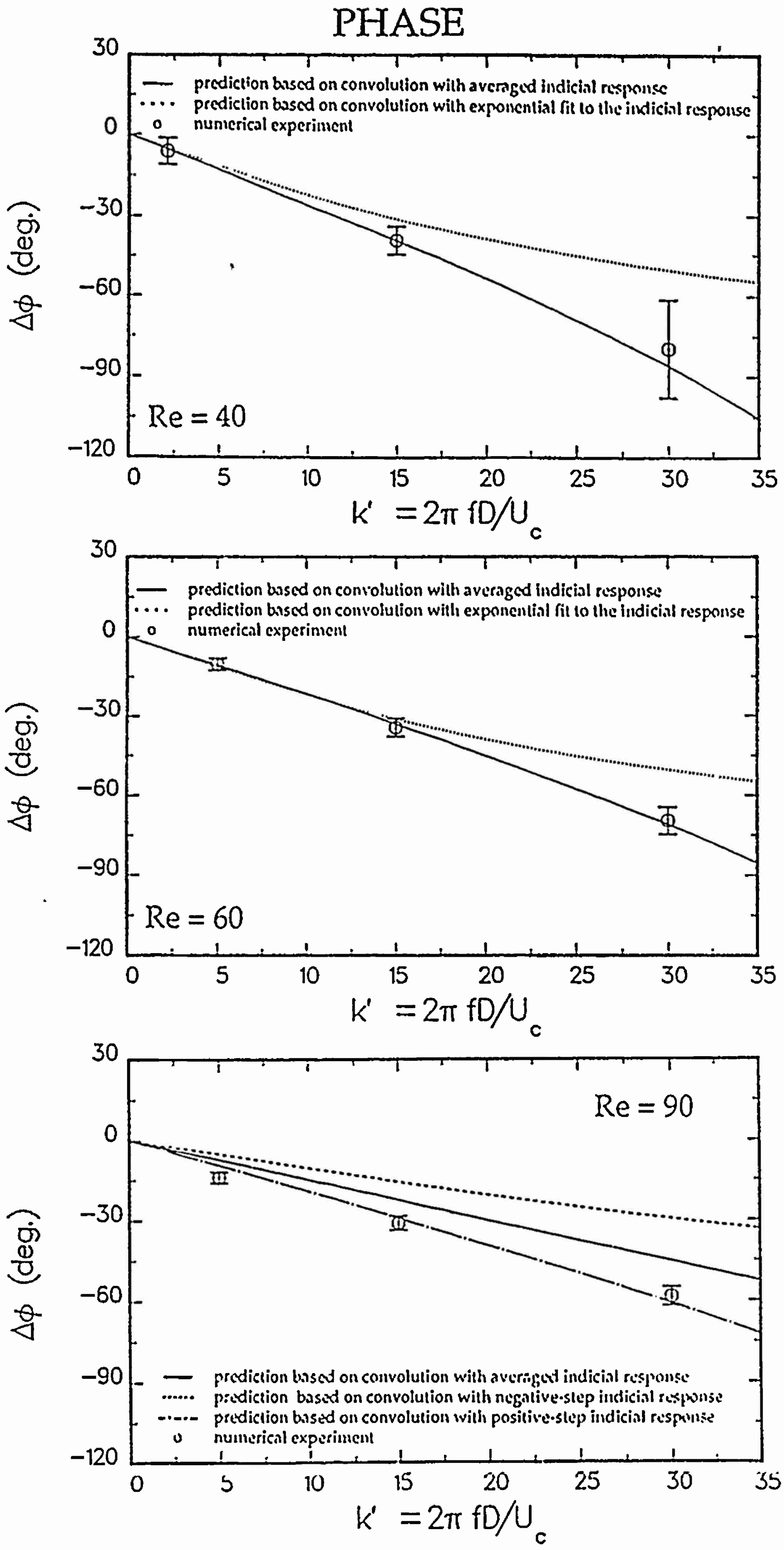

Fig. 12. Evolution of Prediction Accuracy of Phase Delays of θ_s with Reynolds Number, for a 10% Change in Reynolds Number at M_c = 0.1.

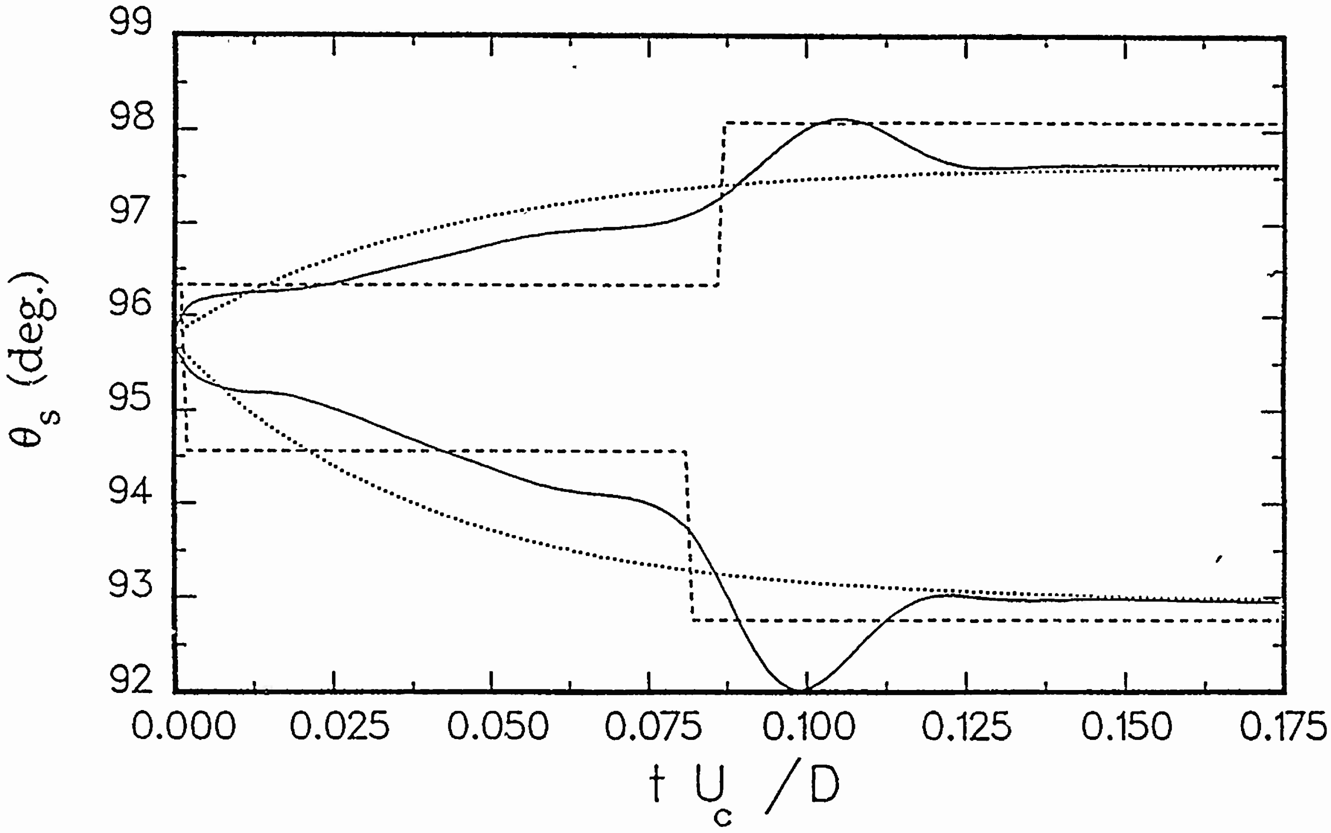

Fig. 13. Response of the Separation Angle θ_s to Negative and Positive Step Changes in Reynolds Number ($\Delta Re = \pm 4$ at $Re = 40$, $M_c = 0.1$), with Exponential Fits and Grid Resolution Indicator.

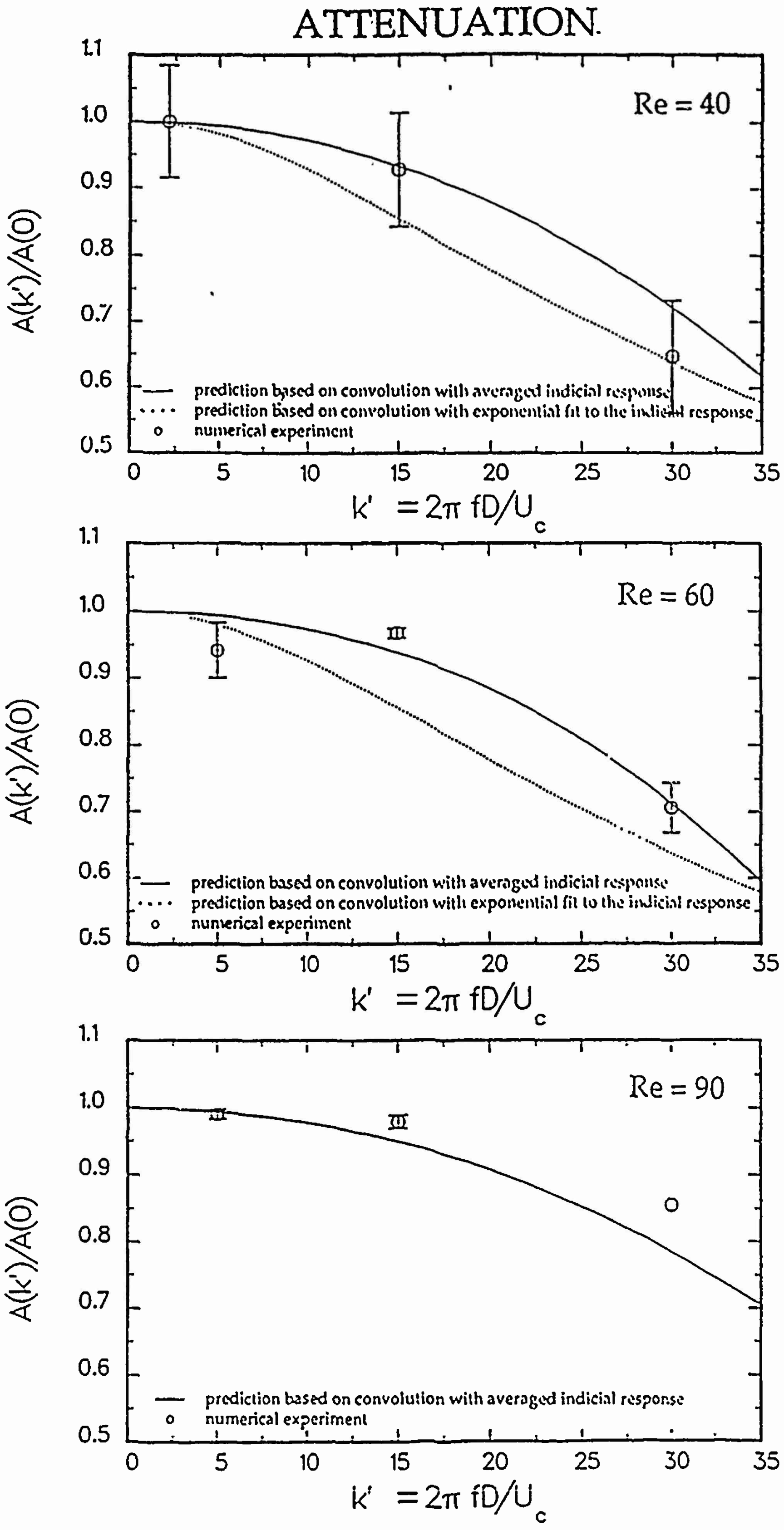

Fig. 14. Evolution of Prediction Accuracy of Attenuation Factors of θ_s with Reynolds Number, for a 10% Change in Reynolds Number at $M_c = 0.1$.

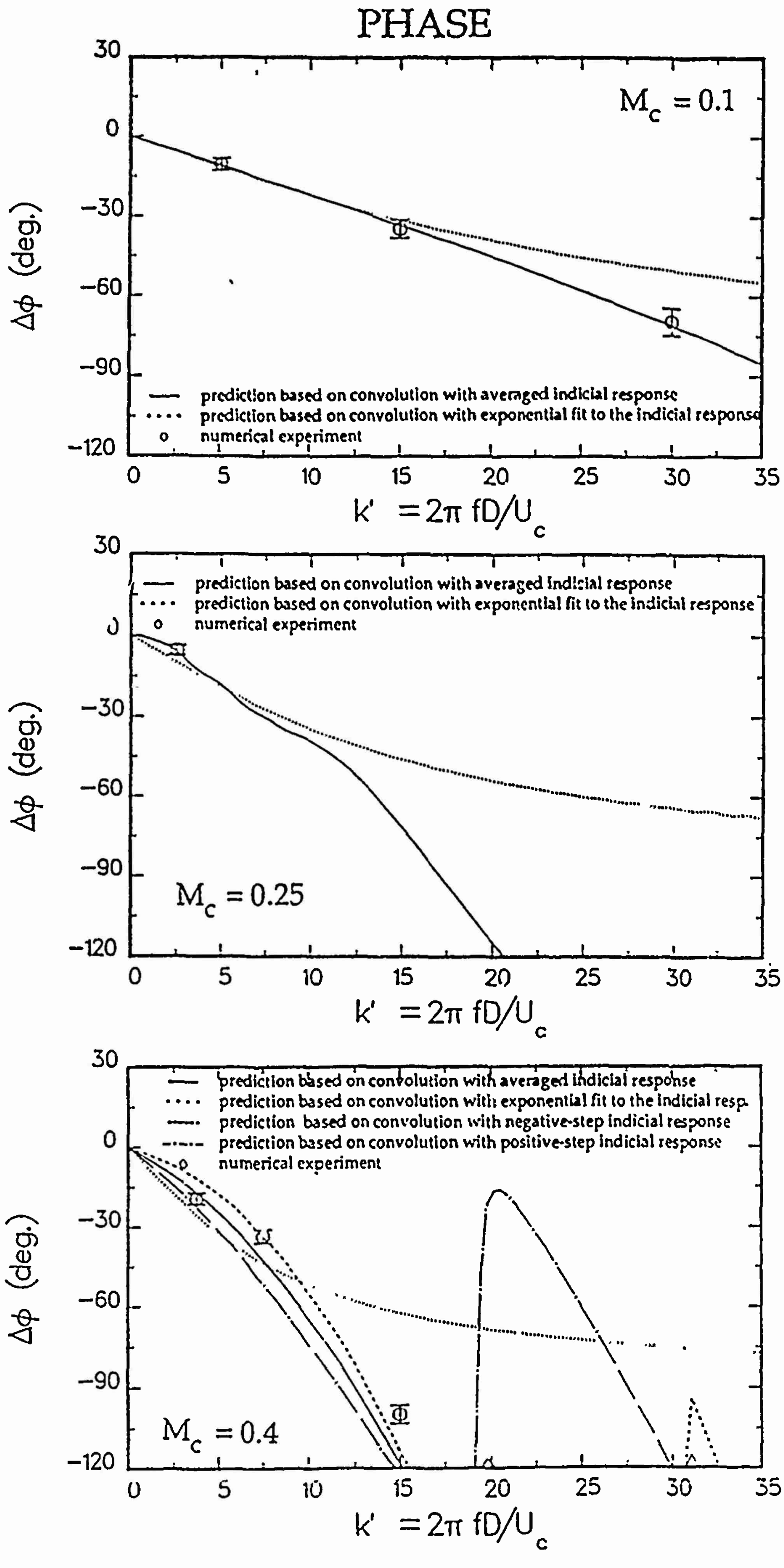

Fig. 15. Evolution of Prediction Accuracy of Phase Delays of θ_s with Cross-Flow Mach Number, for a 10% Change in Reynolds Number at Re = 60.

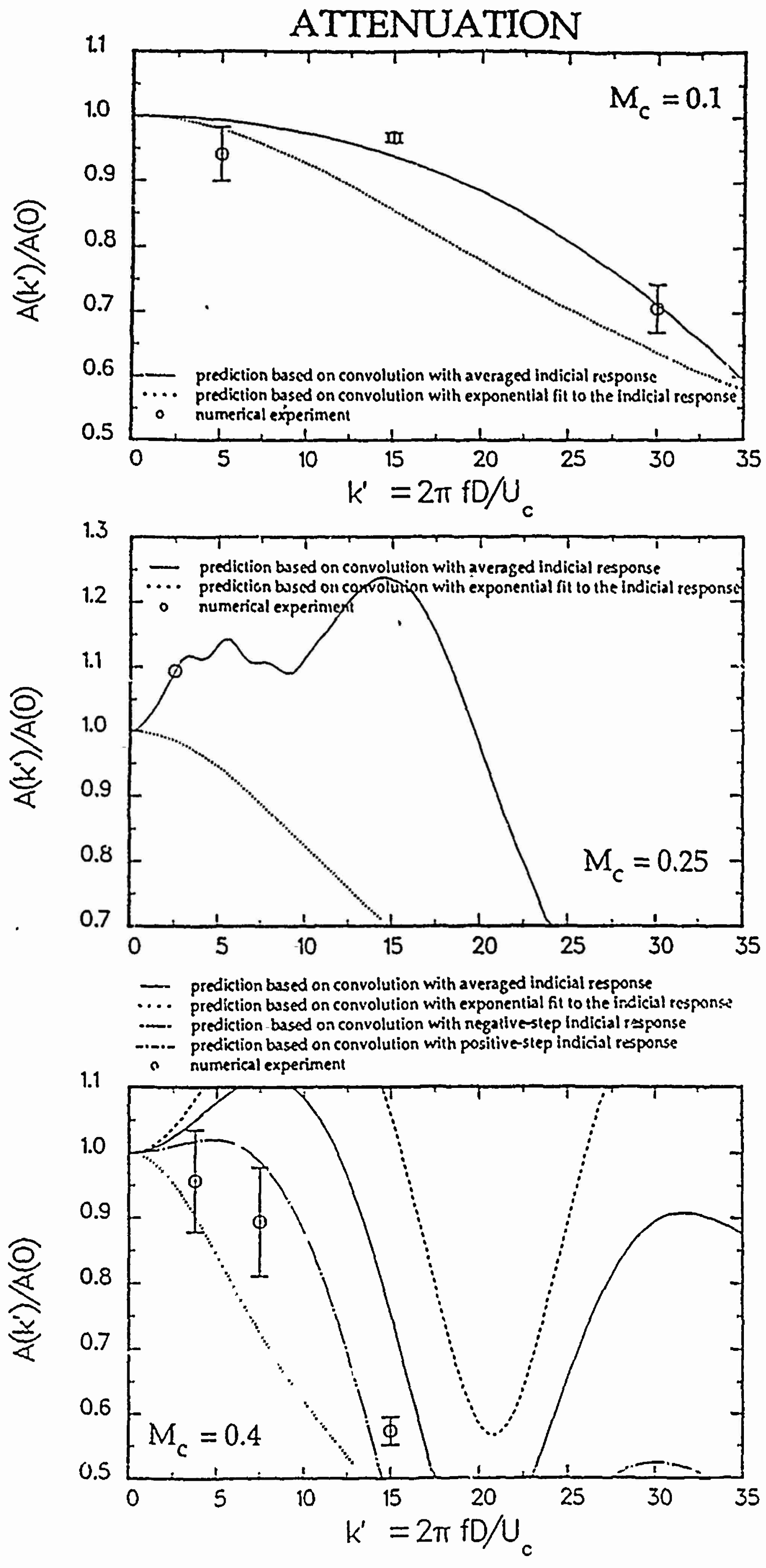

Fig. 16. Evolution of Prediction Accuracy of Attenuation Factors of θ_s with Cross-Flow Mach Number, for a 10% Change in Reynolds Number at Re = 60.

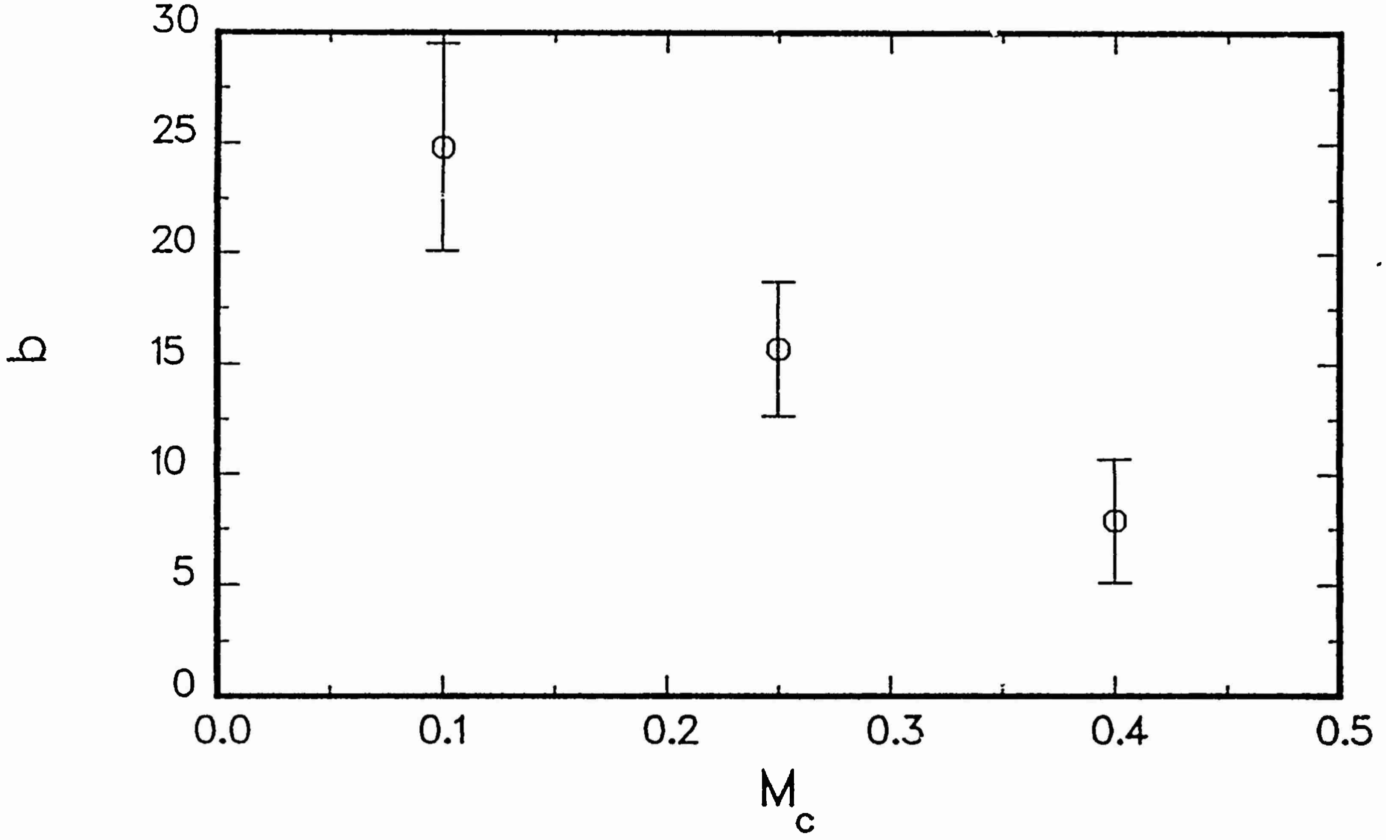

Fig. 17. Scaling with Mach Number of Inverse Time Constant of Indicial Response Exponential Fit (Re = 60).

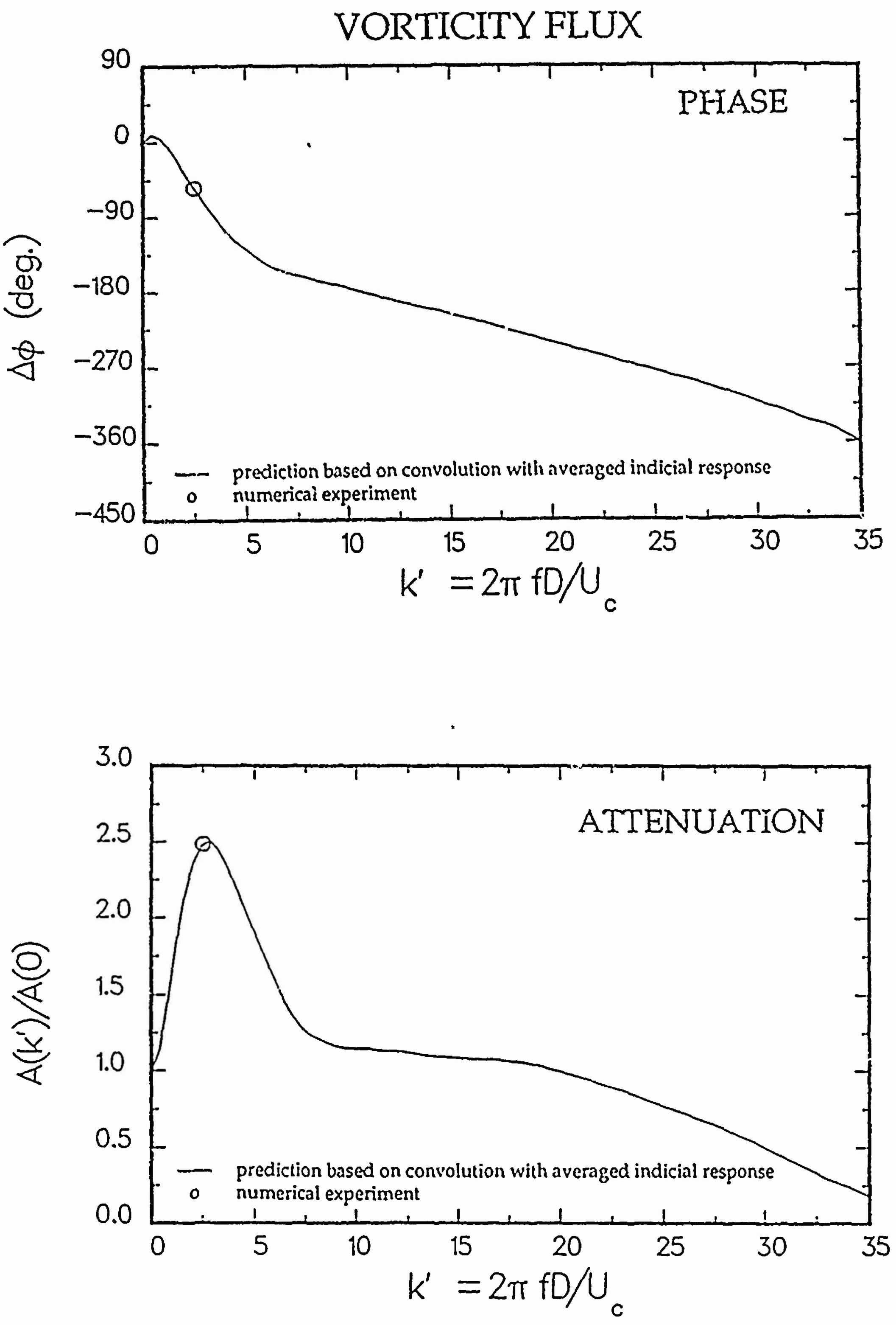

Fig. 18. Evaluation of Prediction Accuracy for the Vorticity Flux, for a 10% Change in Reynolds Number (M_c = 0.25, Re = 60).

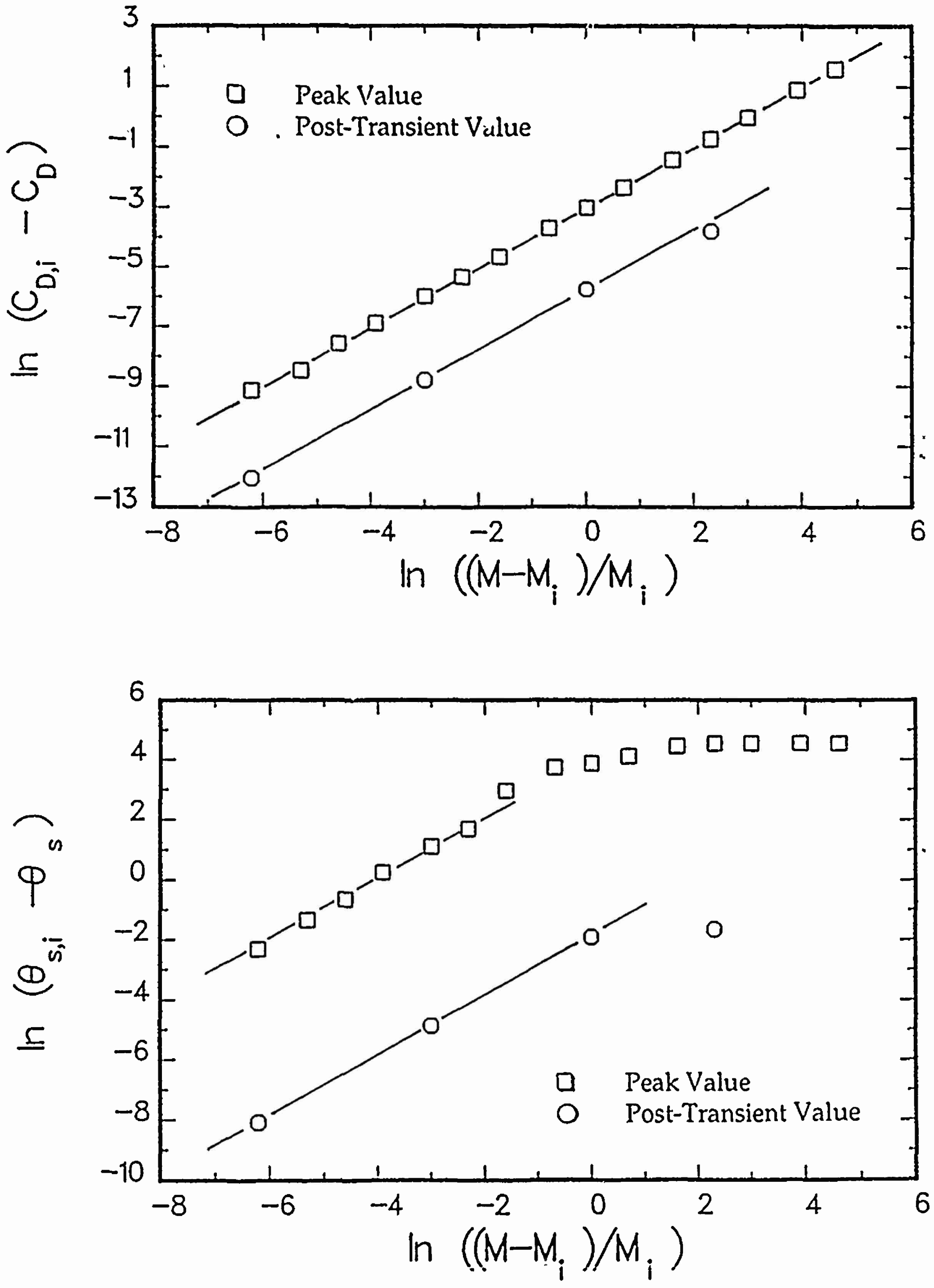

Fig. 19. Determination of the Linear Range, with respect to Mach Number Change, of Peak and Post-Transient Values of the Indicial Responses for: Total Drag (Top) and Separation Angle (Bottom), (M_c = 0.25, Re = 60).

AIAA 91-0601

Prediction of Unsteady Separated Transonic Flow Around Missile Configurations

P. H. Reisenthel and D. Nixon
Nielsen Engineering & Research, Inc.
Mountain View, CA

29th Aerospace Sciences Meeting

January 7-10, 1991/Reno, Nevada

PREDICTION OF UNSTEADY SEPARATED TRANSONIC FLOW AROUND MISSILE CONFIGURATIONS

P. Reisenthel[*] *and D. Nixon*[**]
Nielsen Engineering & Research, Inc.
Mountain View, California

Abstract

The Transonic Small Disturbance equation was supplemented with a transport equation for the streamwise vorticity and a vector potential equation to predict vortex effects over missile configurations. The flow separation phenomenon was modeled using normal vorticity jets placed along the separation line. The strength and location of the separating vorticity was determined from empirical criteria. Time-accurate calculations performed using a modified version of the CAP-TSD code in subsonic, transonic, and supersonic flow suggest that it is possible to compute realistic angle of attack configurations using CAP-TSD, thus showing considerable potential for aeroelastic applications and unsteady aerodynamics.

Nomenclature

Symbols:

A	Rotational vector potential
C_N	Normal force coefficient (based on body cross-sectional area)
Cp	Pressure coefficient
D	Body diameter
f	Frequency
Im()	Imaginary part
k	Angular reduced frequency based on length and freestream velocity $(2\pi fL/U_\infty)$
k'	Angular reduced frequency based on diameter and crossflow velocity $(2\pi fD/U_c)$
L	Body length
M	Mach number
p	Pressure
q	Total velocity $(u^2+v^2+w^2)^{1/2}$
s	Curvilinear coordinate along body radius
Re()	Real part
t	Time
u	Streamwise velocity
v	Spanwise velocity
w	Normal velocity
x	Streamwise coordinate
y	Spanwise coordinate
z	Normal coordinate
α	Angle of Attack
Γ	Circulation
θ	Roll angle
ϕ	Irrotational potential
ρ	Fluid density
Ω	Streamwise vorticity

Subscripts:

c	Crossflow
le	Leading edge
n	Normal
te	Trailing edge
∞	Freestream

1. Introduction

In recent years it has been possible to predict the unsteady transonic flow around a wing, especially those typical of commercial aircraft, in a fairly efficient manner. Frequently, the computer codes that are used are based on potential theory and are considerably faster than a corresponding calculation using the Euler equations. Because these methods have been developed for aircraft, they are not really applicable to missile flows where the effects of vorticity due to flow separation are important; the potential approximation cannot predict the effects of vorticity other than by representing a vortex wake by an infinitely thin sheet which is excluded from the computational domain. This model is complicated and may not be a viable option for routine calculations around real aircraft or missile configurations because the geometry of the vortex sheet can get quite complex.

For steady missile flow a variety of prediction methods are available,[1] ranging from panel methods with the addition of nonlinear vortex dynamics to the Euler equations or Navier-Stokes equations. It would be ideal to use the Navier-Stokes equations to model unsteady transonic flow around missiles, but there are several difficulties with this approach. The most obvious difficulty is the computer time required, which is several orders of magnitude greater than that required for a potential calculation. Even if a dedicated supercomputer were available for such calculations, the computation of the necessary flow separation might be inaccurate because of the inherent inaccuracy in many present turbulence models. The next best approach would be to use the time dependent Euler equations which require some empiricism to initiate separation and compute the shed vorticity. If the separation line and shed vorticity could be predicted, then the Euler equations would be a viable model since they will model the transport of this vorticity reasonably accurately. However, since missiles are slender some further approximations can be made.

This paper is concerned with developing a method of predicting the unsteady pressure distribution on missile-like bodies at transonic and supersonic speeds. The concepts developed in this work are extensions of earlier analyses[2,3] for steady and unsteady flow. The approach is to make as much use of the existing technology as possible. The final goal is a computer code capable of predicting the effects of three-dimensional unsteady separation in transonic flow about missiles for use in aeroelastic calculations or during maneuver. One important aspect of this work involves the application of indicial theory to predict the time-dependent behavior of boundary layer separation. The present paper is an account of the final phase of the work, namely the refinement and exploitation of the unsteady flow variant of this method for prediction of three-dimensional unsteady separated flow.

---

[*] Research Scientist, Member AIAA
[**] President

2. Basic Equations

The present approach is based on experience gained in steady subsonic and supersonic flow predictions for missiles, in particular, the fact that if a separation line and the strength of the vorticity introduced at that line can be estimated empirically, the governing equations (such as the Euler equations) will represent the transport of this vorticity accurately. Because the computational time for the Euler equations for an unsteady calculation is considerably greater than that for a potential calculation, a simplified model is used.

The basic equations are an extension of those derived by Klopfer and Nixon[4] for steady flow and constitute a subset of the Euler equations. For slender bodies, the five Euler equations are reduced to an equation similar to the three-dimensional unsteady potential equation, a three-dimensional vorticity transport equation, and a two-dimensional Poisson equation. In addition to having to solve a reduced set of equations, a significant advantage is that one of the equations is almost identical to the potential equation for which there are well tested computer codes. This allows the development of a prediction method based considerably on proved technology. The reader is referred to Ref. 3 for the derivation of these equations, as well as a description of their numerical implementation.

The basic equations are summarized as follows:

Vorticity Transport

$$\Omega_t + \Omega_x + (v\Omega)_y + (w\Omega)_z = 0 \qquad (1)$$

Rotational Crossflow

$$A_{yy} + A_{zz} = -\Omega \qquad (2)$$

Mass Conservation

$$\rho_t + (\rho u)_x + (\rho v)_y + (\rho w)_z = 0 \qquad (3)$$

where ρ is the fluid density, u, v, and w designate the streamwise, spanwise, and normal velocity components (i.e., in the coordinate directions x, y and z, respectively), and A is the vector potential for the rotational velocity. The Helmholz decomposition of the flowfield into potential and rotational components is given by:

$$u = 1 + \phi_x \,;\, v = \phi_y + A_z \,;\, w = \phi_z - A_y \qquad (4)$$

where ϕ is the irrotational scalar potential. Finally, the density is related to the velocity components through the isentropic ideal gas relation:

$$\rho = \rho_\infty \left\{ 1 + \frac{(\gamma-1)M_\infty^2}{2}(1 - 2\phi_t - u^2 - v^2 - w^2) \right\}^{\frac{1}{\gamma-1}} \qquad (5)$$

where M_∞ designates the freestream Mach number, and γ is the specific heat ratio.

The boundary conditions on the body are zero flow through the body, and zero vorticity flux, except at the specified separation line.

3. Computer Code and Numerical Methods

By making the small disturbance approximation, ρ can be expanded in terms of disturbance velocities, and substituted into the conservation of mass equation to give the following three-dimensional unsteady potential equation:

$$\frac{\partial f_0}{\partial t} + \frac{\partial f_1}{\partial x} + \frac{\partial f_2}{\partial y} + \frac{\partial f_3}{\partial z} = 0 \qquad (6)$$

with

$$\left.\begin{aligned} f_0 &= -M_\infty^2\phi_t - 2M_\infty^2\phi_x \\ f_1 &= (1-M_\infty^2)\phi_x - \tfrac{1}{2}(\gamma+1)M_\infty^2\phi_x^2 + \tfrac{1}{2}(\gamma-3)M_\infty^2(\phi_y+A_z)^2 \\ f_2 &= \phi_y + A_z - (\gamma-1)M_\infty^2\phi_x(\phi_y + A_z) \\ f_3 &= \phi_z - A_y \end{aligned}\right\} \qquad (7)$$

In Ref. 3, Nixon et al. showed that because of the resemblance between Eq. 6 and the usual Transonic Small Disturbance (TSD) equation, this theory could be implemented using established and well-tested potential flow solvers, such as the Computational Aeroelasticity Program CAP-TSD, due to Batina et al.[5] The CAP-TSD code is capable of predicting the unsteady transonic and supersonic flow over a complete aircraft configuration including fins, stores, and pylons. Consequently, this code was used as a basis for the implementation of the above-mentioned unsteady flow theory (an implementation of the steady version of this theory may be found in Ref. 4).

The present paper reports sample calculations for a model three-dimensional slender body with horizontal and vertical fins. The results illustrate the predictive capability of a computational tool initially based on CAP-TSD, but which has extended the range of applications of this code to separated vortical flows, including crucial refinements in the representation of the computational fuselage.

The algorithm used in CAP-TSD is approximate factorization with time stepping as an option; this algorithm is retained in solving Equation (6) and the vorticity transport equation, Equation (1). Since Equation (2) does not have explicit time-dependence, it can be solved at each time step and in each individual streamwise plane by using the successive over-relaxation method. The time-marching procedure is performed using a second order accurate implicit scheme. For the continuity and vorticity transport equations, if the Newton iteration option is used, then the L_2-norm over space of the incremental change in the solution ($\Delta\phi$ or $\Delta\Omega$) approaches zero at each time step, and the solution is time-accurate. For the vector potential equation, the solution is also time-accurate, since at each iteration, ΔA can be made arbitrarily close to zero. A more complete description of the algorithm and the difference equations which have been used to modify the CAP-TSD code can be found in Ref. 3.

4. Boundary Conditions

a) *Body*. At the body, the flow is required to be tangential to the surface, and a normal vorticity jet is prescribed at the point of flow separation.

In CAP-TSD, the fuselage cross-section is assumed to be elliptic, and the boundary conditions on the body surface are *transferred* to a bounding cartesian grid (the computational fuselage) by using ideas from slender body theory. For angles of attack typical of missile flight, however, the original treatment was inadequate and an alternative scheme was developed.[3] In this modified scheme, the assumption of slender body flow is still used, in particular, the consequence that only the crossflow is important. The boundary conditions on the cartesian computational boundary are found from the 'thickness effect,' which is relatively accurate, and by using an analytic solution for the crossflow to specify normal velocities v or w on the computational boundary. For a body at angle of attack α these conditions, in a reference frame aligned with the freestream, are expressed as:

$$\phi_y + A_z = v \; ; \; \phi_z - A_y = w - \sin(\alpha) \tag{8}$$

Since the standard form[3] of the TSD Equation (i.e., in the absence of swept shocks) reduces to Laplace's equation in the crossflow plane, it is justified to use analytic solutions v and w obtained from conformal mapping transformations. Such an approach has been previously shown[3] to be valid for reduced frequencies, $2\pi fL/U_\infty$, up to order unity, within the context of slender body approximation and negligible compressibility effects (of order α^2) in the crossflow.

For a body with elliptical cross-section and thin lifting surfaces aligned with the principal axes of the ellipse, this analytic solution is obtained by using successive conformal mapping transformations. The global transformation (noted $\sigma = \chi(Z)$, with $Z = -z + iy$) maps the symmetry plane ($y = 0$), the elliptical boundary, and the horizontal and vertical fins into a subset of the real axis in the σ-plane. The transformation is the composite of the following mappings:

i) ellipse of semi-axes b and a into the unit circle:

$$\xi = \frac{Z + (Z^2 - a^2 + b^2)^{1/2}}{a+b} \tag{9}$$

ii) unit circle into a flat plate:

$$\eta = \xi + \frac{1}{\xi}$$

iii) flat plate with vertical fence of height η_e into a flat plate:

$$\sigma = \left[\left[\frac{\eta}{\eta_e}\right]^2 + 1\right]^{1/2} \tag{11}$$

In the σ-plane, the flow is that associated with a point vortex in a crossflow (see Nixon et al.[3]). The freestream velocity magnitude in σ-space is $(a+b)\eta_e\sin(\alpha)/2$. The point vortex used in each streamwise plane models the rotational component of the flowfield by being given a strength Γ_o equal to the numerically integrated vorticity in that plane. The location of the vortex in Z-space is chosen to be the centroid of vorticity.[*]

Let F be the complex potential associated with the analytic solution in the transformed plane; the spanwise and normal velocities v and w can then be recovered according to:

$$V = \operatorname{Im}\left\{-\frac{dF}{d\sigma}\frac{d\chi}{dZ}\right\} \tag{12}$$

and

$$W = -\operatorname{Re}\left\{\frac{dF}{d\sigma}\frac{d\chi}{dZ}\right\} \tag{13}$$

If A is a constant along the boundary, then Equations 8 are used to supply CAP-TSD with the required Neumann boundary conditions on ϕ. The inclusion of the $\sin(\alpha)$ term in Equation 8 reflects the fact that the equations of motion are solved in a reference frame attached to the body, i.e., at an angle of attack α from the freestream.

In the original CAP-TSD code, the computational fuselage is a *rectangular* cylinder which encompasses the entire body. Such a configuration was used in computations by Nixon et al.,[3] for a body with a 2:1 elliptical cross-section. For such bodies, the separation line lies close to the 90° roll angle, and the shear layers are known to separate almost vertically. There are, however, several problems with this representation of the fuselage, in particular, the fact that the exact location of the vorticity jet cannot be determined accurately, since one must account for the transport of vorticity within the space bounded by the true and computational body surfaces. Furthermore, the vorticity distribution at a far away boundary cannot be represented by a single outward vorticity jet at some location on that boundary. This problem becomes especially acute with low aspect ratio ellipses, and in particular in the case of *circular* cross-sections.

The difficulty was circumvented by modifying the CAP-TSD code so as to represent the computational fuselage by a serrated-edged cylinder which closely approximates the actual solid boundary. The obvious advantages of this modification are: *i)* an accurate calculation of the vorticity transport phenomenon close to the separation point; *ii)* a lesser dependence on the model used for the transfer of boundary conditions (Equations 12 and 13); and *iii)* convergence of the true and computational surfaces towards one another, with increasing grid resolution in the crossflow plane. Most importantly, this representation of the computational fuselage can retain the cartesian grid of the CAP-TSD code. The resulting grid is shown in Fig. 1, where the cross-section of the actual body has been outlined. The

---

[*] In the two-dimensional point vortex model, it is necessary to consider the existence of a 'feeding sheet' along the branch cut because $\partial\Gamma/\partial t \neq 0$. This is because the variable circulation results in a $\partial\phi/\partial t$ term in the Bernouilli equation, hence producing a pressure jump across the branch cut. The resulting force must be balanced by the Joukowski force on the vortex core.[19] This 'force-free' (but not moment-free) vortex condition leads to an O.D.E. for the vortex position and circulation[20] as a function of time, for given initial conditions. Since Γ is known such an approach would essentially amount to a duplication of the vorticity transport equation. Therefore, the simple centroid model was retained in the present boundary conditions.

arrow in the close-up figure indicates the roll angle convention.

For the vorticity boundary condition at the body, a flow separation condition is simulated by the injection of vorticity into the flowfield at the point of separation. For steady flow, a modified version of the Stratford criterion[6] is used to determine the separation line:

$$C_p'\left(s\frac{dC_p'}{ds}\right)^{1/2}\left[Re_s \times 10^{-6}\right]^{0.1} = 0.35 \sin(\alpha) \tag{14}$$

where Cp' is the modified pressure coefficient[7] and s is the virtual length of the turbulent boundary layer, as seen in the crossflow plane.

Although two-dimensional Navier-Stokes calculations of unsteady flow around a circular cylinder have been performed[8] as a first step towards the goal of formulating a truly dynamic version of the Stratford criterion, the results presented in this manuscript are mostly limited to its quasi-steady implementation. Typical separation lines obtained in this manner are provided in Fig. 2. For the body geometry described in Section 6, this figure shows the temporal variations of the computed separation line (i.e., the separation roll angle θ_s measured from the windward stagnation point as a function of streamwise distance along the body), for a step change in angle of attack at t = 0, from $\alpha = 15°$ to $\alpha = 20°$.

In each crossflow plane, the strength of the vorticity jet is derived from the observation that for a flat plate boundary layer of thickness δ, the streamwise vorticity flux per unit span is given to the order of boundary layer theory by:

$$\int_0^\delta U\Omega dy = \frac{U_e^2}{2} \tag{15}$$

where U_e is the velocity at the edge of the boundary layer. At the point of separation, it is assumed that a net fraction λ of this vorticity flux is injected into the freestream. This method has been formally shown[1] to be equivalent at subsonic speeds to the "vortex cloud" method used by Mendenhall and Perkins.[9] In its numerical implementation, the incremental normal vorticity flux released between x and x + Δx is derived from the condition:

$$\int_x^{x+\Delta x}\int_{s_1}^{s_2} V_n \Omega ds = \frac{1}{2}(V_{sp}^2 + W_{sp}^2)\lambda\Delta x \tag{16}$$

where the subscript "sp" denotes a value at separation, and s_1 and s_2 are values of the curvilinear coordinate along the body in the crossflow plane, placed on either side of the separation point. The empirical "vortex reduction factor" λ determines the amount of vorticity shed at that point and was set to be equal to 0.6 in the present calculations.

The transfer of the vorticity jet boundary condition to the computational fuselage and the transport of vorticity from that point are analyzed next. For consistency with the model used to transfer velocity boundary conditions, the Stratford criterion is implemented on the true surface of the body by making use of the inverse transformation $Z = \chi^{-1}(\sigma)$ to obtain Cp (see Section 5). This same transformation can, in turn, be used to compute the intersection of the stagnation streamline with the computational boundary. This location would determine the placement of the vorticity jet on the computational fuselage. At the present time, the computer code is set up to prescribe any distribution of normal vorticity fluxes along the computational fuselage boundary. For simplicity, the results presented in this paper consider only the model case of a concentrated vorticity flux placed at the closest grid point from the location of separation.

An additional difficulty in the integration of the vorticity transport equation arises from the fact that, in the original CAP-TSD code, vorticity was initially pulled away from the computational domain and towards the body, due to the downwash effect. This problem was circumvented by placing the body *parallel* to the grid and considering the freestream flow to be inclined at an angle of attack α. As a first approximation, the disturbance potential ϕ can be solved using the method of integration in CAP-TSD, as long as α remains small, although in the present study the theory is pushed well beyond its limits, i.e., for finite α. The potential, ϕ is therefore replaced by ($\phi + \sin(\alpha)\, z$) in order to resolve the transport of vorticity away from the computational fuselage.

b) *Farfield and Symmetry Plane.* The farfield boundary conditions are based on characteristic 'non-reflecting' boundary conditions for ϕ, and on the fact that the rotational flow component must vanish away from the solid boundary.[3] The non-reflecting boundary conditions are derived after Whitlow.[10] These are:

$$\left.\begin{array}{lll} \text{Upstream boundary:} & \phi = & 0 \\ \text{Downstream boundary:} & \phi_x = & \frac{1}{2}\left[\frac{B}{C} - \frac{D}{\sqrt{C}}\right]\phi_t \\ \text{Upper boundary:} & \phi_z = & -\frac{D}{2}\phi_t + A_y \\ \text{Lower boundary:} & \phi_z = & \frac{D}{2}\phi_t + A_y \\ \text{Spanwise boundary:} & \phi_y = & -\frac{D}{2}\phi_t - A_z \end{array}\right\} \tag{17}$$

where:

$$\left.\begin{array}{lll} \bar{A} = M_\infty^2 & B = 2M_\infty^2 & C = E + 2F\phi_x \\ D = \left(\frac{B^2}{C} + 4\bar{A}\right)^{1/2} & E = 1 - M_\infty^2 & F = -\frac{1}{2}(\gamma+1)M_\infty^2 \end{array}\right\} \tag{18}$$

The present study is restricted to pitching motion only About the symmetry plane, v and Ω are antisymmetric in y ; therefore at y = 0:

$$\phi_y + A_z = 0 ; \Omega = 0 \tag{19}$$

c) *Horizontal Fins and Wake.* For horizontal lifting surfaces, the boundary conditions on ϕ are unchanged from their original treatment in CAP-TSD (Refs. 11 and 12). Along the top (+) and bottom (-)

surfaces of the surface, the vertical disturbance velocity is specified according to a flow tangency condition:

$$\phi_z^{\pm} = \delta^{\pm}(x,y,t) \qquad (20)$$

where δ represents the local vertical deflection angle at the fin surface. Across the wake, the vertical velocity component ϕ_z is required to be continuous, while the wake circulation, Γ, is convected downstream[12] by integrating the equation

$$\Gamma_x + \Gamma_t = 0 \qquad (21)$$

It may be shown[13,14] from a contour integral in the trailing edge plane of the fin that an initial condition at the trailing edge is given by:

$$\Gamma_{te}(y,t) = \phi^{+}_{te}(y,t) - \phi^{-}_{te}(y,t) \qquad (22)$$

Equation 21 can be used to represent at each streamwise location the effect of the wake on the body, by assigning a strength Γ_j to point vortices placed at each spanwise grid location of the wake cut. This horizontal array of point vortices is then mapped into σ-space, inducing a complex velocity

$$\frac{dF}{d\sigma} = \sum_j \frac{i}{2\pi}\Gamma_j\left[\frac{1}{\sigma-\bar{\sigma}_j} - \frac{1}{\sigma-\sigma_j}\right] \qquad (23)$$

where σ_j is the location of the individually mapped vortices and $\bar{\sigma}_j$ denotes the complex conjugate of σ_j. The summation is carried out over the set of spanwise grid locations representing the wake. The complex velocity $dF'/d\sigma$ induced by the wake circulation is subsequently added to $dF/d\sigma$ in Equations 12 and 13 to give the proper spanwise and normal boundary conditions on the computational fuselage.

5. Pressure Coefficient Calculation

At the solid surfaces the pressure coefficient is calculated using the isentropic[15] relation:

$$C_p = \frac{2}{\gamma M_\infty^{\;2}}\left\{\left[1 - \frac{(\gamma - 1)}{2} M_\infty^{\;2}\left[2\frac{\partial\phi}{\partial t} + q^2 - q_\infty^2\right]\right]^{\frac{\gamma}{(\gamma-1)}} - 1\right\} \qquad (24)$$

where q^2 is the squared modulus of the total velocity. Nixon et al.[2] pointed out that in order to get the correct effect resulting from the tilting of the lee-side vortex away from the surface, it is necessary to apply a second order correction to q^2 so that it includes the rotational component of streamwise velocity:

$$U_R = -\int^{z} \frac{\partial^2 A}{\partial x \partial y}\, dz \qquad (25)$$

The inclusion of this higher order term has been shown[2,3] to yield more accurate results and lays a theoretical foundation for the "empirical correction" used by Mendenhall and Perkins.[9]

In order to obtain Cp at the body surface, it is necessary to know q^2 and $\partial\phi/\partial t$ at the body. This is achieved by inverting the transformation used to transfer boundary conditions from the true body surface to the cartesian computational fuselage. Grid points Z belonging to the computational boundary are first projected orthogonally onto points Z_s which belong to the true body surface. Based on the analytic solution for a point vortex in a crossflow, the complex velocities at the corresponding points in σ-space can be related simply. It can be shown that the velocities at σ and σ_s differ by an additive complex quantity κ which depends only upon σ, σ_s, and the strength and position of potential vortices present in the model. Following the derivations of Ref. 3, this same transfer function κ, is used to obtain the complex velocity at σ_s, based on the *actual* (i.e., calculated) velocity at σ, i.e.:

$$\left.\frac{dF}{d\sigma}\right|_{\sigma_s} = \left.(-w-iv)\frac{d\chi}{d\sigma}^{-1}\right|_{\sigma} + \kappa(\sigma,\sigma_s,\sigma_o,\sigma_j,\Gamma_o,\Gamma_j) \qquad (26)$$

where σ_o is the mapped location of the rotational body vortex of strength Γ_o, and the σ_j's and Γ_j's represent the location and strength of the n_j wake vortices. The complex transfer function, κ, is given by:

$$\kappa = \frac{i}{2\pi}\sum_{j=0}^{n_j}\Gamma_j\left[\frac{1}{\sigma_s-\bar{\sigma}_j} + \frac{1}{\sigma-\sigma_j} - \frac{1}{\sigma_s-\sigma_j} - \frac{1}{\sigma-\bar{\sigma}_j}\right] \qquad (27)$$

The scaled crossflow velocity at the body surface is given, therefore, by the inverse mapping:

$$-w_s-iv_s = \left\{\left.(-w-iv)\frac{d\chi}{d\sigma}^{-1}\right|_{\sigma} + \kappa(\sigma,\sigma_s,\sigma_o,\sigma_j,\Gamma_o,\Gamma_j)\right\}\left.\frac{d\chi}{dZ}\right|_{Z_s} \qquad (28)$$

Similarly, the complex potentials at σ_s and σ can easily be related using the following relation:

$$\phi_s = \phi + \mathrm{Re}\left\{\sum_{j=0}^{n_j}\left[\frac{i}{2\pi}\Gamma_j \ln\left[\frac{(\sigma_s-\bar{\sigma}_j)(\sigma-\sigma_j)}{(\sigma_s-\sigma_j)(\sigma-\bar{\sigma}_j)}\right] - \sin(\alpha)\frac{a+b}{2}\eta_e(\sigma_s-\sigma)\right]\right\} \qquad (29)$$

Hence, $\partial\phi/\partial t|_s$ is not equal to $\partial\phi/\partial t$, and must be modified in order to account for the temporal variations of σ_o, Γ_o and Γ_j, which are the source of additional phase lags in the determination of the pressure coefficient.

6. Results

Time-accurate calculations were performed for a missile-shaped body of 11:1 aspect ratio and circular cross-section. The body is an ogive-cylinder with a 3-

caliber nose and 8-caliber straight section, chosen to allow comparisons with Tinling and Allen's[16] experimental data. In order to demonstrate the current capabilities of the code, generic rectangular horizontal and vertical fins could also be added to the body, as shown in the perspective view of Fig. 3. Each fin was infinitely thin and placed at zero angle of attack with respect to the body. The leading and trailing edges of the fins were located at $X_{le}/L = 0.74$ and $X_{te}/L = 0.86$, respectively. The horizontal lifting surface had a span equal to 85% of the maximum body radius. The body was configured at a mean angle of attack $\alpha = 15°$, which could be oscillated sinusoidally with an amplitude of ±20%. The Mach number was varied between $M_\infty = 0.3$ and $M_\infty = 1.5$.

For all of the results presented in this manuscript, the computational mesh size was 45 x 32 x 50 in the streamwise, spanwise, and normal directions. The cartesian grid was designed to optimize spatial resolution around the separated flow region, and extended at least five body diameters in the spanwise and normal directions (Fig. 1).

In order to verify the accuracy of the analytic transfer of boundary conditions described in Section 4, pressure distributions were computed for a purely irrotational calculation. Fig. 4 shows the Cp distribution as a function of roll angle, in a streamwise plane which corresponds to the straight section of the body. The data points (open symbols) represent the pressure coefficients calculated according to the method described in Section 5, where the grid points closest to the actual body (i.e., the inner "corners" in Fig. 1) have been used. This computed pressure distribution is compared to the analytical solution for potential flow around a circular cylinder (dashed line in Fig. 4). Since the body diameter is constant around this streamwise location, the two pressure distributions are expected to compare relatively well, provided that the appropriate vertical shift is added to the analytical solution. Note that this shift must be introduced, in order to take into account the local value of a streamwise component of velocity, which differs from unity. As may be seen from Fig. 4, the agreement, in the absence of vorticity, is quite satisfactory. This implies that the transfer of boundary conditions that was derived in Ref. 3 may be used reliably, to the extent that the surface rotational velocities induced by the distributed vorticity can be adequately represented by the effect of a point vortex.

The decomposition of the flowfield into rotational and irrotational velocity components is illustrated in Fig. 5, for a crossflow plane intersecting the fins. The left hand graph shows the irrotational velocity component, $\nabla\phi + \sin(\alpha)\overline{k}$, where $\overline{k}$ is the unit vector in the positive z-direction. The rotational component ∇xA (middle graph) illustrates the presence of a formed vortex away from the surface. The total velocity field (right hand side) is the superposition of rotational and irrotational flow components.

Fig. 6 shows the details of vorticity contours at X/D = 10.1 in the absence of fins, and illustrates the entrainment of vorticity from the point of shear layer separation, towards the core of the vortical structure exhibited in Fig. 5. The corresponding global dynamics of three-dimensional vorticity transport and vortex roll-up are illustrated in Fig. 7 for the case of a step change in angle of attack at t = 0, from $\alpha = 15°$ to $\alpha = 20°$, at a Mach number $M_\infty = 0.3$. In the present calculations, the incorporation of dynamic effects through the coupling of outer flow dynamics with the instantaneous motion of the separation line was inhibited along the forebody. In the absence of this restriction, vorticity at the nose is introduced too far away from the surface. This results in loss of coupling and early separation of a weak tip vortex. The source of this problem is similar to that identified earlier in the crossflow plane and has to do with the cylindrical nature of the computational fuselage in CAP-TSD. Consequently, vorticity jets were only introduced from the end of the forebody section (i.e., beyond X/D = 2.5), as seen from Fig. 7.

The anatomy of the flowfield is perhaps best described by the evolution of the velocity field at various downstream positions along the body (Fig. 8). At X/D = 4.0, little vorticity has been injected into the outer flow. The formation of a small region of reversed flow first becomes evident around X/D = 5.6. The phenomena of vortex roll-up and strengthening with increasing downstream distance can be observed from the evolution of the flowfield at X/D = 7.9 and X/D = 9.7. These observations remain qualitatively similar to those of Ref. 3, although in the latter work, the vortex strength and its vertical location were exaggerated, due to the inaccuracies involved in positioning a concentrated vorticity jet at a distant computational boundary, as previously discussed.

A quantitative comparison of pressure distributions at several downstream locations is made in Fig. 9. These pressure distributions are compared to the experimental data of Tinling and Allen[16] (open symbols) and the predictions of Mendenhall and Lesieutre[17] (dashed lines), using the "vortex cloud" method.[8] At all three locations, the current predictions are seen to overshoot both the experimentally acquired values and the vortex cloud predictions in the separated flow region. By comparison with the results of Nixon et al.,[3] one can infer that the discrepancy may be due to the lower strength of the rotational flow component. In the vortex cloud method, incipient separation was reported to take place around X/D = 1.0, but was only allowed beyond X/D = 2.5 in the present calculations. The level of disagreement between the experimental data and the current results is also seen to diminish with increasing downstream distance (a result also observed in Ref. 2).

Fig. 10 illustrates the effect of Mach number at an angle of attack $\alpha = 15°$ by comparing crossflow velocities / vorticity distributions at $M_\infty = 0.3$ and $M_\infty = 1.5$. As can be seen in this figure, the vorticity shed into the lee-side vortex is weaker in the supersonic case. This results in a smaller vortex, residing closer to the surface than in the case of subsonic flow.

One of the objectives of this study is to assess the aerodynamic phase lags which occur in unsteady separated flow. The phase lags result from various dynamic effects, which include lags in the position and strength of vortices with respect to the body motion. These phase lags originate from the fact that the position and strength of a vortex at any streamwise location along the body are the integral consequence of vorticity transport dynamics on the one hand, and the unsteady rate at which vorticity is fed into the vortex sheet on the other. Therefore the 'history effect' is related to convective phase delays, as well as additional time lags associated with the separation process itself. Ref. 8

provides a detailed account of the application of indicial theory to the prediction of unsteady separation.

In this approach, the motion of the separation point and the unsteady vorticity flux in a given crossflow plane are analyzed using two-dimensional time-accurate Navier-Stokes calculations. The study described in Ref. 8 shows that for viscous flow about a two-dimensional cylinder, the time-dependent behavior of both separation angle and vorticity flux can be accurately predicted using a convolution integral, based on the knowledge of the step response of the flowfield to a small perturbation in Mach or Reynolds number.

One of the results was that periodic fluctuations of the vorticity flux exhibited a 50% amplification at a reduced frequency based on diameter and crossflow velocity of: $k' = 2\pi fD/U_c = 2.5$. For the 11:1 aspect ratio body described above and at a mean angle of attack $\alpha = 15°$, this corresponds to a reduced frequency based on body length of approximately $k = 6.5$. At a Mach number $M_\infty = 0.9$ and for a hypothetical body length $L = 10$ m, this would correspond to a frequency $f = 10.5$ Hz, which is well within the range of structural frequencies exhibited by, e.g., sea-skimming missiles.[18]

To illustrate this effect, the total normal force coefficient (i.e., including body and fins) was recorded (Fig. 11) as a function of time, for the case of an oscillating angle of attack $\alpha(t) = \alpha_0 + \alpha_1 H(t)\sin(ktU_\infty/L)$, where $H(t)$ is the Heaviside step function, $\alpha_0 = 15°$, $\alpha_1 = 3°$, and $k = 6.47$. Two calculations were performed at a Mach number $M_\infty = 0.9$. In the first calculation (solid line), the Stratford criterion (Equation 14) is used at each time step to determine the separation location. This location is used to obtain V_{sp} and W_{sp} in Eq. 16. The value of the crossflow velocity at separation then specifies the normal vorticity flux according to Equation 16. This first scenario represents, therefore, a 'quasi-steady' implementation of the Stratford criterion.

In a second calculation initiated from the same steady state, a negligible amplification of separation angle fluctuations was assumed, while a time-dependent vorticity flux $\psi(x,t)$ was imposed based on the findings of Ref. 8. This flux had an identical mean, $\bar{\psi}(x)$, to that of the first calculation, but had a fluctuating component equal to $\beta(\psi(x,t)-\bar{\psi}(x))$, where $\beta = 1.55$. The amplification factor β was chosen to be real because previous results[8] have indicated that the phase delay at that frequency is close to zero. The resulting normal force coefficient is indicated by the dashed line in Fig. 11. As may be seen from this figure, the total normal force lags the motion by approximately 320° in both cases. However, significant differences are observed between peak values and harmonic content of the oscillatory loads.

As a final word of caution, it should be noted that the results of Fig. 11 do not represent a realistic evaluation of the importance of dynamic effects on the separation process, but are simply meant as an example illustrating the way in which small changes in the separation (vorticity) boundary conditions may affect the total loads. Among the reasons that this second calculation may not be realistic are the fact that the results of Ref. 8 are limited to low Reynolds numbers and small amplitudes. Additionally, the instantaneous perturbations of the Navier-Stokes equations involved step changes in Mach number and Reynolds number, rather than in the surface pressure distribution, which is the basis of the Stratford criterion. In other words, the quasi-steady implementation of the Stratford criterion does not correspond to a quasi steady change in angle of attack, as evidenced by the temporal evolution seen in Fig. 2. In spite of these differences, it should be noted that additional motion of the separation point has been ignored, and that a seventeen-fold increase in Reynolds number (Fig. 12) suggests an increase in phase delays, as well as further amplification of fluctuations in the vorticity flux. This implies that the differences in the predictions of Fig. 11 may actually underestimate the effects of unsteady separation.

7. Concluding Remarks

The theory that was developed in Ref. 3 to treat flow separation and related vortex effects in unsteady transonic flow around slender bodies was implemented using a modified version of the CAP-TSD[5] computer code. This theory involves the simultaneous solution of a modified Transonic Small Disturbance equation, a vector potential equation, and a three-dimensional unsteady vorticity transport equation[3]. In the present work, refinements in the representation of the computational fuselage are shown to yield significant improvements over previous predictions. The results of time-accurate computations for complete missile configurations at subsonic, transonic, and supersonic speeds suggest that realistic angle of attack configurations may be calculated using CAP-TSD, thus showing considerable potential for aeroelastic computations and unsteady aerodynamics.

References

[1] Klopfer, G. H. and Nielsen, J. N.: Computational Fluid Dynamics Applications to Missile Aerodynamics, Paper No. 3 in AGARD CP-336, Missile Aerodynamics, September 1982.

[2] Nixon, D., Caruso, S. C., and Klopfer, G. H.: Prediction of Transonic Flow with Vortex Effects, AIAA Paper 90-0389.

[3] Nixon, D., Reisenthel, P. H., Torres, T. O., and Klopfer, G. H.: Prediction of Unsteady Transonic Flow Around Missile Configurations, AIAA Paper 90-0934.

[4] Klopfer, G. H. and Nixon, D.: Transonic Flows with Vorticity Transport Around Slender Bodies, AIAA Journal, Vol. 27, No. 10, 1989, pp. 1461-1464.

[5] Batina, J. T.: An Efficient Algorithm for Solution of the Unsteady Transonic Small Disturbance Equation, AIAA Paper 87-0109.

[6] Stratford, B. S.: The Prediction of Separation of the Turbulent Boundary Layer, Journal of Fluid Mechanics, Vol. 5, 1959, pp. 1-16.

[7] Spangler, S. B. and Mendenhall, M. R.: Further Studies of Aerodynamic Loads at Spin Entry, ONR-CR-212-225-3, 1977.

[8] Reisenthel, P. and Nixon, D.: Application of Indicial Theory to the Prediction of Unsteady Separation, NEAR Paper No. 288, Nielsen Engineering & Research, September 1990.

[9] Mendenhall, M. R. and Perkins, S. C., Jr.: Vortex Cloud Model for Body Vortex Shedding and Tracking. In Tactical Missile Aerodynamics, (edited by M. J. Hemsch and J. N. Nielsen), Vol. 104, Progress in Astronautics and Aeronautics, AIAA, 1986.

[10] Whitlow, W., Jr.: Characteristic Boundary Conditions for Three-Dimensional Transonic Aerodynamics, NASA TM-86292.

[11] Batina, J. T., Seidel, D. A., Bennett, R. M., Bland, S. R., and Neely, R. W.: A Program for Solving the Unsteady Transonic Small-Disturbance Equation for Aeroelastic Analysis of Realistic Aircraft Configurations, Preliminary Users's Manual for CAP-TSD (Version 1.0), NASA Langley Research Center, December 1987.

[12] Batina, T. M.: An Efficient Algorithm for Solution of the Unsteady Transonic Small-Disturbance Equation, NASA TM-89014, December 1986.

[13] Nielsen, J. N., Spangler, S. B., and Hemsch, M. J.: A Study of Induced Rolling Moments for Cruciform-Winged Missiles, NEAR TR 61, Nielsen Engineering & Research, November 1973.

[14] Dillenius, M. F. E.: Program LRCDM2, Improved Aerodynamic Prediction Program for Supersonic Canard-Tail Missiles With Axisymmetric Bodies, NASA CR 3883, April 1985.

[15] Nixon, D.: The Effect of Vortex Rotation on the Flow Around a Missile, NEAR Paper No. 266, Nielsen Engineering & Research, January 1990.

[16] Tinling, B. E. and Allen, C. Q.: An Investigation of the Normal-Force and Vortex-Wake Characteristics of an Ogive-Cylinder Body at Subsonic Speeds, NASA TND-1297, April 1962.

[17] Mendenhall, M. R. and Lesieutre, D. J.: Prediction of Vortex Shedding From Circular and Noncircular Bodies in Subsonic Flow, NASA CR-4037, January 1987.

[18] Lesieutre, D., J., Nixon, D., Dillenius, M. F. E., and Torres, T. O.: Analysis of Missiles Flying Low Over Various Sea States, NEAR TR-408, November 1989.

[19] Rott, N.: Diffraction of a Weak Shock With Vortex Generation, Journal of Fluid Mechanics, Vol. 1, No. 1, 1956, pp. 111-128.

[20] Kuhn, G..D., Spangler, S. B., and Nielsen, J. N.: Theoretical Study of Vortex Shedding From Bodies of Revolution Undergoing Coning Motion, NASA CR-1448, October 1969.

Acknowledgment

The authors gratefully acknowledge the support of this work by the Army Research Office under contract DAAL03-87-C-0008, monitored by Dr. T. Doligalski.

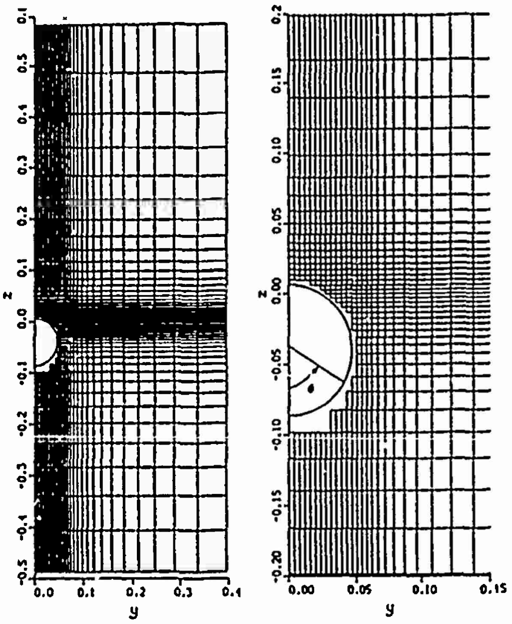

Figure 1. Cross-sectional Views of the Cartesian Grid (Left: Full Grid ; Right: Close-up Illustrating Serrated-Edged Computational Fuselage, with Roll Angle Convention).

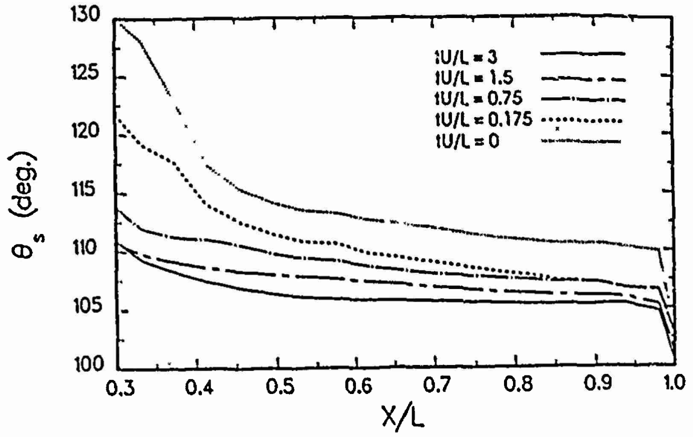

Figure 2. Time-Dependent Separation Line for a Step Change in Angle of Attack at t = 0, from $\alpha = 15°$ to $\alpha = 20°$ ($M_\infty = 0.3$).

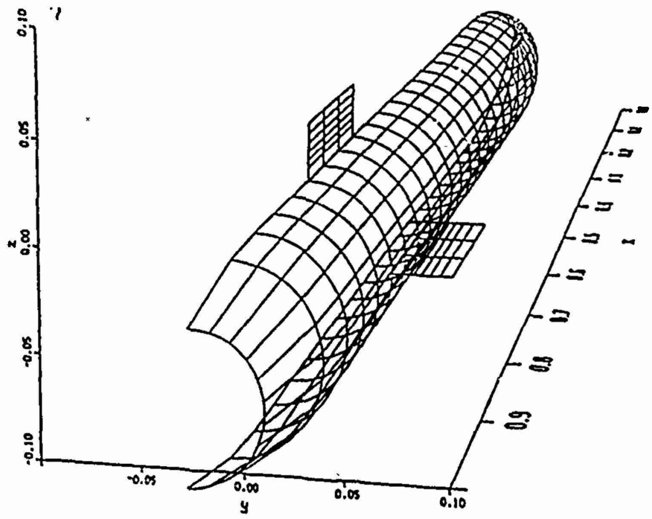

Figure 3. Perspective View of Prototypical Slender Body Under Consideration, Including Horizontal and Vertical Fins.

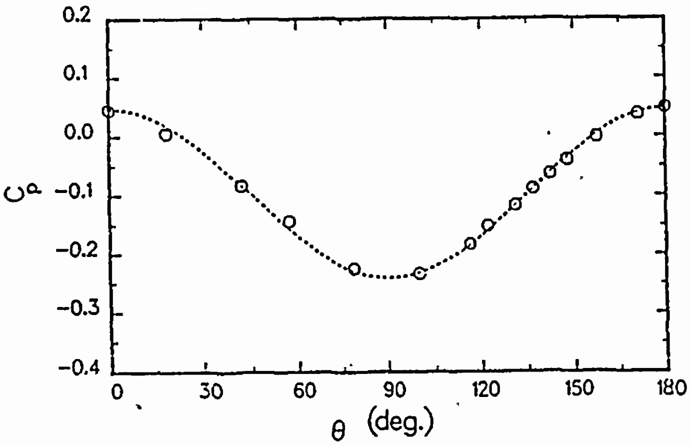

Figure 4. Illustration of the Accuracy of the Transfer of Boundary Conditions by Comparison of Pressure Coefficient Distributions between a Purely Irrotational Calculation (X/D = 7.9) and the Analytical Two-Dimensional Potential Flow Solution ($\alpha = 15°$, $M_\infty = 0.3$).

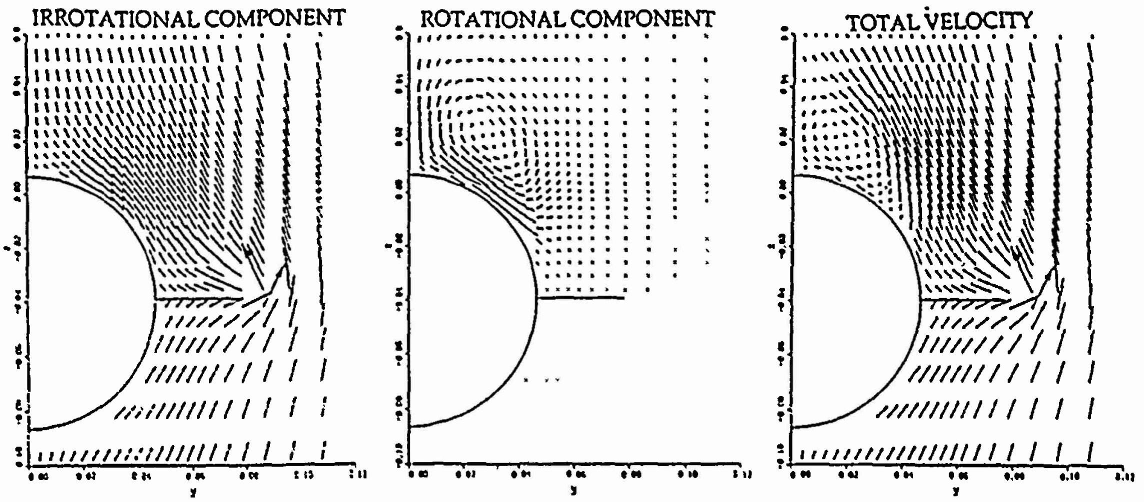

Figure 5. Illustration of the Helmholz Decomposition Procedure at the Leading Edge of a Horizontal Lifting Surface (X/L = 7.4, $M_\infty = 0.3$, $\alpha = 15°$).

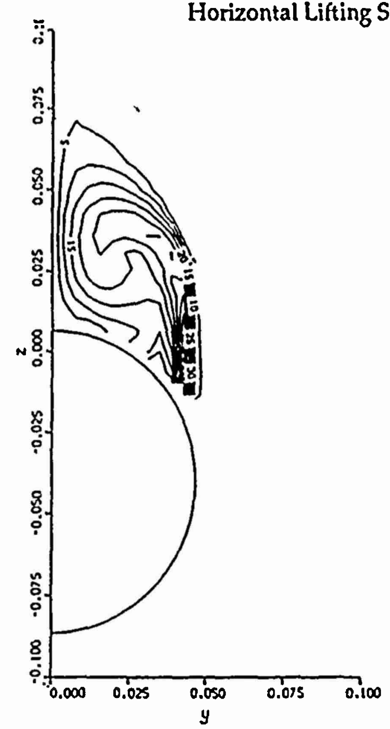

Figure 6. Vorticity Distribution at X/D = 10.1 ($\alpha = 15°$, $M_\infty = 0.3$).

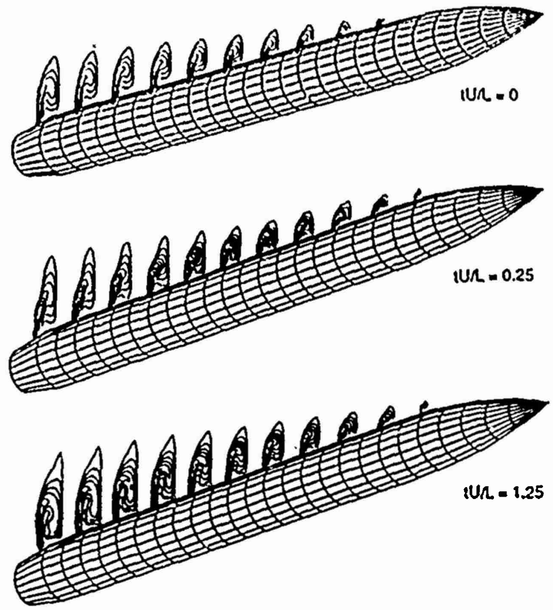

Figure 7. Half-Space Representation of Streamwise Vorticity Contours Illustrating the Time-Dependent Formation of the Leeward Side Vortical Structure, for a Step Change in Angle of Attack at t = 0, from $\alpha = 15°$ to $\alpha = 20°$ ($M_\infty = 0.3$).

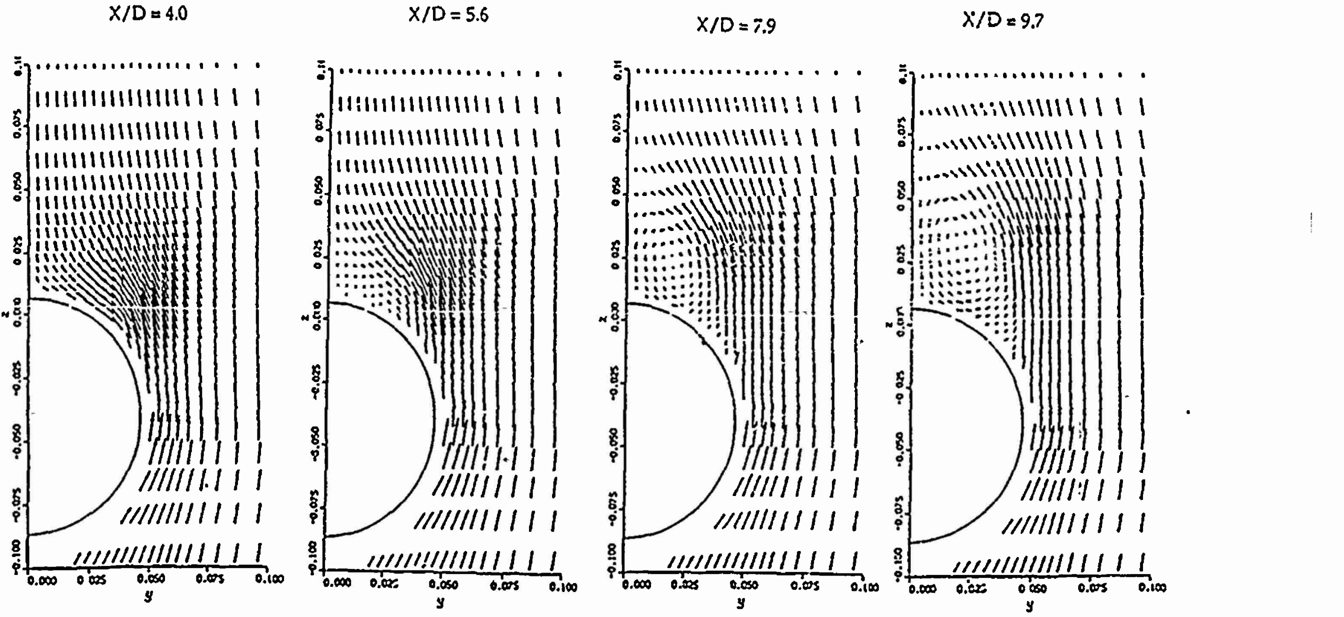

Figure 8. Streamwise Evolution of the Vortical Crossflow ($M_\infty = 0.3$, $\alpha = 15°$).

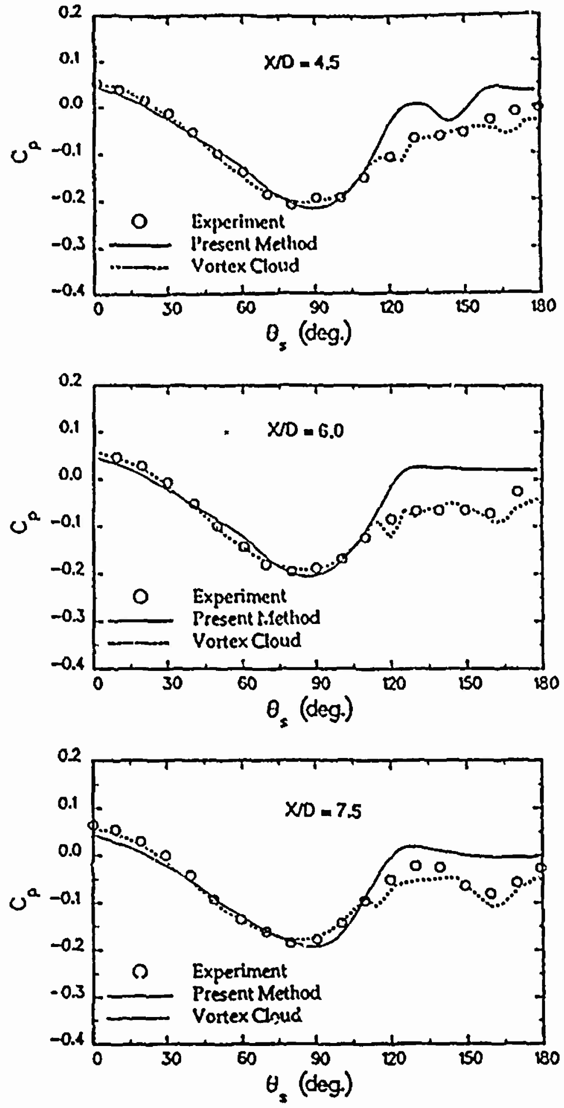

Figure 9. Comparison of Pressure Coefficient Distributions between Current Method (solid line), Experimental Data (Tinling and Allen, 1962, open symbols), and Vortex Cloud Method (Mendenhall and Lesieutre, 1987, dashed line), ($\alpha = 15°$, $M_\infty = 0.3$).

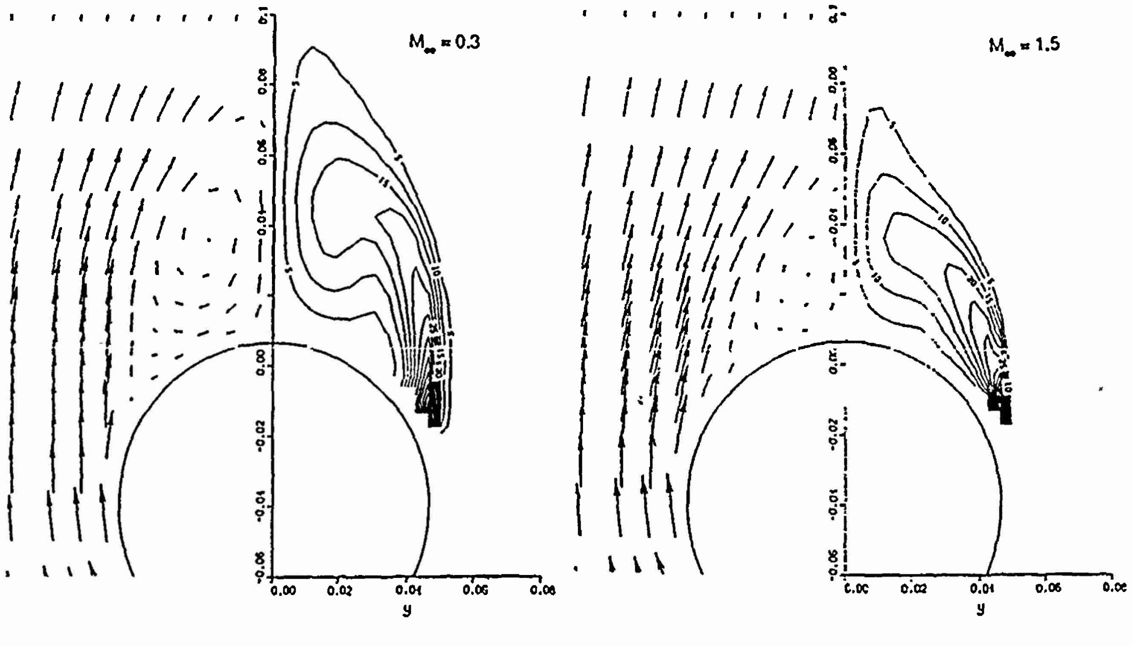

Figure 10. Mach Number Comparison of Vorticity Distributions and Crossflow Velocities at $M_\infty = 0.3$ and $M_\infty = 1.5$, ($\alpha = 15°$, $X/D = 10.5$).

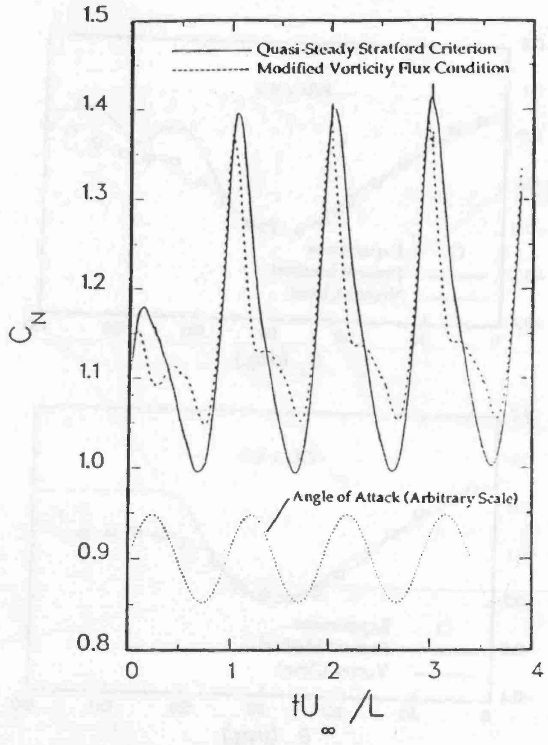

Figure 11. Comparison of Normal Force Coefficient Time Histories Between Predictions Using: *i)* Quasi-Steady Stratford Criterion (solid line), and *ii)* Modified Vorticity Flux Condition (dashed line), for a 20% Sinusoidal Oscillation of Angle Attack Around $\alpha_o = 15°$, $M_\infty = 0.9$.

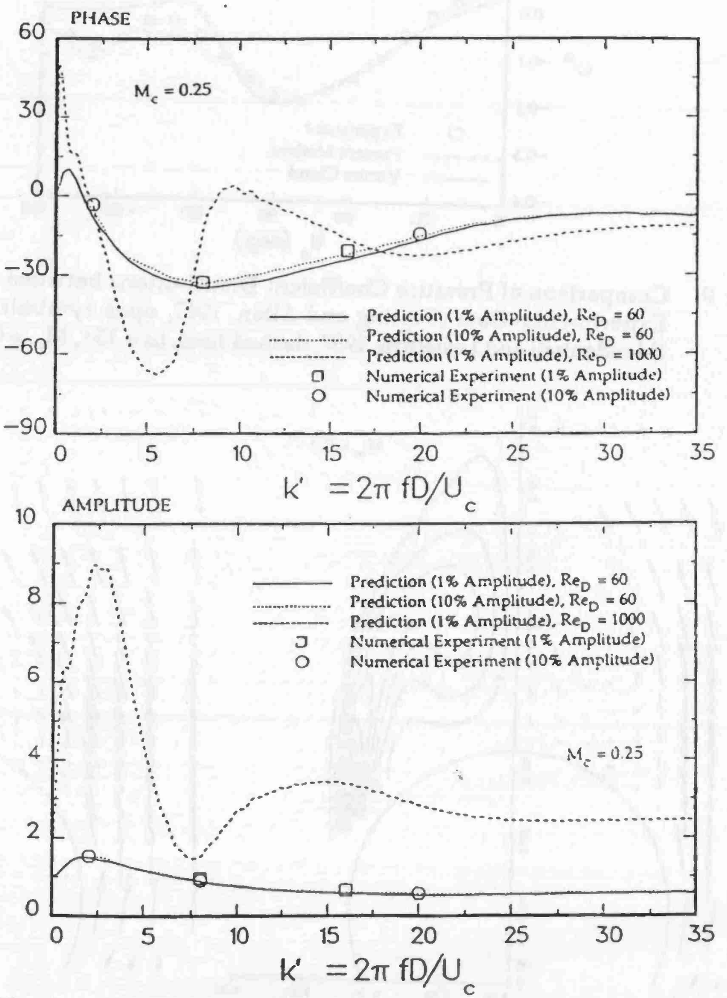

Figure 12. Reynolds Number Comparison of Theoretical Predictions (Based on Indicial Theory) of Phase Delays (top graph) and Amplification Factors (bottom graph) of the Vorticity Flux, Subject to Cross-Flow Mach Number Oscillation About $M_c = 0.25$. Open Symbols Are the Result of Numerical Experiments Based on Two-Dimensional Navier-Stokes Calculations.[8]